Spring 5-2012

# Application of a Hybrid 3D-VAR Data Assimilation System in the Monterey Bay to Study Regional Dynamics of the California Current System

Chudong Pan
*University of Southern Mississippi*

The University of Southern Mississippi

# APPLICATION OF A HYBRID 3D-VAR DATA ASSIMILATION SYSTEM IN THE MONTEREY BAY TO STUDY REGIONAL DYNAMICS OF THE CALIFORNIA CURRENT SYSTEM

by

Chudong Pan

Abstract of a Dissertation
Submitted to the Graduate School
of The University of Southern Mississippi
in Partial Fulfillment of the Requirements
for the Degree of Doctor of Philosophy

May 2012

ABSTRACT

APPLICATION OF A HYBRID 3D-VAR DATA ASSIMILATION SYSTEM

IN THE MONTEREY BAY TO STUDY REGIONAL DYNAMICS

OF THE CALIFORNIA CURRENT SYSTEM

by Chudong Pan

May 2012

A data assimilation system combining 3-dimensional variational scheme and Navy Coastal Ocean Model was applied to the Monterey Bay area to assimilate temperature and salinity glider data collected in August 2003. The hybrid background error covariance model in the present 3-dimensional variational system incorporates both the static and the flow-dependent background error covariance. To explore the impact of high temporal resolution on the overall skill of the assimilation system, the intended data assimilation interval was set to 1 hour in the present study. A Floating Temporal Window approach is designed to keep the computational efficiency of the scheme and to retain the flow-dependent. Both twin data experiments with "synthetic" data and real data experiments were performed in the present study.

The performance of the traditional 3-dimensional variational scheme and the hybrid scheme in twin data experiments were evaluated with respect to the "true state." The hybrid scheme reduces both temperature and salinity errors during the twin data experiment, especially during the transition period from wind relaxation to upwelling events and vice versa.

In real data experiments, the model performance is validated against independent mooring observations. In the first real data experiment, the model free run, data

assimilation run with traditional scheme, and data assimilation run with hybrid scheme were compared. The assimilation skill was tested by calculating the normalized distance between the assimilation results and observations at the mooring locations. The performance of the hybrid scheme generally exceeded the performance of the traditional scheme. Although there was no velocity data assimilation in the experiments, the change of temperature and salinity fields originated from glider data assimilation had a positive impact on the velocity fields according to mooring velocity records.

The second real data experiment compared the hybrid schemes with the full ensemble and the Floating Temporal Window ensemble. Results showed that the Floating Temporal Window scheme provided lower discrepancy between the values of temperature, salinity and velocity predicted by the model and observed at the moorings. The improvement became more clearly visible during the upwelling and relaxations events associated with intermittent wind forcing.

The results from the Navy Coastal Ocean Model free run and the data assimilation run with the hybrid scheme were compared with historical data. Comparisons have shown that the Navy Coastal Ocean Model combining with the hybrid 3-dimensional variational assimilation system was capable of reproducing major dynamical features, including onshore-offshore translation of the Monterey Bay Eddy during upwelling and relaxation events, coastal upwelling and respective upwelling filaments, the appearance of the California Undercurrent, and the interaction between the California Undercurrent and California Current.

The University of Southern Mississippi

# APPLICATION OF A HYBRID 3D-VAR DATA ASSIMILATION SYSTEM IN THE MONTEREY BAY TO STUDY REGIONAL DYNAMICS OF THE CALIFORNIA CURRENT SYSTEM

by

Chudong Pan

A Dissertation
Submitted to the Graduate School
of The University of Southern Mississippi
in Partial Fulfillment of the Requirements
for the Degree of Doctor of Philosophy

Approved:

Dmitri Nechaev_____
Director

Max Yaremchuk_____

Hans Ngodock_____

Stephan Howden_____

Vladimir M. Kamenkovich_____

Susan A. Siltanen_____
Dean of the Graduate School

May 2012

ACKNOWLEDGMENTS

The writer would like to thank his advisor, Dr. Dmitri Nechaev, and the other committee members, Dr. Max Yaremchuk, Dr. Vladimir Kamenkovich, Dr. Hans Ngodock, and Dr. Stephan Howden, for their great advices and support during this study. I would like to thank the Office of Naval Research (Program element 0602435N) and the North Pacific Research Board (project 828) for funding this project. The Fortran and Matlab programming help from Dr. Max Yaremchuk and Dr. Xiaobiao Xu is highly appreciated. I would like to thank Dr. Igor Shulman for providing the wind data and advice. I would like to thank David Rosenfield for proofreading this dissertation. I would also like to thank all my friends at USM. It's been a great time having you guys around. Special thanks go to my family, my mom, and my girlfriend, Lingmin, for their support and believing me.

TABLE OF CONTENTS

LIST OF TABLES

Table

LIST OF ILLUSTRATIONS

Figure

LIST OF ABBREVIATIONS

| | |
|---|---|
| 3D-VAR | 3-Dimensional Variational Assimilation |
| 4D-VAR | 4-Dimensional Variational Assimilation |
| ADCP | Acoustic Doppler Current Profilers |
| AOSN-II | Autonomous Ocean Sampling Network-II |
| AUV | Autonomous Underwater Vehicle |
| AVHRR | Advanced Very High Resolution Radiometer |
| BEC | Background Error Covariance |
| CC | California Current |
| CCS | California Current System |
| CTD | Oceanographic tool used to measure Conductivity, Temperature and Depth of sea water |
| COAMPS | Coupled Ocean-Atmosphere Mesoscale Prediction System |
| CUC | California Undercurrent |
| DC | Davidson Current |
| EBC | Eastern Boundary Current |
| ECMWF | European Centre for Medium-Range Weather Forecasts |
| EnKF | Ensemble Kalman Filter |
| EnOI | Ensemble Optimal Interpolation |
| EOF | Empirical Orthogonal Functions |
| FTW | Floating Temporal Window |
| GC-IBM | Ghost Cell Immersed Boundary Method |
| GDE | Generalized Diffusion Equations |
| HF | High-Frequency |

| | |
|---|---|
| HOPS | Harvard Ocean Prediction System |
| IC | Inshore Countercurrent |
| ICON | Innovative Coastal-Ocean Observing Network model |
| KF | Kalman Filter |
| MBARI | Monterey Bay Aquarium Research Institute |
| MBARM | Monterey Bay Area Regional Model |
| MBE | Monterey Bay Eddy |
| MSC | Monterey Bay Submarine Canyon |
| NCEP | National Centers for Environmental Prediction |
| NCODA | Navy Coupled Ocean Data Assimilation |
| NCOM | Navy Coastal Ocean Model |
| NHY | Non-Hydrostatic |
| NMFS | National Marine Fisheries Service |
| NOAA | National Oceanic and Atmospheric Administration |
| NPS | Naval Postgraduate School |
| NRL | Naval Research Laboratory |
| OEC | Observational Error Covariance |
| OI | Optimal Interpolation |
| PE | Primitive Equation |
| POM | Princeton Ocean Model |
| POST | Point Sur Transect |
| PSAS | Physical-space Statistical Analysis System |
| PWC | Pacific West Coast model |
| RMS | Root Mean Square |
| ROMS | Regional Ocean Modeling System |

SOAR Second Order Auto-Regressive

SOFA The System for Ocean Forecasting and Analyses

SWR Short Wave Radiation

# CHAPTER I

## INTRODUCTION

As one of the most famous upwelling regions in the world, the Monterey Bay, located on the central coast of California, has been recognized as a National Marine Sanctuary (Shulman *et al*., 2002) for a long time. The Monterey Bay has a distinctive geometry feature. The Bay is oriented north-south and the west of the Bay is directly connected to the Pacific Ocean. Being the largest bay of the West Coast of the United States, its main portion measures approximately 21 km wide east-to-west and about 35 km north-to-south. The Monterey Bay Submarine Canyon (MSC) extends from the Pacific side into the center of the Bay, separating the Bay into a northern part and a southern part (Figure 1). The continental shelf to the north of the Bay is relatively shallower (within the 50 m isobath) than the shelf to the south (within the 100 m isobath). The shallow continental shelf provides a strong contrast to the MSC which descends rapidly to at least 2000 m.

The atmospheric feature in the Monterey Bay area is characterized by the dominant northwesterly winds with occasional wind reversal or relaxation. Prevailing northwesterly winds are the major causes of local upwelling events. Two upwelling centers of the Monterey Bay have been identified: Point Aňo Nuevo and Point Sur. The cold water that originates from these two upwelling centers provides important dynamical information. The movement of upwelling filaments is a mirror of the regional circulation and near-shore currents.

The regional circulation in the Monterey Bay area is closely related to the California Current System which includes three major currents (Figure 2): California

Current (CC), Inshore Countercurrent (IC, also called Davidson Current, DC) and California Undercurrent (CUC). Local circulation patterns and the water mass properties inside and outside the Bay change during upwelling events and wind relaxation events.

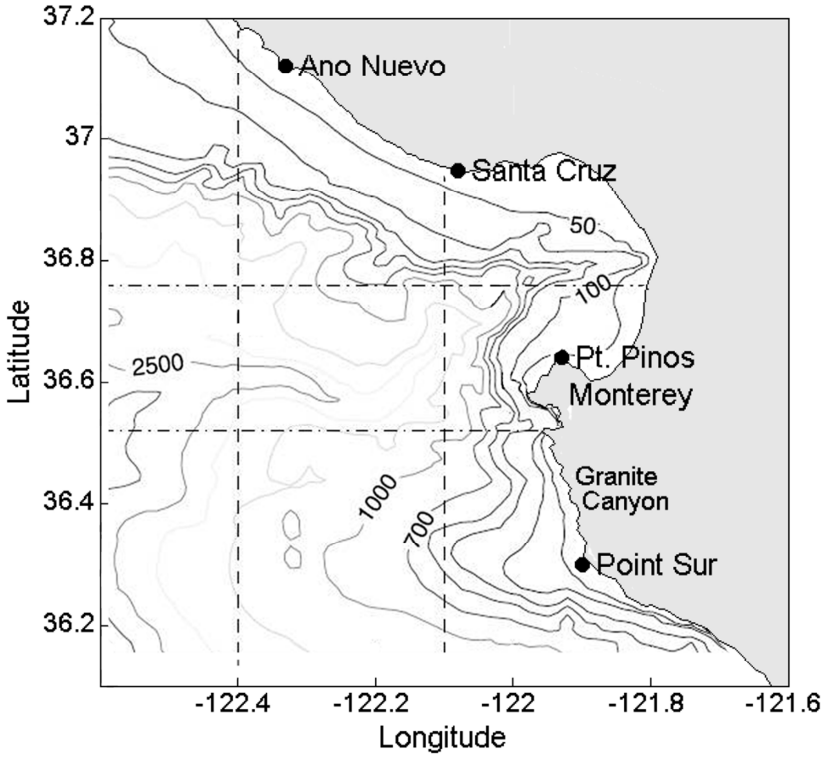


Figure 1. Bathymetry of Monterey Bay area (modified from Tseng *et al*., 2005).

In recent years, observational networks developed by a number of oceanographic institutions such as Naval Research Laboratory (NRL), Naval Postgraduate School (NPS), NOAA/NMFS and Monterey Bay Aquarium Research Institute have provided a great amount of oceanic data for data assimilation and ocean modeling projects in the Monterey Bay region. With unique features like the complex coastline and bathymetry, the presence of Monterey Bay Submarine Canyon (MSC), direct communication of water masses with the Pacific Ocean, numerous local upwelling events and increasing observations, the Monterey Bay has become one of the most attractive sites for data

assimilation and ocean modeling over the past decade.

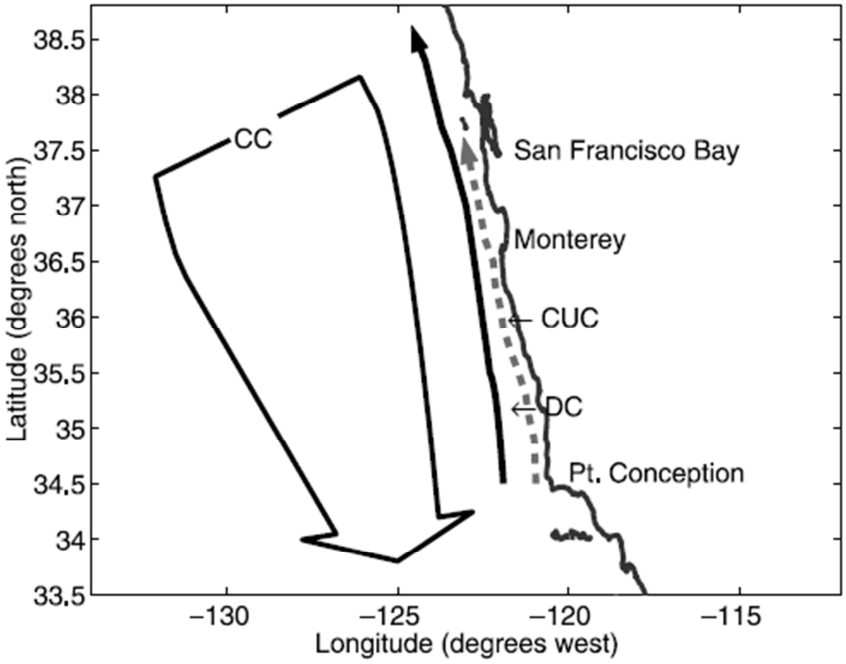


Figure 2. California Current System (Tseng *et al*., 2005).

Ensemble based data assimilation methods have been investigated and applied in atmospheric and oceanic studies. Most of ensemble-based data assimilation methods evolved from the ensemble Kalman filter (EnKF) (Evensen, 2003). It is established that ensemble-based techniques are capable of generating flow-dependent background error covariances which control the proper weighting of the background field and observations (Wang *et al*., 2007).

Unlike ensemble-based methods, variational data assimilation techniques utilize heuristic background error covariance models (hereafter referred to as BEC), which simulate BECs without direct analysis of the model statistics. These methods (Courtier *et al*., 1998; Weaver and Courtier, 2001; Wang *et al*., 2007; Dobricic and Pinardi, 2008; Li *et al*., 2008) are widely used in operational schemes of many oceanographic institutions like Naval Research Laboratory (NRL) and National Centers for Environmental

Prediction (NCEP) because of the increasing amount of observations generated by the improvement of observational technologies each year. Traditional 3-dimensional variational methods approximate BEC by a Gaussian or near-Gaussian function in one way or another (Courtier *et al*., 1998; Weaver and Courtier, 2001; Weaver and Ricci, 2004; Dobricic and Pinardi, 2008; Li *et al*., 2008). Since the BEC models in traditional variational schemes are normally time-independent, they are often referred to as "static" or "stationary" BEC. Nonetheless, in coastal regions, a static BEC might not be able to reflect real ocean dynamics since near-coastal regions are often affected by numerous factors, such as tides, bottom topography and large scale circulations (Wang *et al*., 2008).

To improve performance of regional 3-Dimensional Variational Assimilation (hereafter referred to as 3D-VAR) algorithms, hybrid BEC models have been under extensive development during the last decade (Hamill and Snyder, 2000; Etherton and Bishop, 2004; Buehner, 2005; Wang *et al*., 2007). In particular, results of Wang *et al*. (2007, 2008, 2009) and Yaremchuk *et al*. (2011) have shown that the hybrid schemes can produce more accurate results than traditional variational schemes and are capable of improving predictability by 5-15%.

In their recent work, Yaremchuk *et al*. (2011) proposed a hybrid 3D-VAR scheme for assimilating glider data into Navy Coastal Ocean Model (NCOM). Both the twin data experiments and real data experiments showed improvement for 12-hour forecast with the hybrid scheme. In twin data experiments, a model free run is performed and used as the "true state of the ocean." Bogus data are then generated from the "true state" at glider observation points plus a small perturbation. Bogus glider observations are assimilated into the ocean model. Since the bogus glider data are generated from the "true state," the

results of assimilation can be compared with the "true state." In real data experiments, the bogus data are replaced by real glider observations and the assimilation results are compared with observations from two independent mooring points. In the real-data experiments of Yaremchuk *et al.* (2011), only data within one-hour interval near the analysis were used, therefore physical phenomena at scales less than one day were excluded from consideration and treated as noise by the assimilation algorithm. It is interesting to explore the impact of higher time resolution on the overall skill of the assimilation system. A shortened data assimilation interval, however, will increase the ensemble size substantially, which will increase the computational cost of the hybrid scheme. A Floating Temporal Window (hereafter referred to as FTW) is designed solve this problem in present study.

Given the sophisticated physical environment of Monterey Bay, successfully assimilating oceanic data with short time-scale interval will be a challenging and crucial step for the development of this hybrid 3D-VAR system. In addition, since the regional dynamics like wind fields, circulation patterns, temperature and salinity distributions and so forth affect water properties, primary production, oil and gas operations, sediment transport, fisheries and all kinds of near-shore activities, whether the hybrid data assimilation system can reproduce the major physical features of this region is of great interest.

The present study focuses on the continual development and application of the hybrid 3D-VAR data assimilation scheme combining with NCOM to assimilate temperature and salinity data with a short-time scale interval (one hour). The data used in this study are temperature and salinity profiles from Spray and Slocum gliders (Figure 3),

which were deployed by Monterey Bay Aquarium Research Institute (MBARI) during the second Autonomous Ocean Sampling Network (AOSN-II) experiment (late July – early September 2003). This study concentrated on addressing the following subjects: (a) comparison of the traditional 3D-VAR scheme with the hybrid scheme in twin data experiments; (b) comparison of the NCOM free run, NCOM data assimilation run with traditional 3D-VAR scheme, NCOM data assimilation run with hybrid scheme in real data experiments; (c) comparison of the hybrid scheme with full ensemble and the hybrid scheme with FTW ensemble; and (d) investigation of the capability of the hybrid 3D-VAR system to reproduce the major dynamical feature in Monterey region.

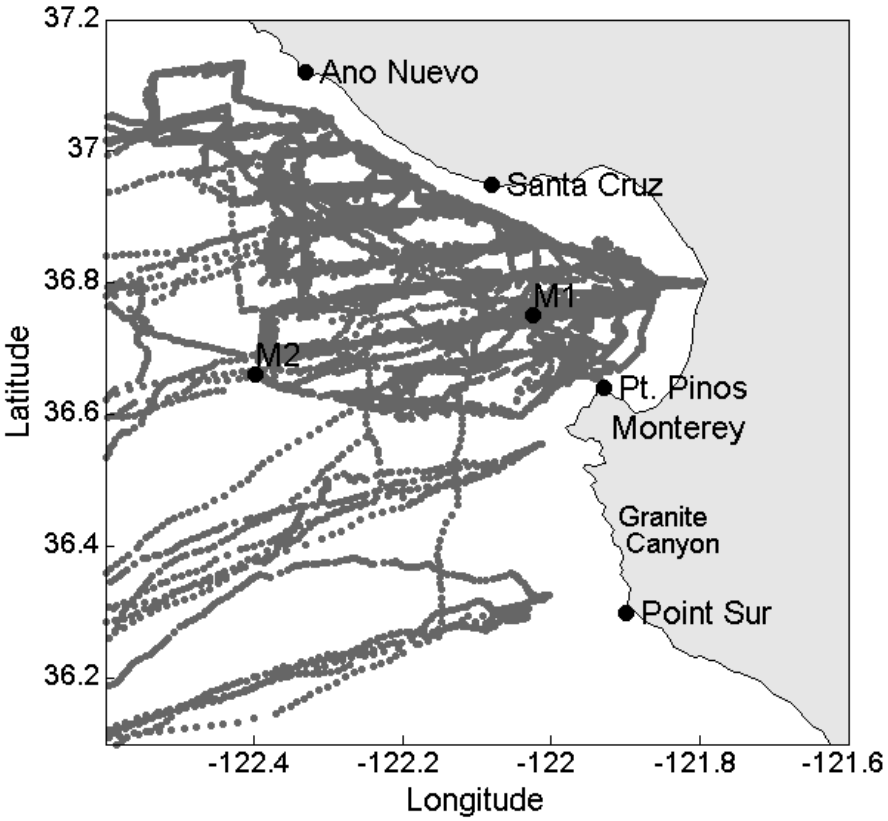


Figure 3. Glider locations during the second Autonomous Ocean Sampling Network (AOSN-II) experiment in 2003. M1 and M2 are two independent mooring locations.

# CHAPTER II

# REVIEW OF RELATED LITERATURE

## 2.1 California Current System

Right outside of Monterey Bay lies the California Current System (hereafter referred to as CCS), a part of an Eastern Boundary Current (EBC) system. The circulation inside the Monterey Bay is greatly influenced by CCS since they are intimately tied together. CCS includes three major currents: the dominant equatorward current - California Current (hereafter referred to as CC), poleward subsurface flow – California Undercurrent (hereafter referred to as CUC) and another poleward flow – Inshore Countercurrent (hereafter referred to as IC).

## 2.2 California Current (CC)

Lynn and Simpson (1987) specified four water masses in CCS: Pacific Subarctic water, Eastern North Pacific Central water, Equatorial Pacific water and Coastal Upwelled water. These water masses can be identified by their own temperature, salinity, dissolved oxygen and nutrients when they enter the CCS.

CC is the eastern branch of North Pacific gyre, a large-scale anticyclonic current covering most of northern Pacific basin. CC is a broad (typically about 1000 km offshore), near-surface (0-500 m depth) equatorward flow throughout the year. It flows along the west coast of North America carrying low temperature, low salinity, high dissolved oxygen and high nutrient Pacific Subarctic origin water (Lynn and Simpson, 1987).

The speed of CC is relatively slow. Lynn and Simpson (1987) evaluated the temporal and spatial variation of physical properties of CCS by harmonic analysis using

1950-1978 CalCOFI hydrographic survey data. According to Lynn and Simpson, the mean speeds of CC near surface (upper 150 m) are 4-12 cm/s. The seasonal mean speeds of CC are approximately 10 cm/s (Hickey, 1998). Although the mean speeds of CC is relatively low, there are some exceptional cases. For example, Davis (1985) derived a coastal flow pattern from 164 drifters deployed during U.S. Coastal Dynamics Experiment (CODE). The daily average speed of CC calculated by Davis reached 50 cm/s.

Lynn and Simpson (1987) also found that the core of CC near central and southern California (where Monterey Bay is located) often occurs between 300 to 400 km offshore. CC is strongest at the surface (Hickey, 1998). Lynn and Simpson (1987) analyzed dynamic height at 200 m (with respect to 500 dbar) and found that CC weakens downward from this layer. They also pointed out that CC is the strongest during spring and summer.

Most of the components of CC are equatorward. CC near the border of USA and Mexico, however, has a large shoreward component (Reid *et al*., 1963). Part of this flow continues southward along the coast. Another part of this shoreward flow turns northward, forming a poleward current known as Inshore Countercurrent (IC).

Chelton (1984) examined the seasonal variability of alongshore geostrophic velocity (with respect to 500 dbar) from Point Sur to Point Conception using 23 years of CalCOFI data. He found predominant equatorward geostrophic flow from February to September at both points.

Because the hydrographic data that Lynn, Simpson and Chelton used had coarse horizontal resolution (a grid width of 40-74 km) and limited vertical range (upper 500 m),

Tisch *et al*. (1992) re-examined the variability of the alongshore geostrophic currents and water properties off Point Sur using Point Sur transect (POST) hydrographic data with much finer horizontal resolution (5-10 km) and deeper extent (top to bottom). These data showed a great interannual variability of the circulation from the continental shelf to slope. A higher geostrophic velocity of CC (20 cm/s), comparing with Lynn and Simpson (1987), was observed using these data.

In February 1992, a shore-based High-Frequency (HF) radar network was set up around Monterey Bay region (Paduan and Cook, 1997), giving oceanographers the ability to derive two-dimensional flow pattern. HF radar data showed a band of equatorward flow across the mouth of Monterey Bay (Paduan and Rosenfeld, 1996). Paduan and Rosenfeld pointed out that this flow is part of the CC meander.

Strub and James (1995) spotted a large-scale equatorward jet existing at the offshore side of the west coast of USA using satellite data from the Geosat altimeter and the Advanced Very High Resolution Radiometer (AVHRR). They also found eddies and meanders associated with this large-scale jet.

Although temperature has been thought to be the major component in calculating sea water density in most locations of the world since the variation of temperature is usually more pronounced than salinity, Batteen *et al*. (1995) demonstrated the active effect of salinity on CCS density field. By integrating the specific volume anomaly over depth, they calculated the dynamic height anomaly and compared it with a referenced dynamic height anomaly (in which salinity has a fixed value of 35 psu with real temperature and pressure). Their results show that monthly mean salinity plays an important role in the geostrophic circulation of the CCS. Specifically, the mean variation

of salinity in CCS is the key factor to generate the equatorward current along the California coast and an offshore component near Baja California.

### 2.3 California Undercurrent (CUC)

California Undercurrent (CUC) is a narrow (about 10-40 km wide), subsurface poleward flow carrying high temperature, high salinity, low dissolved oxygen and high nutrient Equatorial Pacific origin water (Lynn and Simpson, 1987). CUC originates near Baja California and extends northward along the coast of North America to at least Vancouver Island (Hickey, 1998). A National Marine Fisheries Service (NMFS) ADCP data collected in summer 1995 indicated an uninterrupted pathway of CUC which traveled through Cape Blanco, Oregon, Cape Mendocino and California (Pierce *et al*., 2000), a distance of over 440 km. However, Lynn and Simpson (1987) observed a spring interruption of CUC near central California.

The core of CUC is often found along the continental slope (Reid *et al*., 1963; Wooster and Jones, 1970; Lynn and Simpson, 1987) and the strongest undercurrent is typically located between 100 m and 300 m from the surface (Chelton, 1984; Hickey, 1998). CUC is a relatively weak flow with mean speed less than 10 cm/s (Batteen and Vance, 1998), but observations indicated speeds of CUC could reach 30-50 cm/s (Hickey, 1998).

The earliest observation of CUC could be traced back to 1937 (Sverdrup and Fleming, 1941; Sverdrup *et al*., 1942). A poleward undercurrent was found at 200 m depth. They noted that equatorward CC overrides CUC during spring and summer when the northwesterly winds are the strongest.

Using a hydrographic survey (5 km grid spacing) conducted near Point Sur and

Monterey Bay, Wickham (1975) noticed an extremely complicated vertical distribution in this area. He found a band of water (10 - 20 km wide) with high temperature and high salinity intruding from the south.

There are several theories concerning the development of CUC. Pedlosky (1974) suggested that positive wind stress curl along the coast and descending surface heat to the north play an important role in developing and maintaining the undercurrent. Nelson (1976) analyzed monthly distributions of surface wind stress derived from surface marine observations (National Climatic Center historical files). He concluded that CUC along the west coast of North America may be driven by local positive wind stress curl which is consistent with Pedlosky's theory.

Chelton (1984) suggested that the undercurrent near Point Conception in early summer is topographically generated. This provides a second mechanism for the development of CUC.

Batteen (1997) pointed out that the wind forcing can generate both CC and CUC. He suggested that the β plane used in the primitive equation model is very important in generating realistic 3-dimensional structures of the CC and the CUC.

CUC has a very strong seasonal variation. According to Hickey (1998), poleward undercurrents in most locations are the strongest in summer or late fall and the weakest during spring. Although the seasonal variation of CUC typically has a semiannual signal, there is an exception that the seasonal variation signal of CUC near Point Sur is annual (Hickey, 1998).

Using aircraft data and HF radar data, Ramp *et al*. (2005) found that the water carried by CUC can be transported into the Monterey Bay, causing a dramatic change of

water properties in the south of the Bay during the peak of wind relaxation.

## 2.4 Inshore Countercurrent (IC)

IC is another poleward flow, also known as Davidson Current (DC). There is a shoreward flow, which is part of CC, near the border of USA and Mexico (Reid *et al*., 1963). Part of this flow continues southward along the coast of Baja California. Another part of this shoreward flow turns northward, forming the IC. It flows northward from Point Conception to Vancouver Island (Hickey, 1998). There is a quasi-permanent cyclonic eddy from Point Conception to northern Baja. Chelton (1984) suggested that the near-shore component of this eddy is part of the IC.

IC is relatively narrow (100 km wide and confined over the continental shelf and slope) and weak with mean speeds less than 5 cm/s (Chelton, 1984; Lynn and Simpson, 1987; Batteen and Vance, 1998).

Lynn and Simpson (1987) suggested that IC also has a strong seasonal variation and the variation signal corresponds with the signal of CUC in most locations. There is evidence that the IC is the "surfacing" of CUC in late fall when CUC is the strongest (Pavlova, 1966; Huyer and Smith, 1974). Tisch *et al*. (1992) also observed CUC reaching the surface during wind relaxation events.

## 2.5 Coastal Upwelling

CCS is one of the biggest upwelling regions in the world. Previous studies indicate that wind stress plays an important role in the upwelling of this area (Nelson, 1976; Rosenfeld *et al*., 1994; Shulman *et al*., 2002; Ramp *et al*., 2005; Shulman *et al*., 2009).

The dominant winds near central California come from the northwest. Prevailing northwesterly winds near central California are the strongest during spring and early

summer (March through June) and the weakest during late summer and early fall (Nelson, 1976; Rosenfeld *et al*., 1994). These winds drive Ekman transport to the right which is the offshore direction in the coastal area of central California (Tseng *et al*., 2005). To satisfy the continuity condition, the water transported away from shore has to be replenished, which causes the upwelling on the coast (Tracy, 1990).

There are two upwelling centers in the Monterey Bay area: Point Aňo Nuevo and Point Sur. Tracy (1990) determined the source of cold water in Monterey Bay using AVHRR satellite sequential images. The author suggested that the cold water is advected into the Bay from the upwelling center Point Aňo Nuevo. Rosenfeld *et al*. (1994) described the upwelling filaments originated at Point Aňo Nuevo (Fig. 1) using AVHRR and CTD data. They found a bifurcated flow off Point Aňo Nuevo. According to the authors, part of the upwelled water with low temperature and high salinity flows offshore and the other part advects southeast into the Bay over the Monterey Canyon (MSC). Their theory that the primary source of cold upwelled water is advected into the Bay from the north rather than local upwelling from MSC has been supported by evidence from many observational and numerical studies (Graham and Largier, 1997; Blencoe, 2001; Shulman *et al*., 2002; Ramp *et al*., 2005; Shulman *et al*., 2009).

Another upwelling center is located at Point Sur, south of the Monterey Bay (Fig. 1). Breaker and Mooers (1986) described the movement of filaments originating from Point Sur. They suggested that the upwelling front is an important factor for cross-shore variability during upwelling seasons. POST (Point Sur transect) data and NOAA AVHRR satellite image indicate that the cold filament from Point Sur flows offshore (Tisch *et al*., 1992). Mooring observations near Point Sur also shows offshore filaments and currents

present have intense temporal and spatial variations (Ramp *et al*., 1997).

Coastal upwelling filaments can be seen extending hundreds of kilometers across the shelf and slope into the deep ocean from high resolution satellite images, providing transport between the coastal area and the open ocean. Previous studies indicate that upwelling filaments can penetrate 100-200 meters deep, and the peak speed can reach 50-100 cm/s (Mooers and Robinson, 1984). Thus "the offshore and vertical fluxes of mass, heat, and biological materials associated with these filaments can therefore be substantial and are of likely importance to regional, and perhaps global, physical and biological balances" (Haidvogel *et al*., 1991, p. 15017).

In the study of the nature of the cold filaments in CCS, Strub et al. (1991) suggested three simplified conceptual models with the first one being "squirts model," the second one being "meso-scale eddy model," and the last one being "meandering jet model" (Fig. 4). "Squirts" are one-way jets generated by near-shore convergences and transport cold, salty coastal upwelled water to the deep ocean. The "meso-scale eddy model" states that the recent coastal upwelled water can be carried away by a set of near-by eddies which usually have different directions of rotation. Strub pointed out that both "squirts model" and "meso-scale model" can generate similar surface temperature structures, but the underlying mechanisms of these two models are different. "Squirt" jets are generated by near-shore convergences while the jet-like structures in "eddy model" are generated by meso-scale eddies. The last conceptual model "meandering jet" includes the idea that an uninterrupted meander draws upwelled water from the coast by flowing on and off shore along the coast. By analyzing the CTZ and NCCCS surveys, Strub excluded the "squirts model" for CCS between $36^{o}$N and $42^{o}$N because most of the evidence they collected

does not support this conceptual model. Most of their studies, however, were concentrated in the area between 39°N and 42°N while Monterey Bay is close to 36.6°N.

Haidvogel *et al*. (1991) simulated the production of filaments in California coastal regional by using a primitive equation model. Their results are consistent with Strub's three filament-generation models. In addition, their model results show that several factors (e.g., shelf-slope topography, coastal geometry, equatorward currents and coastal upwelled water) are "all involved in the formation and subsequent evolution of filaments in the coastal transition zone" (Haidvogel, p. 15039). Their study, however, neglected several physical restrictions, such as direct wind forcing, remote influence from outside of the model region and the variation of coriolis parameter $f$.

An area of higher surface temperature was found at the northeast corner of the Monterey Bay during upwelling events, termed "upwelling shadow" (Graham, 1993, p. 83; Graham and Largier, 1997). According to Graham (1993), the existence of an "upwelling shadow" is the result of the warming of water which is trapped in the northern Bay due to the slow recirculation of near-shore flow. Graham and Largier (1997) built a conceptual dynamical model of the Monterey Bay upwelling shadow. The model states that upwelled water separates from the coast during wind relaxation period and gets transported into the curved coastline (northern Bay) where reversed alongshore flow (cyclonic current) occurs due to cross-stream diffusion of momentum and local pressure gradients. The trapped upwelled water thus has an increased residence time and warms up rapidly because of large atmospheric heat fluxes. When the trapped water meets newly upwelled water, a thermal front is generated, which, in turn, prevents the trapped water from mixing out of the northern Bay and hence the generation of the upwelling shadow.

This model provides an indirect angle concerning the circulation pattern inside the Monterey Bay during upwelling events.

The movement of upwelling filaments is a mirror of the regional circulation and near-shore currents. However, there is still a long way to go to fully understand the detailed mechanism of circulation in the Monterey Bay region since current data are usually sparse in the ocean. The most temporally and spatially extensive current observation system in this region by far is the HF radar (Paduan and Cook, 1997; Paduan and Graber, 1997). Paduan and Cook (1997) described the evolution of upwelling filaments after wind reversal using HF low-pass-filtered current maps. They noted that by adjusting the frequency, HF radar has the capability to distinguish whether the movements are caused by tidal effect or wind forcing. Like other remote sensed observational methods, HF current observations, however, are limited to the surface of the ocean.

## 2.6 Monterey Bay Eddy (MBE)

Although the dominant flows of CCS are CC, CUC and IC, they are not the only feature in CCS system. Mesoscale eddies, meanders, filaments and fronts are observed over the entire CCS system, which increases the variability of CCS (Chelton, 1984; Batteen and Vance, 1998). Near central California, there exists an anticyclonic warm core eddy right outside of Monterey Bay with a diameter of 50-100 km (Breaker and Broenkow, 1994). Rosenfeld *et al*. (1994) also observed this eddy from AVHRR images. Using the AVHRR images, Ramp *et al*. (1997) found a warm anticyclonic eddy located offshore of Monterey Bay. The eddy was bounded by cold water upwelled from Point Aňo Nuevo at the northern end and cold filaments extending from Point Sur at the

southern end. Evidence exists that this warm core eddy is the meander of CC and is also known as the Monterey Bay Eddy (MBE), an important feature of the meandering CCS (Rosenfeld *et al*., 1994; Paduan and Rosenfeld, 1996; Ramp *et al*., 2005). AVHRR images indicate that this meander of CC has the tendency to detach from CC and becomes an eddy (Rosenfeld *et al*., 1994), but Ramp *et al*. (1997) argued that whether this feature has detached from CC or not is still not clear. Mooring observations suggest that the flow speed of the eddy can reach 20 cm/s and it can penetrate as deep as 1000 m (Ramp *et al*., 1997). Unlike the local upwelled cold and salty water, MBE carries warm and fresh water which originates from the Pacific Subarctic (Rosenfeld *et al.*, 1994).

Rosenfeld *et al*. (1994) provided a possible mechanism concerning the generation of MBE. Their hypothesis is that MBE is generated and maintained by the vorticity produced by the cold upwelling plumes from the two upwelling centers: Point Aňo Nuevo and Point Sur. The equatorward momentum of the cold plume from Point Aňo Nuevo and offshore momentum of the plume from Point Sur combine together and drive the anticyclonic flow of the meander. This is why the diameter of MBE approximately coincides with the distance between Point Aňo Nuevo and Point Sur. It also explained why MBE is bounded by cold water upwelled from both points. Rosenfeld et al. also noted that this eddy is "anchored" at this specific location because it has to be driven by the momentums of the plumes mentioned above.

MBE is not quiescent. Although Ramp *et al*. (2005) suggested that MBE is not generated by local wind stress, they noted that its movement does respond to wind. MBE was observed to move offshore during upwelling-favorable (northwesterly) wind periods and to move onshore during wind relaxation events (Rosenfeld *et al*., 1994; Ramp *et al*.,

2005). Abnormal onshore translation of MBE, however, was also found by moored observations, which didn't respond to wind forcing as usual (Ramp *et al*., 1997). The nature of this abnormal onshore translation of MBE is still not well understood. The onshore and offshore movements of MBE can cause sudden change of water properties. Mooring observations indicate that sea surface temperature fluctuates as much as ~1$^{o}$C during MBE moving onshore and offshore (Ramp *et al*., 1997). Ramp *et al*. (1997) observed a phenomenon that mooring temperature decreases more rapidly when MBE moves offshore than it increases when MBE moves onshore. They provided three possible explanations. The first explanation is that MBE may have moved offshore more rapidly than it progressed onshore. The second one is that MBE sharpened the horizontal temperature gradient when it moved onshore, which resulted in a quicker temperature drop when it retreated offshore. The last explanation is that the dropping of temperature was affected by the near shore upwelling plume. Besides sudden change of temperature, they also found a "pulse-like" poleward flow off Point Sur, which, they claim, might be related to the onshore translation of MBE.

Combining aircraft, ADCP and HF radar data, Ramp *et al*. (2005) described the regional circulation near central California coast during upwelling and relaxation events in August, 2000. They noticed mooring velocity direction changed as MBE moved onshore and velocity profiles collected near MBE showed barotropic flows in the upper layer (upper 240 m). The front of MBE was roughly defined as 14.0$^{o}$-14.5$^{o}$C in their study. An onshore translation speed of 0.05 degrees of longitude per day (about 5 km/day) was observed when MBE approached the coast during a relaxation event.

## 2.7 Numerical Model Studies

Oceanic observation technology has made great progress nowadays, but available oceanic data is still relatively sparse. Even with temporally and spatially extensive observation networks like HF radar or satellite, they can only cover the surface ocean and a small region at a time. Numerical methods, such as ocean modeling and data assimilation, proved to be useful in simulating ocean phenomena and generating additional information when there is not enough data available. The Monterey Bay region is one of the most attractive sites for ocean modeling and data assimilation because it possesses unique features like a complex coastline and bathymetry, interaction of Bay water masses with the Pacific Ocean and numerous local upwelling events.

Using a primitive equation (PE) model with sigma coordinate, irregular basin geometry and finite bottom topography, Haidvogel *et al*. (1991) explored the production and evolution of filaments in California coastal region. Based on cross-filament length scale (~70-80 km), cross shelf penetration distance (~300 km), life time (30-50 days), current speed and transport of the filaments, they considered the simulated filaments to be similar to those observed in the real ocean. Their model results show that the generation and evolution of cold filaments are a combined result of topography, coastal geometry, equatorward currents and the existence of coastal upwelled water.

Batteen (1997) analyzed the generation, evolution and maintenance of currents, meanders and eddies in the CCS using a multi-level nonadiabatic PE model which was driven by a temporally and spatially varying wind field. The model was designed for an eddy-resolving, limited-area eastern boundary currents (EBC) system. To analyze the baroclinic instability, the model was set to 10 layers. The model adapted primitive

equations on a β plane and was based on the hydrostatic and Boussinesq approximations. The climatological (1980-1989) ECMWF wind data was used to drive the model. In their experiments, types of wind field were the most important variable. In other words, different types of wind fields were used to trigger currents, meanders and eddies in the CCS. Model results showed that wind forcing can set up both equatorward CC and poleward CUC. Batteen suggested that barotropic and baroclinic instabilities play an important role in generating meanders, eddies, jets and coastal filaments. The involvement of β plane is an important factor for the currents to become barotropically and baroclinically unstable. In addition, his model results indicated that the irregularities of the coastline had an "anchoring" effect for upwelling and development of filaments.

Batteen *et al*. (1995) demonstrated the importance of salinity to the regional circulation of CCS. Batteen and Vance (1998) incorporated thermohaline gradients into the model used by Batteen (1997) and analyzed the effects of both wind forcing and salinity on the CCS. They concluded that while wind forcing was still the dominant effect on CCS, thermohaline gradients were responsible for the generation of a poleward surface current and an equatorward undercurrent in the northern end of the model region. In addition, thermohaline gradients also caused a temperature front and surface current between Cape Mendocino and Point Arena. Batteen *et al*. (2003) used the same model but with an expanded domain (from the original 35$^{o}$N to 22.5$^{o}$N) and thus were capable of analyzing the entire CCS from Baja to the border of US and Canada. From the cross-shore sections of meridional velocity, they found that barotropic and baroclinic instabilities of CC and CUC can cause the generation of eddies in CCS. According to Batteen *et al*. (2003), the combined effects of wind forcing, seasonal thermohaline

gradients and irregularities of the coastline are responsible for the generation and evolution of CC, CUC, IC and even the meanders, eddies, and filaments which are superimposed on the major currents.

Shulman *et al*. (2002) coupled a regional high resolution model (Innovative Coastal-Ocean Observing Network model, or ICON) with a larger scale model (Pacific West Coast model, or PWC), and demonstrated a new way to set up more accurate and sophisticated open boundary conditions. ICON is based on a 3-dimensional coastal ocean model described by Blumberg and Mellor (1987). It has 30 sigma layers and adopts primitive equations of momentum, heat and salt. The Meller-Yamada and Smagorinsky closure scheme is used for horizontal mixing in ICON. ICON is one-way coupled (the information of PWC affects ICON while the information of ICON doesn't affect PWC) with a larger scale model PWC which is also a Blumberg and Mellor, sigma coordinate based model. Specifically, at the open boundaries, the barotropic and baroclinic velocity components of ICON are determined by PWC output and radiation conditions, respectively. They noted that the adoption of cross-shelf open boundaries which are almost orthogonal to the isobaths of the bathymetry is the key to successfully transfer information from PWC into ICON.

Paduan and Shulman (2004) assimilated HF radar data into the ICON model over the Monterey Bay region. Since the HF radar only covers the ocean surface, it is critical to find a way to transfer the surface information downward. They solved this problem by connecting HF radar-derived surface velocities to the "corrections" in the model wind-forcing. This is realized by adding a pseudo-shearing wind stress (can be calculated from the difference between HF radar-derived velocity and model velocity using an optimal

algorithm) to the model wind stress. The 3-dimensional Physical-space Statistical Analysis System (PSAS) data assimilation scheme (Cohn *et al*., 1998) was used to estimate the difference between HF radar-derived surface velocity and model predicted velocity. The corrections derived from PSAS scheme were connected to model wind forcing by the conservation of energy law and Ekman theory. By assimilating HF radar velocity data, ICON model predictions were greatly improved, especially on the upper 120 water levels.

Tseng *et al*. (2005) argued that previous numerical studies may have missed non-hydrostatic (NHY) effects by omitting NHY terms in hydrostatic (HY) primitive equations used in numerical models. The fact that bottom topography is rather steep in Monterey Bay region because of the presence of MSC has introduced a great obstacle during modeling, because NHY terms may be important in such regions. They thus compared a hydrostatic model with a non-hydrostatic model in order to examine the influence of the non-hydrostatic factors in a numerical coastal ocean simulation. The non-hydrostatic model they used is called "Monterey Bay Area Regional Model" (MBARM), which is based on $4^{th}$ order Dietrich/Center for Air-Sea Technology with z-coordinate, mixed Arakawa A and C grid. On the open boundaries, MBARM is one-way coupled with a larger-scale CCS DieCAST model. The model adopted the rigid lid approximation and used a so-called Ghost Cell Immersed Boundary Method (GC-IBM) to accurately represent bottom topography around Monterey Bay area, which avoids using stair-case approximation to simulate the complex topography of this region. The results showed that the existence of MSC and Sur Ridge causes the non-hydrostatic effects over the Monterey Bay region. They noted that the idealized smooth geometry and topography

used in previous studies are incapable of representing the steep topography like the MSC and the hydrostatic approximation in previous ocean models can cause artificial currents and eddies. The authors further concluded that non-hydrostatic models are recommended when dealing with circulations in Monterey Bay area.

In their study of the circulation in Monterey Bay, Shulman *et al*. (2007) used Navy Coastal Ocean Model (NCOM), which is based on Princeton Ocean Model (POM, Blumberg and Mellor, 1987), to hindcast the circulations during upwelling and relaxation events. NCOM is a primitive equation based ocean model with options of using sigma or hybrid coordinates (sigma coordinates in the upper layers and z coordinate in the lower layers). In their model settings, a hybrid vertical grid with 19 sigma layers (from surface to 138 m) and 21 z-levels (from 138 m to the bottom) is adopted for the global NCOM model and regional NCOM CCS model. The global NCOM model provides the regional NCOM CCS model with open boundary conditions, and the results of NCOM CCS provides open boundary values to a high resolution NCOM ICON model specifically designed for the Monterey Bay area. It has a curvilinear orthogonal grid with 1-4 km resolution and 30 sigma levels in the vertical dimension. The atmospheric forcing driving NCOM is from the Coupled Ocean-Atmosphere Mesoscale Prediction System (COAMPS) atmospheric model. Two versions of COAMPS with different surface fluxes and microphysics parameterizations were used to drive NCOM in their experiments. They found that the weakening of wind stresses in the 9km version of COAMPS can result in artificial flows in the domain. The overestimation of short wave radiation (SWR) predicted by COAMPS was noted. The authors pointed out that the overestimation of SWR caused higher temperature values by NCOM as compared with mooring

observations. The warming of surface waters near shore due to the onshore translation of MBE during a wind relaxation event was successfully reproduced by NCOM.

Over the last 10 years, many observational networks have been set up in the Monterey Bay area. Over a dozen Spray and Slocum gliders (Sherman *et al*., 2001; Webb *et al*., 2002) were deployed into the Monterey Bay area, collecting temperature and salinity profiles in August 2003. Shulman *et al*. (2009) assimilated this glider data into NCOM using the Navy Coupled Ocean Data Assimilation (NCODA) data assimilation system (Cummings, 2005). The model settings of NCOM is close to those used by Shulman *et al*. (2007). NCODA is an optimal interpolation (OI) based data assimilation system capable of assimilating temperature, salinity, geopotential and velocity. The BECs of NCODA are produced by multiplying the BEC with a correlation value derived from a second order auto-regressive (SOAR) function (Cummings, 2005). The BECs vary spatially (both horizontally and vertically) and are time dependent. The BECs are estimated from the difference between model results and NCODA analysis at every time step (Shulman *et al*., 2009). To correct the SWR overestimation from COMAPS (Shulman *et al*., 2007), the model predicted SWR values are replaced by observation values. According to Shulman *et al*., both hindcasts and nowcasts of temperature, salinity and velocity fields are all improved by combining the observational values of SWR and assimilating glider data. The authors noted that to further improve forecasts, a reliable and accurate atmospheric forcing is needed.

Building a tidal model for Monterey Bay is deemed difficult since barotropic tides can interact with complex bathymetry or interact with other movements of different frequencies (Rainville and Pinkel, 2006). ROMS, a 3-dimensional, one-way nested

community model with horizontal curvilinear coordinates and vertical sigma coordinates was used to model tides in the Monterey Bay area (Wang *et al*., 2009). There were three nested domains in their model. The largest domain covers the west coast of the United States. The second domain, which is part of the first domain, covers the Central and Northern California coast. The third domain, part of the second domain, covers the Monterey Bay. According to the authors, this kind of nesting enables the exchange of boundary conditions between three domains. Eight tidal constituents, $M_2$, $K_1$, $O_1$, $S_1$, $N_2$, $P_1$, $K_2$, $Q_1$, were used at the boundary for tidal forcing. The simulation results were successful when compared with observations. The authors noted that realistic stratification is critical to simulate barotropic and baroclinic tides.

Haley, Jr *et al.* (2009) presented the results of numerical studies of the Monterey Bay using Harvard Ocean Prediction System (HOPS; Robinson *et al*., 2002). HOPS is a primitive equation based dynamical model with space-average grids, sigma coordinate system. Like NCOM, HOPS is also driven by COAMPS grid products. In their experiments, a data assimilation scheme based on Optimal Interpolation was used to assimilate gliders, aircraft, AUVs and ships measurements. They evaluated the model predictive skill and assimilation skill in real time by RMS estimation. By assimilating data from various sources, the circulation, temperature and salinity fields predicted by HOPS were all improved. The authors concluded that the reanalysis of model results allows for a detailed description of the ocean features which occurred during the Autonomous Ocean Sampling Network-II (AOSN-II) in 2003 to be made.

## 2.8 Data Assimilation Studies

The earliest forms of data assimilation were simple analyses before the existence of

computers (about the middle of the 20th century). In the 1960s and 1970s, statistics were introduced into data assimilation in order to adapt to the need of meteorological application, especially in weather forecasting. Optimal Interpolation (OI) became popular during this period (Gandin, 1965). Even today, OI is still one of the most important data assimilation methods, especially for mapping data onto regular grids. By specifying prior information of state vector and observations, one can estimate the optimal value of a variable on a given grid point using OI. It has been recognized, however, that there exists limitations of OI implementation. For example, it is difficult to specify prior multivariate error statistics when one tries to incorporate existing OI scheme with a newly developed model (Brasseur and Verron, 2006). To overcome this problem, many institutions switch their data assimilation systems from OI to variational approaches in the 1980s and 1990s. Over the last 20 years, numerous data assimilation techniques were transplanted from meteorology to oceanography, accompanying the rising use of various ocean models.

Nowadays, there are many data assimilation methods for oceanic applications. Besides OI, ensemble-based methods and variational methods are also popular data assimilation methods.

Currently, most of ensemble-based data assimilation methods are evolved from or inspired by ensemble Kalman filter (EnKF; Evensen, 2003). EnKF is closely related to Kalman Filter (KF; Kalman, 1960), which assumes linear growth and Gaussian distribution of error (Hamill, 2006). Although the feature of calculating forecasts, analyses and their respective error covariances at the same time is attractive, the computational cost of error covariances is so high that the implementation of full KF is practically impossible (Tippett *et al*., 2003). Instead, ensemble forecast methods proved

to be feasible since the computational requirements for ensemble methods can be met by modern computer architecture (Toth and Kalnay, 1993). A variety of ensemble-based methods were proposed and applied in practical data assimilation systems. As one of these methods, EnKF estimates the forecast (or background) error covariance matrix from a set of parallel members (ensemble) which possess their own initial conditions, forecasts and analyses (Evensen, 1994, 2003). One of the advantages that distinguish EnKF from KF is the lower computational costs for estimating the BEC from the forecast ensemble. Because the accuracy of BECs lies on the ensemble, the way that an ensemble is generated becomes important. Given that there exists many different ways to generate ensembles, the assimilation results often vary, and the results of EnKF are hence suboptimal.

Other ensemble methods based on the Kalman Filter also have their own way to define and model error covariances. For example, Ensemble Kalman Square Root Filter (Kalman SRF) was found capable of reducing computational cost by avoiding the forming of full error covariance matrices (Tippett *et al*., 2003). Specifically, the forecast and analysis error covariance square root matrices were used to replace the original error covariance matrices in their algorithm. Kalman SRF is also subjected to "non-uniqueness" since the choice of ensemble is not unique (Tippett *et al*., 2003).

In addition to ensemble methods, variational data assimilation methodologies are also widely accepted. Variational methods, specifically the 3-dimensional variational method (3D-VAR) and 4-dimensional variational method (4D-VAR), were first proposed and applied in meteorology and then transplanted to oceanography in the 1980s. By minimizing the cost function, which represents the difference between the analysis and

the background state vector and the difference between the analysis and observations, one can inject the information from oceanic observations into a numerical model. Since variational methods can easily adapt to multivariate error statistic estimation, it is more convenient to incorporate existing variational schemes with modern oceanic models. The computational cost of most of the ensemble data assimilations schemes, however, grows linearly with the number of observations since these schemes sequentially deal with observations (Wang *et al*., 2007). Comparing with ensemble-based methods, variational data assimilation techniques can accommodate more data without dramatically adding computational burden and are thus preferred as operational schemes in many oceanographic institutions (Courtier *et al*., 1998; Weaver and Courtier, 2001; Wang *et al*., 2007; Dobricic and Pinardi, 2008; Li *et al*., 2008) like Naval Research Laboratory (NRL) and National Centers for Environmental Prediction (NCEP) because of the increasing amount of observations from all sorts of pools attributing to the improvement of observational technologies each year.

The statistics embedded in the BEC matrix and observational error covariance (OEC) matrix in the 3D-VAR cost function play a fundamental role in determining the spatial structure and amplitude of the increment of the state vector (Derber and Rosati, 1989). There is little knowledge, however, about these statistics since the ocean state is often poorly known without thorough investigation. Therefore, all BECs in variational data assimilation schemes must be modeled using different algorithms. As Weaver and Courtier (2001) said in their work on building correlation function on a sphere, estimation and representation of BECs is the “central task” in building a variational data assimilation system.

The way that BECs are modeled also vary. For example, Derber and Rosati (1989) suggested a BEC model using a Laplacian smoother in which the horizontal covariance between any two points can be determined by a near-Gaussian function. The horizontal distance and latitude of the grids determine the magnitude of covariances. Near the equator, horizontal distances were empirically stretched by a factor of 2.28 to account for longer east-west correlation scales at equatorial regions. The covariance model used, however, was limited to the 2D plane (i.e., ignoring vertical structure).

Weaver and Courtier (2001) built a classical BEC model (hereafter called WC model) on a sphere by solving the generalized diffusion equations (GDE) and extended this concept into 3D. The WC covariance model was designed specifically for the univariate component of BECs which represents auto-covariances between grid points with the same model variable (e.g., temperature) rather than the multivariate component of BEC (e.g., cross-covariance between grid points of different variables). The process of solving GDE serves as a BEC operator which results in 3D-isotropic and near-Gaussian covariances. By adding boundary conditions to the GDE, the BEC operator can adapt to the variability of the coastlines. Stretching coordinates with respect to the Laplacian operator in GDE allows for the forming of an anisotropic BEC model near the equator. The idea of building a BEC model in such way still has great influence for many data assimilation systems today.

Another BEC example is built by Dobricic and Pinardi (2008). In their numerical scheme, the BEC matrix was separated into horizontal and vertical modes, which were modeled as Gaussian functions and Empirical Orthogonal Functions (EOFs), respectively. By utilizing the dominant EOFs (in another word, discarding unimportant EOFs), the

rank of the BEC matrix was considerably reduced, resulting in the reduction of computational time. Although this configuration of BECs was transplanted from so-called SOFA (the System for Ocean Forecasting and Analyses) system (De Mey and Benkiran, 2002), it has more computational advantages in the 3D-VAR system since optimal interpolation (OI) used in SOFA is incapable of dealing with large amounts of data while the dominant factor of computational cost of 3D-VAR is the size of the model state vector, not the size of the data. The Gaussian horizontal covariances were modeled using a recursive filter in which variation of complicated coastlines are adapted. Furthermore, they introduced a barotropic model for the estimation of vertical covariances, capable of adapting complex bottom topography. The data assimilation results showed improvement as compared with the SOFA OI scheme.

Over the last decade, research into hybrid BEC model development has become one of the most attractive data assimilation topics (Hamill and Snyder, 2000; Etherton and Bishop, 2004; Buehner, 2005; Wang *et al*., 2007; Yaremchuk *et al*., 2011). In their studies of hybrid BEC data assimilation schemes, Wang *et al*. (2007, 2008, 2009) suggested that it is feasible to incorporate ensemble-based BEC schemes into existing variational schemes, and their results proved that hybrid schemes are more robust than traditional variational schemes.

Yaremchuk *et al*. (2011) proposed a hybrid 3D-VAR scheme assimilating glider data into Navy Coastal Ocean Model (NCOM). The flow-dependent part of the hybrid BEC in this scheme is estimated from an ensemble of model states. The ensemble of model states contains the statistics of NCOM integrations and respective forecasts and analyses. The static part of the hybrid BEC is derived by propagating the diffusion

equation for temperature and salinity. A semi-implicit scheme is applied to model the near-Gaussian propagator, which enhances the computational efficiency of the system (Weaver and Ricci, 2004; Yaremchuk *et al*., 2010). To retain the regional-scale error correlations, an explicit separation technique is adopted by restricting the action of static covariance to the null space of the flow-dependent covariance matrix. Both the twin data experiments and real data experiments showed improvement in the 12-hourly forecast with the hybrid scheme.

# CHAPTER III

# METHODS

## 3.1 Background

### *a. Optimal Interpolation*

Optimal Interpolation (OI), also known as Objective Analysis (Gandin, 1965), became popular as a mapping tool for weather forecasting in the 1960s and 1970s. OI is still used widely for interpolation and in data assimilation methods.

OI is based on Gauss-Markov theorem which provides a best linear unbiased estimate of the "true state" $\mathbf{x}$ (a variable that needs to be estimated) that is optimal in the sense of minimal error variance. Gauss-Marcov theorem states that the Best Linear Unbiased Estimator (BLUE) can be built as:

$$\mathbf{x}_{opt} = \langle \mathbf{x} \rangle + R_{xy} R_{yy}^{-1} \left( \mathbf{y} - \langle \mathbf{y} \rangle \right) \tag{3.2.1}$$

Where $\mathbf{x}_{opt}$ is the estimate of the "true state" $\mathbf{x}$. Covariance $R_{xy} = \left\langle (\mathbf{x} - \langle \mathbf{x} \rangle)(\mathbf{y} - \langle \mathbf{y} \rangle)^T \right\rangle$ and $R_{yy} = \left\langle (\mathbf{y} - \langle \mathbf{y} \rangle)(\mathbf{y} - \langle \mathbf{y} \rangle)^T \right\rangle$ and the means $\langle \mathbf{x} \rangle$, $\langle \mathbf{y} \rangle$ are assumed to be known, where $\langle \ \rangle$ denotes mathematical expectation.

Using Gauss-Marcov theorem, the OI estimator can be built as follows. The observations $\mathbf{y}$ can be expressed as:

$$\mathbf{y} = \boldsymbol{H}\mathbf{x} + \mathbf{n} \tag{3.1.2}$$

where $\mathbf{n}$ is the noise in observations. $\boldsymbol{H}$ is the linearized observation operator, projecting $\mathbf{x}$ onto observation points.

Suppose that the noise is an uncorrelated Gaussian random variable with zero mean, then:

$$\langle \mathbf{y} \rangle = \boldsymbol{H} \langle \mathbf{x} \rangle \Rightarrow \mathbf{y}' = \boldsymbol{H}\mathbf{x}' + \mathbf{n} \tag{3.1.3}$$

where $\mathbf{x}' = \mathbf{x} - \langle \mathbf{x} \rangle$, $\mathbf{y}' = \mathbf{y} - \langle \mathbf{y} \rangle$.

Given that $\langle \mathbf{x}'\mathbf{n} \rangle = 0$, we have:

$$\begin{aligned} R_{yy} &= \langle (\mathbf{y} - \langle \mathbf{y} \rangle)(\mathbf{y} - \langle \mathbf{y} \rangle)^T \rangle \\ &= \langle (\boldsymbol{H}\mathbf{x}' + \mathbf{n})(\boldsymbol{H}\mathbf{x}' + \mathbf{n})^T \rangle \\ &= \boldsymbol{H} \langle \mathbf{x}'\mathbf{x}'^T \rangle \boldsymbol{H}^T + \langle \mathbf{n}\mathbf{n}^T \rangle \\ &= \boldsymbol{H}\mathbf{B}\boldsymbol{H}^T + \mathbf{R} \end{aligned} \tag{3.1.4}$$

where $\mathbf{B} = \langle \mathbf{x}'\mathbf{x}'^T \rangle$ is the BEC, $\mathbf{R} = \langle \mathbf{n}\mathbf{n}^T \rangle$ is the observation error covariance (OEC), and

$$R_{xy} = \langle \boldsymbol{x}'\boldsymbol{y}'^T \rangle = \langle \boldsymbol{x}'\boldsymbol{x}'^T \rangle \boldsymbol{H}^T = \mathbf{B}\boldsymbol{H}^T \tag{3.1.5}$$

Using (3.1.1), (3.1.4) and (3.1.5), the optimal interpolation estimator can be written as:

$$\mathbf{x}_{opt} = \langle \mathbf{x} \rangle + \mathbf{B}\boldsymbol{H}^T \left( \boldsymbol{H}\mathbf{B}\boldsymbol{H}^T + \mathbf{R} \right)^{-1} \left( \mathbf{y} - \langle \mathbf{y} \rangle \right) \tag{3.1.6}$$

By denoting $\langle \mathbf{x} \rangle$ as the background field $\mathbf{x}_b$ and $\langle \mathbf{y} \rangle$ as $\boldsymbol{H}\mathbf{x}_b$, (3.1.6) can be rewritten as:

$$\mathbf{x}_{opt} = \mathbf{x}_b + \mathbf{B}\boldsymbol{H}^T \left( \boldsymbol{H}\mathbf{B}\boldsymbol{H}^T + \mathbf{R} \right)^{-1} \left( \mathbf{y} - \boldsymbol{H}\mathbf{x}_b \right) \tag{3.1.7}$$

If the background field $\mathbf{x}_b$, BEC $\mathbf{B}$ and OEC $\mathbf{R}$ is specified, the optimal estimate of the "true state" $\mathbf{x}$ can be obtained using (3.1.7).

OI directly calculates gain matrix (or weight matrix): $\mathbf{B}\boldsymbol{H}^T \left( \boldsymbol{H}\mathbf{B}\boldsymbol{H}^T + \mathbf{R} \right)^{-1}$. During this process, the matrix $\left( \boldsymbol{H}\mathbf{B}\boldsymbol{H}^T + \mathbf{R} \right)^{-1}$ has to be inverted in one way or another.

There is a group of sequential data assimilation methods based upon the OI procedure. These methods use the model solution (forecast state) at the time moment of

observations as a background field for the OI of observations. The BEC in this method is assumed to be known, and in most cases it does not change in time. The result of OI is called the analysis state and the model is restarted from the analysis state. This procedure is applied sequentially as new data becomes available. Sequential OI is a simplified version of the Kalman Filter (KF). KF not only prognoses the state of the ocean (implementation of OI), but also propagates the model forecast error covariances (BECs) in time. Although the feature of calculating forecasts, analyses and their respective error covariances at the same time is attractive, the computational cost of error covariances is so high that the implementation of a full KF is impractical (Tippett *et al*., 2003). Instead, ensemble-based methods proved to be feasible since the computational requirements for ensemble methods can be met by modern computer architecture (Toth and Kalnay, 1993). A variety of ensemble-based methods were proposed and applied in practical data assimilation systems. As one of these methods, Ensemble Kalman Filter (EnKF) estimates the forecast error covariance matrix from a set of ensemble members derived from the model integration (Evensen, 1994, 2003). Another example is Ensemble Optimal Interpolation (EnOI), which uses stationary ensembles to estimate forecast error covariance. EnOI is regarded as an approximation of EnKF.

*b. 3-Dimensional Variational Data Assimilation*

Variational methods, specifically the 3-dimensional variational method (3D-VAR) and 4-dimensional variational method (4D-VAR), were first proposed and applied in meteorology and then transplanted to oceanography in the 1980s. The process of obtaining analyses using variational methods is usually achieved by minimizing a "cost function." The cost function represents the difference between the analysis and

background state vector and the difference between the analysis and observations.

3D-VAR is based on Bayesian statistics. Let X be model realizations and Y be the realization of observations. The Bayesian formulation for the optimal estimate of X given Y is:

$$P(X|Y) = \frac{P(Y|X)P(X)}{P(Y)} \tag{3.1.8}$$

where $P(X|Y)$ is the conditional probability of X given Y. $P(Y|X)$ is the conditional probability of Y given X. $P(X)$ and $P(Y)$ are unconditional probabilities of X and Y.

Take the log of (3.1.8):

$$-\log P(X|Y) = J(\mathbf{x}) = -\log P(Y|X) - \log P(X) + \log P(Y) \tag{3.1.9}$$

Assuming the probability density functions are Gaussian:

$$P(Y|X) = \exp\left[-\frac{1}{2}(\mathbf{y}-\mathrm{H}\mathbf{x})^T \mathbf{R}^{-1}(\mathbf{y}-\mathrm{H}\mathbf{x})\right] \text{and} \tag{3.1.10}$$

$$P(X) = \exp\left[-\frac{1}{2}(\mathbf{x}-\mathbf{x}_b)^T \mathbf{B}^{-1}(\mathbf{x}-\mathbf{x}_b)\right], \tag{3.1.11}$$

where **B** and **R** are the BEC and OEC, respectively. H is the observation operator.

Given that $P(Y)$ is a pre-known number for observations, then $\log P(Y)$ can be neglected in (3.1.9). Using (3.1.9), (3.1.10) and (3.1.11), we have the cost function for 3D-VAR:

$$J(\mathbf{x}) = \frac{1}{2}\left[\left(\mathbf{x}-\mathbf{x}_b\right)^T \mathbf{B}^{-1}\left(\mathbf{x}-\mathbf{x}_b\right) + \left(\mathbf{y}-\mathrm{H}\mathbf{x}\right)^T \mathbf{R}^{-1}\left(\mathbf{y}-\mathrm{H}\mathbf{x}\right)\right] \tag{3.1.12}$$

where $\mathbf{x}$ represents model state vector and $\mathbf{x}_b$ is the background state vector.

The cost function is minimized by equating its gradient (with respect to **x**) to 0:

$$\delta\mathbf{x} = \mathbf{x} - \mathbf{x}_b = \left[\mathbf{B}^{-1} + \mathbf{H}^T\mathbf{R}^{-1}\mathbf{H}\right]^{-1}\mathbf{H}^T\mathbf{R}^{-1}\left[\mathbf{y} - \mathrm{H}(\mathbf{x}_b)\right] \qquad (3.1.13)$$

Equation (3.1.13) is often called the model space formulation of the variational problem (3.1.12). The observational operator H is assumed to be linear: $\mathrm{H}(\mathbf{x}) = \mathrm{H}(\mathbf{x}_b) + \boldsymbol{H}(\mathbf{x} - \mathbf{x}_b)$.

If $\mathbf{B}^{-1}$ is the full rank, its "dual form" can be written as:

$$\delta\mathbf{x} = \mathbf{x} - \mathbf{x}_b = \mathbf{B}\boldsymbol{H}^T\left[\boldsymbol{H}\mathbf{B}\boldsymbol{H}^T + \mathbf{R}\right]^{-1}\left[\mathbf{y} - \mathrm{H}(\mathbf{x}_b)\right] \qquad (3.1.14)$$

which coincides with (3.1.7) presenting the OI solution.

Equation (3.1.14) is often called the data space formulation of the variational problem (4.12). Solving (3.1.13) is difficult because it requires solving the linear system in model space, which usually has much more dimensions than the data space. In addition, the estimation of **B** from the data is usually easier than estimation of $\mathbf{B}^{-1}$.

In equation (3.1.14), under the assumption that the state is observed in every point ($\boldsymbol{H} = \boldsymbol{E}$) the magnitude of $\mathbf{B}\boldsymbol{H}^T[\boldsymbol{H}\mathbf{B}\boldsymbol{H}^T+\mathbf{R}]^{-1}$ is defined by **B** and **R**. When the model error is large ($\mathbf{B} >> \mathbf{R}$), the magnitude of $\mathbf{B}\boldsymbol{H}^T[\boldsymbol{H}\mathbf{B}\boldsymbol{H}^T+\mathbf{R}]^{-1}$ tends toward 1. In this case, $\delta\mathbf{x} \approx [\mathrm{y} - \mathrm{H}(\mathbf{x}_b)] = \delta\mathbf{y}$. In this case, the increment of state vector is defined by the model-data misfit, which means the model results cannot be trusted. When the data error is large ($\mathbf{R} >> \mathbf{B}$), the magnitude of $\mathbf{B}\boldsymbol{H}^T[\boldsymbol{H}\mathbf{B}\boldsymbol{H}^T+\mathbf{R}]^{-1}$ tends toward 0. In this case, the data is no longer trustworthy.

The normal equation (3.1.14) is usually solved using the descent algorithm which requires a number of iterations in 3D-VAR. The matrix $\mathbf{B}\boldsymbol{H}^T[\boldsymbol{H}\mathbf{B}\boldsymbol{H}^T+\mathbf{R}]^{-1}$ is equivalent to the gain matrix in OI. Thus, 3D-VAR and OI solve the same problem using different methods. 3D-VAR avoids directly calculating the gain matrix by seeking the analysis in the way of iteration to minimize the cost function (3.1.12).

In addition to the iterative "descent" algorithm, variational problems can also be

solved using the method of "representers" (Bennett, 1992, p. 136). Variational problems can be formulated in the form of the Euler-Lagrange equation system, composed of forward and adjoint models. The forward model is integrated forward in time while the adjoint model propagates the state vector backward in time. The method of "representers" states that the optimal solution of the Euler-Lagrange equations is the sum of a first guess and a linear combination of representers. The matrix of representers can be obtained in the following way: (a) project the orthogonal basis (in the linear space of data vectors) backward in time using the adjoint model; (b) integrate the forward model using the results from (a) as the initial condition (the result of this step is a representer for an observation point); (c) repeat (a) and (b) until all the vectors of representers are ready. The representer shows the influence all observational points to the unit model-data misfit in observational point m. Formally, the method of representers results in the solution given by the equation (3.1.14) coinciding with the OI solution.

*c. Hybrid BEC*

The BEC **B** is a matrix with typical dimensions of $10^6 \times 10^6$. It is impractical to manipulate such a huge matrix during computation. Hence, **B** is often modeled as an operator. Although there are many algorithms for modeling **B**, their purpose is the same: building BECs on a Gaussian or near-Gaussian function in one way or another (Courtier *et al*., 1998; Weaver and Courtier, 2001; Weaver and Ricci, 2004; Dobricic and Pinardi, 2008; Li *et al*., 2008). Since the BECs modeled in traditional variational schemes are normally time-independent, they are often referred to as "static" or "stationary" BECs. Nonetheless, in coastal regions like Monterey Bay, a static BEC model might not be able to reflect real ocean dynamics since coastal ocean states are often affected by many

factors, such as tidal effects, bottom topography and large scale circulation (Wang *et al*., 2008; Yaremchuk *et al*., 2011).

Ensemble-based assimilation methods, on the other hand, provide another kind of BEC. Because the BECs in ensemble-based techniques are estimated from a set of ensembles (e.g., ensemble of forecasts) that evolve with time. The error statistics also propagate temporally. This kind of BEC is known as "flow-dependent" BECs. It is a common presumption that ensemble-based techniques are capable of generating flow-dependent BECs, which control the proper weighting of the background field and observations (Wang *et al*., 2007). Pure flow-dependent BECs also have their limitations. For example, the results of ensemble-based schemes often vary with different sets of ensembles. Hence, ensemble-based methods are sub-optimal.

To improve performance of regional 3D-VAR data assimilation algorithms, hybrid BEC models have been under extensive development during the last decade (Hamill and Snyder, 2000; Etherton and Bishop, 2004; Buehner, 2005; Wang *et al*., 2007). The major idea of the hybrid approach is to represent the BEC matrix by a weighted sum of the flow-dependent covariance derived from the ensemble of model integrations and the "static" covariance represented by an operator with a smoothing kernel. By tuning the covariance weights, Wang *et al*., (2007, 2008, 2009) have demonstrated that hybrid schemes can produce more accurate results than traditional variational schemes and are capable of improving predictability of the atmospheric models by 5-15%.

The BECs in the following 3D-VAR system are also composed of two parts. The first part is the static, or stationary BEC, which is modeled by a near Gaussian correlation function. The second part is the flow-dependent BEC, which is derived from the statistics

of the ensemble of model states. Hence, the 3D-VAR system described below is termed "hybrid."

## 3.2 Hybrid 3D-VAR System

The goal of applying a 3D-VAR assimilation scheme is to obtain the increment ($\delta\mathbf{x}$) of model state vector ($\mathbf{x}$) by minimizing the cost function:

$$J(\delta\mathbf{x}) = \frac{1}{2}\left[\delta\mathbf{x}^{\mathrm{T}}\mathbf{B}^{-1}\delta\mathbf{x} + (\boldsymbol{H}\delta\mathbf{x} - \delta\mathbf{y})^{\mathrm{T}}\mathbf{R}^{-1}(\boldsymbol{H}\delta\mathbf{x} - \delta\mathbf{y})\right] \rightarrow \min_{\delta\mathbf{x}} \tag{3.2.1}$$

where $\mathbf{B}$ is the M×M BEC matrix, $\mathbf{R}$ represents K×K OEC matrix, $\delta\mathbf{y}$ is the innovation vector, $\boldsymbol{H}$ denotes the linearized observational operator, projecting the model state $\mathbf{x}$ onto observations. For convenience, the cost function (3.1.12) is rewritten in the increment form (3.2.1).

The state vector $\mathbf{x}$ and increment $\delta\mathbf{x}$ could include temperature, salinity, velocity or other model variables at each grid point (only temperature and salinity in our case since the glider observations only consist of temperature and salinity data); hence, $\mathbf{x}$ and $\delta\mathbf{x}$ are multivariate. To define linear operations with multivariate vectors $\delta\mathbf{x}$, a diagonal matrix denoted as $\mathbf{G}$ is introduced**,** whose elements depend on the error variances of the fields (temperature and salinity) based on spatial coordinates. All the quantities in (3.2.1) are normalized by the respective error variances:

$$\delta\mathbf{x}_* \leftarrow \mathbf{G}^{-1/2}\delta\mathbf{x}, \quad \delta\mathbf{y}_* \leftarrow \mathbf{R}^{-1/2}\delta\mathbf{y}$$

To keep the cost function $J$ invariant, the matrices $\mathbf{B}$, $\boldsymbol{H}$ are transformed as:

$$\mathbf{B}_*^{-1} \leftarrow \mathbf{G}^{1/2}\mathbf{B}^{-1}\mathbf{G}^{1/2}, \quad \boldsymbol{H}_* \leftarrow \mathbf{R}^{-1/2}\boldsymbol{H}\mathbf{G}^{1/2}$$

Further below, the asterisks are dropped for convenience. The cost function (3.2.1) can now be rewritten as:

$$J(\delta\mathbf{x}) = \frac{1}{2}\left[\delta\mathbf{x}^{\mathrm{T}}\mathbf{B}^{-1}\delta\mathbf{x} + (\boldsymbol{H}\delta\mathbf{x} - \delta\mathbf{y})^{\mathrm{T}}(\boldsymbol{H}\delta\mathbf{x} - \delta\mathbf{y})\right] \tag{3.2.2}$$

The respective normal equation ($\partial J / \partial \delta\mathbf{x} = 0$) is:

$$\left[\mathbf{B}^{-1} + \boldsymbol{H}^{\mathrm{T}}\boldsymbol{H}\right]\delta\mathbf{x} = \boldsymbol{H}^{\mathrm{T}}\delta\mathbf{y} \tag{3.2.3}$$

For computational convenience, the hybrid BEC model is formulated in terms of the inverse covariances and has two terms scaled by the adjustable coefficients $\alpha$ and $\beta$:

$$\mathbf{B}^{-1} = \alpha\mathbf{B}_{\mathbf{m}}^{-1} + \beta\boldsymbol{P}_{\perp}\mathbf{B}_{0}^{-1}\boldsymbol{P}_{\perp}^{T} \tag{3.2.4}$$

The first term on the right hand side accounts for the flow-dependent part of the covariance ($\mathbf{B}_{\mathrm{m}}$), which is derived from the analysis of model statistics. Initially, model statistics is generated as an ensemble of model states from a free run. In the course of assimilation, at every analysis moment, the ensemble is updated by replacing the respective members of the free run by the forecasts initialized using this analysis. By applying eigenvector analysis or singular value decomposition (SVD) to the model state ensemble, $\mathbf{B}_{\mathbf{m}}$ can be expressed with the form:

$$\mathbf{B}_{\mathbf{m}} = \boldsymbol{P}\Lambda_{m}\boldsymbol{P}^{T} \tag{3.2.5}$$

where $\boldsymbol{P}$ is a $m \times M$ matrix whose $m$ columns are the eigenvectors $\mathbf{e}_k$ ($k$=1,…,$m$) of the sample covariance, and $\Lambda_{\mathrm{m}}$ is a $m \times m$ diagonal matrix whose diagonal elements are the variances of $\mathbf{e}_k$.

The second term in equation (3.2.4) is the static part of the BEC represented by projection of the inverse static covariance operator on the subspace orthogonal to $\mathbf{e}_k$: here $\mathbf{P}_{\perp} = \mathbf{I}_{M} - \boldsymbol{P}\boldsymbol{P}^{T}$ is the corresponding projector and $\mathbf{I}_M$ is the identity operator in state space. The static BEC operator $\mathbf{B}_0$ is modeled by integrating a generalized diffusion equation (Weaver and Courtier, 2001).

$$\mathbf{B}_0 = \exp(\rho^2 \mathbf{D}) \approx \exp(\tau \mathbf{D}) = \exp(\frac{1}{2}\tau \nabla \nu \nabla) \tag{3.2.6}$$

The parameter $\tau$ can be interpreted as "integration time" of the diffusion equation. The "integration time" $\tau$ plays the role of a global scaling parameter for the distribution of square of the mean decorrelation scale $\rho^2$ (see Appendix).

Equation (3.2.6) is approximated by an implicit "time integration scheme" (Yaremchuk *et al*., 2010, p. 24):

$$\mathbf{B}_0 = \exp(\tau \mathbf{D}) \approx \left[ \mathbf{I}_{\mathrm{M}} - \frac{\tau \mathbf{D}}{n} \right]^{-n} \tag{3.2.7}$$

where $\tau/n$ defines the implicit "time step" and $n$ is the explicit "time steps" (see Appendix). Based on the results of twin data experiments, the value of $\tau = 20$ and $n = 2$ were chosen for the scheme. An example of the action of static BEC $\mathbf{B}_0 = \exp(\tau \mathbf{D})$ is showed in Figure 4.

The inverse of $\exp(\tau \mathbf{D})$ which is required in the normal equation (3.2.3) has the form:

$$\mathbf{B}_0^{-1} = \exp(-\tau \mathbf{D}) \approx \left[ \mathbf{I}_{\mathrm{M}} - \frac{\tau \mathbf{D}}{n} \right]^{n} \tag{3.2.8}$$

The inverse of the flow-dependent BEC is defined as:

$$\mathbf{B}_{\mathbf{m}}^{-1} = \boldsymbol{P} \Lambda_{\mathbf{m}}^{-1} \boldsymbol{P}^{\boldsymbol{T}} \tag{3.2.9}$$

Hence, the inverse of the hybrid BEC can be written as:

$$\mathbf{B}^{-1} = \alpha \mathbf{B}_{\mathbf{m}}^{-1} + \beta \boldsymbol{P}_{\perp} \mathbf{B}_0^{-1} \boldsymbol{P}_{\perp}^{\boldsymbol{T}} = \alpha \boldsymbol{P} \Lambda_{\mathbf{m}}^{-1} \boldsymbol{P}^{\boldsymbol{T}} + \beta \boldsymbol{P}_{\perp} \exp(-\tau \mathbf{D}) \boldsymbol{P}_{\perp}^{\boldsymbol{T}} \tag{3.2.10}$$

The corresponding BEC can be expressed as follows:

$$\mathbf{B} = \frac{1}{\alpha} \boldsymbol{P} \Lambda_{\boldsymbol{m}} \boldsymbol{P}^{\boldsymbol{T}} + \frac{1}{\beta} \left[ \boldsymbol{P}_{\perp} \exp(-\tau \mathbf{D}) \boldsymbol{P}_{\perp}^{\boldsymbol{T}} \right]^{-1} \tag{3.2.11}$$

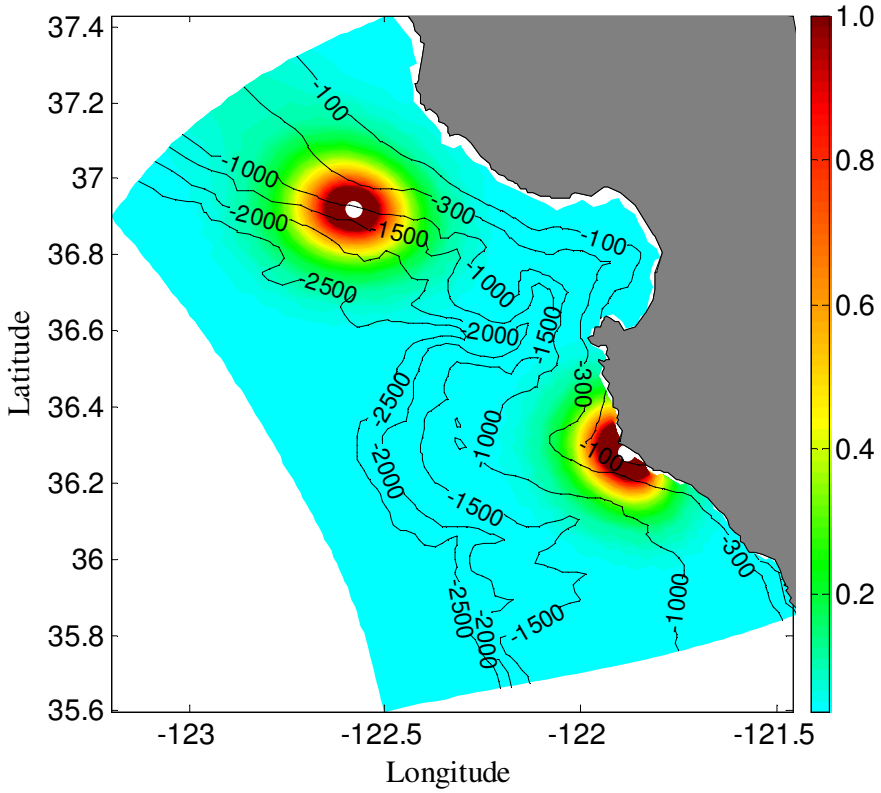


Figure 4. The action of static BEC $\mathbf{B}_0 = \exp(\tau\mathbf{D})$ on the $\delta$-shaped disturbances of temperature field at the two white points. $\exp(\tau\mathbf{D})$ is approximated by equation (3.2.7).

By constraining the action of $\mathbf{B}_0$ to the null space of $\mathbf{B}_m$, the static and flow-dependent parts of the BEC are statistically separated.

Using (3.2.10), the normal equation (3.2.3) now takes the form:

$$\left[\alpha \boldsymbol{P}\Lambda_{\boldsymbol{m}}^{-1}\boldsymbol{P}^{\boldsymbol{T}} + \beta\mathbf{P}_{\perp}\exp(-\tau\boldsymbol{D})\mathbf{P}_{\perp}^{\boldsymbol{T}} + \boldsymbol{H}^{\boldsymbol{T}}\boldsymbol{H}\right]\delta\boldsymbol{x} = \boldsymbol{H}^{\boldsymbol{T}}\delta\boldsymbol{y} \tag{3.2.12}$$

To solve this normal equation, the number of eigenvectors $m$, and the hybrid weighting coefficients $\alpha$ and $\beta$ have to be determined.

The optimal number $m$ of the eigenmodes is computed by the Bayesian information criterion (Schwarz, 1978). By minimizing the Bayesian function, the number of eigenvectors $m$ is determined:

$$C(m) = m + \frac{N}{\ln N}\ln\sigma_m^2 \;\rightarrow\; \min_m \tag{3.2.13}$$

where $\sigma_m$ represents the root mean square (RMS) of the error of $N$ data samples approximated by $m$ modes ($N > m$).

Knowing the dimension $m$ of subspace $\mathcal{R}^m$, the coefficient $\alpha$ is determined by minimizing (3.2.1) in the subspace spanned by $\mathbf{e}_k$. The approximate formula for the covariance matrix of the projection of $\delta\mathbf{x}$ on $\mathbf{e}_k$ is:

$$\left\langle \delta\boldsymbol{e}\delta\boldsymbol{e}^T \right\rangle = \left[\alpha\Lambda_m^{-1} + \boldsymbol{Q}\right]^{-1}\left[\frac{1}{\alpha}\boldsymbol{Q}\Lambda_m\boldsymbol{Q}^T + \boldsymbol{Q}\right]\left[\alpha\Lambda_m^{-1} + \boldsymbol{Q}\right]^{-1} \tag{3.2.14}$$

Note that matrix $\boldsymbol{Q} = \boldsymbol{P}^T\boldsymbol{H}^T\boldsymbol{H}\boldsymbol{P}$. $\delta\boldsymbol{e}$ is introduced such that $\delta\boldsymbol{x} = \boldsymbol{P}\delta\boldsymbol{e}$. Detailed deduction of (3.2.14) can be found in Appendix of Yaremchuk *et al*. (2011).

Given that background model errors are much larger than observational errors ($|\boldsymbol{Q}| >> \alpha|\Lambda_m^{-1}|$), (3.2.14) can be simplified as

$$\left\langle \delta\boldsymbol{e}\delta\boldsymbol{e}^T \right\rangle \approx \frac{1}{\alpha}\Lambda_m \tag{3.2.15}$$

$\alpha$ can then be estimated by minimizing the mean squared difference between the diagonal elements of $\left\langle \delta\boldsymbol{e}\delta\boldsymbol{e}^T \right\rangle$ and $\Lambda_m / \alpha$.

With known $m$ and $\alpha$, $\beta$ can be calculated using a technique which is used for computation of the inflation factor in the Kalman filter (e.g. Wang *et al*., 2007). This is accomplished by equating the trace of the sample forecast error covariance $\mathrm{Tr}\left\langle \delta\boldsymbol{y}\delta\boldsymbol{y}^T \right\rangle$ to the trace of $\boldsymbol{H}\boldsymbol{B}\boldsymbol{H}^T + \boldsymbol{I}_K$. Substituting B in equation (3.2.11) with the expression $\boldsymbol{H}\boldsymbol{B}\boldsymbol{H}^T$ gives:

$$\left\langle \delta\boldsymbol{y}^T\delta\boldsymbol{y} \right\rangle = \mathrm{Tr}\left[\frac{1}{\alpha}\boldsymbol{H}\boldsymbol{P}\Lambda_m\boldsymbol{P}^T\boldsymbol{H}^T + \frac{1}{\beta}\boldsymbol{H}\left[\mathbf{P}_\perp \exp(-\tau\boldsymbol{D})\mathbf{P}_\perp^T\right]^{-1}\boldsymbol{H}^T\right] + K \tag{3.2.16}$$

From (3.2.16), the final form of $\beta$ is:

$$\beta = \frac{\mathrm{Tr}\left\{ \boldsymbol{H}\left[ \mathbf{P}_{\perp} \exp(-\tau \boldsymbol{D}) \mathbf{P}_{\perp}^{\boldsymbol{T}} \right]^{-1} \boldsymbol{H}^{\boldsymbol{T}} \right\}}{\left\langle \delta \boldsymbol{y}^{\boldsymbol{T}} \delta \boldsymbol{y} \right\rangle - K - \mathrm{Tr}\left[ \boldsymbol{H} \boldsymbol{B}_{\boldsymbol{m}} \boldsymbol{H}^{\boldsymbol{T}} \right] / \alpha} \qquad (3.2.17).$$

## 3.3 Floating Temporal Window

Using the above hybrid 3D-VAR scheme, Yaremchuk *et al*. (2010) designed both twin data experiments and real data experiments. In these experiments, the assimilation interval was set to be 12 hours. As a newly developed method, more experiments are needed to test and solve the unaddressed problems of this hybrid system. For instance, only the data within 1-hour intervals near the model forecast moment were used in the assimilation; thus, at least 90% of glider data were excluded from the experiments with a 12-hour assimilation window. In addition, physical phenomena at scales less than one day were excluded from consideration and treated as noise by the assimilation algorithm with 12-hour cycle. The Monterey Bay is known for its complicated dynamics (Rosenfeld *et al*., 1994; Shulman *et al*., 2002; Ramp *et al*., 2005) on time scales of 1-2 days and less, and it is interesting to explore the impact of time resolution on the overall skill of the assimilation system. Therefore, the intended assimilation interval is shortened to 1 hour in the present study. However, shortening the assimilation window raises another issue. The ensemble of model states used to define the flow-dependent BEC in the original scheme is obtained from the integration of the NCOM model and the respective forecasts and analyses. Shortening the assimilation window means increasing the time steps of the integration, which produces a larger ensemble size. In other words, an hourly data assimilation interval will increase the ensemble size substantially and will increase the computational cost at least 12 times compared with the original experiments.

Inspired by the “central moving average” technique (Chou, 1970, p. 38), a “floating

temporal window" (FTW) is added to the scheme when the ensemble is used to model the flow-dependent part of the BEC. The idea of FTW is to introduce a temporal radius whose magnitude is small enough to keep the scheme computationally efficient and large enough to retain the flow-dependent information and keep the assimilation skill of the system. When the ensemble is used for statistical analysis, only the ensemble members within this radius (71 hours or about 3 days in the present study) are chosen. In our case, the total ensemble size is 718, and the assimilation interval is 1 hour (i.e., 718 hours of glider data are assimilated). A temporal radius of 35 is chosen, so that the FTW covering 71 members is effective for generating the orthogonal basis of $\mathcal{R}^n$. When the assimilation moment is less than the temporal radius, however, the FTW is fixed from the first to the 71st of the ensemble members. Similarly, the FTW is also fixed towards the end of assimilation cycles.

The cost of updating the covariance estimates grows substantially with the ensemble dimension. By applying the FTW, the size of the ensemble is reduced to a reasonable level without losing the major flow-dependent background information while improving the computational efficiency significantly. With a FTW ensemble size of 71 members (about 3 days with hourly analyses), the computational cost for the scheme is less than 5% of the one using the full ensemble (with 718 members).

### 3.4 Dynamical Constraints

The model forecasts are in dynamical balance, which is achieved by the NCOM model's self-adjustment during the model integration. The new analyses from data assimilation are obtained by adding the assimilation increments $\boldsymbol{\delta x}$ to the model forecasts $\boldsymbol{x}^f$. The increments $\boldsymbol{\delta x}$, however, are not guaranteed to be in dynamical

balance. Specifically, the temperature and salinity increments obtained from glider data assimilation might change the density of the water column and thus break the dynamical consistency. To solve this problem, two dynamical constraints, hydrostatic balance and geostrophic balance (e.g., Li *et al*., 2008), are incorporated into the hybrid data assimilation scheme.

The two dynamical balances can be expressed by the following equations (Li *et al*., 2008):

Hydrostatic balance: $$\frac{\partial \delta p}{\partial z} = -g\delta\rho \tag{3.4.1}$$

Geostrophic balance: $$\mathbf{\Omega}\times\delta\boldsymbol{v} = -\rho^{-1}\nabla\delta p \tag{3.4.2}$$

where $p$ denotes pressure; $\rho$ represents density; $\mathbf{\Omega}$ stands for angular velocity of earth's rotation; $\boldsymbol{v}$ is the horizontal velocity vector.

The two dynamical constraints are applied to the assimilation increments (temperature and salinity). The coordinate system in our hybrid system is pure sigma layers; thus, the geostrophic balance relationship is difficult to apply to the increments directly. In particular, the depths of the same layer are typically different at different locations. The depth difference of the same sigma layer at two locations could reach hundreds of meters. Hence, in order to apply the geostrophic balance, the density derived from temperature and salinity increments is linearly interpolated into Cartesian coordinates. The application of geostrophic balance and hydrostatic balance is thus accomplished in Cartesian coordinates. The adjusted increments are then interpolated back to respective sigma layers and added to the model forecasts.

## 3.5 Numerical Model

The numerical model used in this study is Navy Coastal Ocean Model (NCOM),

which is a three dimensional oceanic model with hydrostatic and Boussinesq approximations (Martin, 2000; Rhodes *et al*., 2002). NCOM is based on the Princeton Ocean Model (POM) and Sigma/Z-level Model (SZM). Thus, NCOM is a primitive equation based model with options of using pure z-coordinate, or pure sigma layer, or hybrid layers with sigma coordinates in the upper layers and z coordinates in the lower layers (Shulman *et al*., 2007; Yaremchuk *et al*., 2011). A pure sigma coordinate scheme with 29 levels is adopted in the present study.

*a. NCOM Equations*

The differential equations of NCOM and physical meaning of each term are listed below:

**x-component momentum equation:**

$$\frac{\partial u}{\partial t} = -\nabla \cdot (\vec{v}u) + fv - \frac{1}{\rho_0}\frac{\partial p}{\partial x} + F_u + \frac{\partial}{\partial z}(K_M \frac{\partial u}{\partial z}) \tag{3.5.1}$$

$\frac{\partial u}{\partial t}$: local acceleration;

$\nabla \cdot (\vec{v}u)$: divergence of advective momentum fluxes;

$fv$: coriolis acceleration;

$-\frac{1}{\rho_0}\frac{\partial p}{\partial x}$: x-direction pressure gradient force;

$F_u$: x-direction horizontal mixing term for momentum;

$\frac{\partial}{\partial z}(K_M \frac{\partial u}{\partial z})$: x-direction momentum eddy diffusion term caused by vertical mixing;

**y-component momentum equation**:

$$\frac{\partial v}{\partial t} = -\nabla \cdot (\vec{v}v) - fu - \frac{1}{\rho_0}\frac{\partial p}{\partial y} + F_v + \frac{\partial}{\partial z}(K_M \frac{\partial v}{\partial z}) \tag{3.5.2}$$

$\frac{\partial v}{\partial t}$: local acceleration;

$\nabla \cdot (\vec{v}v)$: divergence of advective momentum fluxes;

$fu$: Coriolis acceleration;

$-\frac{1}{\rho_0}\frac{\partial p}{\partial y}$: y-direction pressure gradient force;

$F_v$: y-direction horizontal mixing term for momentum;

$\frac{\partial}{\partial z}(K_M \frac{\partial v}{\partial z})$: y-direction momentum eddy diffusion term caused by vertical mixing;

**z-component momentum equation:** Under Boussinesq and Hydrostatic approximation, the z-component momentum equation can be written as:

$$\frac{\partial p}{\partial z} = -\rho g \tag{3.5.3}$$

$\frac{\partial p}{\partial z}$: vertical pressure gradient force;

$-\rho g$: gravity force;

**Continuity equation:**

$$\frac{\partial u}{\partial x} + \frac{\partial v}{\partial y} + \frac{\partial w}{\partial z} = 0 \tag{3.5.4}$$

$\frac{\partial u}{\partial x} + \frac{\partial v}{\partial y} + \frac{\partial w}{\partial z}$: divergence of velocity;

**Heat equation:**

$$\frac{\partial T}{\partial t} = -\nabla \cdot (\vec{v}T) + \nabla_h (A_H \nabla_h T) + \frac{\partial}{\partial z}(K_H \frac{\partial T}{\partial z}) + Q_r \frac{\partial \gamma}{\partial z} \tag{3.5.5}$$

$\frac{\partial T}{\partial t}$: local rate of change of temperature with respect to time;

$\nabla \cdot (\vec{v}T)$ : advective heat fluxes;

$\nabla_h (A_H \nabla_h T)$ : eddy diffusion of heat due to horizontal mixing;

$\frac{\partial}{\partial z}(K_H \frac{\partial T}{\partial z})$ : eddy diffusion of heat due to vertical mixing;

$Q_r \frac{\partial \gamma}{\partial z}$ : solar radiation term;

**Salt equation:**

$$\frac{\partial S}{\partial t} = -\nabla \cdot (\vec{v}S) + \nabla_h (A_H \nabla_h S) + \frac{\partial}{\partial z}(K_H \frac{\partial S}{\partial z}) \tag{3.5.6}$$

$\frac{\partial S}{\partial t}$ : local rate of change of salinity with respect to time;

$\nabla \cdot (\vec{v}S)$ : advective salt fluxes;

$\nabla_h (A_H \nabla_h S)$ : eddy diffusion of salt due to horizontal mixing;

$\frac{\partial}{\partial z}(K_H \frac{\partial S}{\partial z})$ : eddy diffusion of salt due to vertical mixing;

**Equation of state:**

$$\rho = \rho(T, S, p) \tag{3.5.7}$$

In the above equations, t denotes time; $x$, $y$ and $z$ are the three Cartesian coordinates; $u$, $v$ and $w$ are the three velocity components; $\vec{v}$ is velocity vector; $T$ and $S$ are potential temperature and salinity, respectively; $\nabla$ is gradient operator and $\nabla_h$ is the horizontal gradient operator; $f$ is the Coriolis parameter; $p$ and $\rho$ denote pressure and density, respectively; $\rho_0$ represents reference water density; $g$ is gravitational acceleration; $F_u$ and $F_v$ are horizontal mixing terms for momentum; $A_H$ represents the horizontal mixing coefficient for temperature and salinity scalar fields; $K_M$ and $K_H$

denote vertical eddy diffusion coefficients for momentum and scalar fields, respectively; $Q_r$ represents solar radiation, and $\gamma$ is a function describing the solar decay.

*b. NCOM Setting for Present Study*

**Surface and bottom boundary conditions:**

Surface: $K_M \frac{\partial u}{\partial z} = \frac{\tau_x}{\rho_0}$ , $K_M \frac{\partial v}{\partial z} = \frac{\tau_y}{\rho_0}$

$$K_H \frac{\partial T}{\partial z} = \frac{Q_b + Q_e + Q_s}{\rho_0 c_p} \text{ and } K_H \frac{\partial S}{\partial z} = S\Big|_{z=\zeta}(E_v - P_r)$$

where $\tau_x$ and $\tau_y$ are x and y direction surface wind stress. $Q_b$, $Q_e$ and $Q_s$ denotes the net long wave, latent and sensible surface heat fluxes. $c_p$ is specific heat capacity of seawater. $E_v$ and $P_r$ are surface evaporation and precipitation rates. $\tau_x$, $\tau_y$, $Q_b$, $Q_e$, $Q_s$, $E_v$ and $P_r$ are prescribed in atmospheric input files from Navy's Coupled Ocean and Atmospheric Mesoscale Prediction System (COAMPS), which was developed by Marine Meteorology Division of the NRL at Monterey, California (Hodur, 1997).

Bottom: $K_M \frac{\partial u}{\partial z} = c_b u|\vec{v}|$ $K_M \frac{\partial v}{\partial z} = c_b v|\vec{v}|$

$K_H \frac{\partial T}{\partial z} = 0$ $K_H \frac{\partial S}{\partial z} = 0$

The bottom drag coefficient $c_b$ is:

$$c_b = \max\left[\frac{\kappa^2}{\ln^2(\frac{\Delta z_b}{2z_0})}, c_{b_{\min}}\right],$$

where von Karman's constant $\kappa = 0.4$. $\Delta z_b$ is the thickness of the layer that is the closest

to the bottom. $z_0$ is the bottom roughness. $c_{b_{\min}} = 0.0025$ is the minimum value of $c_b$.

**Open boundary conditions:**

NCOM is set up to be one-way coupled with a global NCOM model at open boundaries (Shulman *et al*., 2009). Cross-shelf open boundaries are near-orthogonal to the isobaths (Figure 5), which accommodates local bathymetry and allows flow to be almost normal to the open boundaries (Shulman *et al*., 2002).

(a) Depth-averaged normal velocity: Flather open boundary condition:

$$v_f^{normal} = v_c^{normal} - \sqrt{\frac{g}{H}}(\zeta_C - \zeta_f)$$

where $v_f^{normal}$ is the depth averaged normal velocity of regional NCOM (with fine grid). $v_c^{normal}$ is the depth averaged normal velocity of global NCOM (with coarse grid). H is the depth of the bottom. $\zeta_C$ is the sea surface elevation from global NCOM. $\zeta_f$ is the sea surface elevation of regional NCOM.

(b) Depth-averaged tangential velocity: Orlanski radiation condition for outward propagating signals and relax to externally specified values for incoming signals.

(c) Normal baroclinic velocity: Orlanski radiation condition for outgoing signals and relax to externally specified values for incoming signals.

(d) Tangential baroclinic velocity: Orlanski radiation condition for outgoing signals and relax to externally specified values for incoming signals.

(e) Scalar fields (T and S): Orlanski radiation condition for outgoing signals and relax to externally specified values for incoming signals.

**River inflow for source terms:** river inflow off (no river input in present study, i.e., all source terms equal to 0).

**Horizontal mixing:** Smagorinsky scheme.

**Vertical mixing:** Mellor and Yamada Level 2.5 scheme.

**Leapfrog timestep:** 450 s.

**Model output frequency:** 1 hourly.

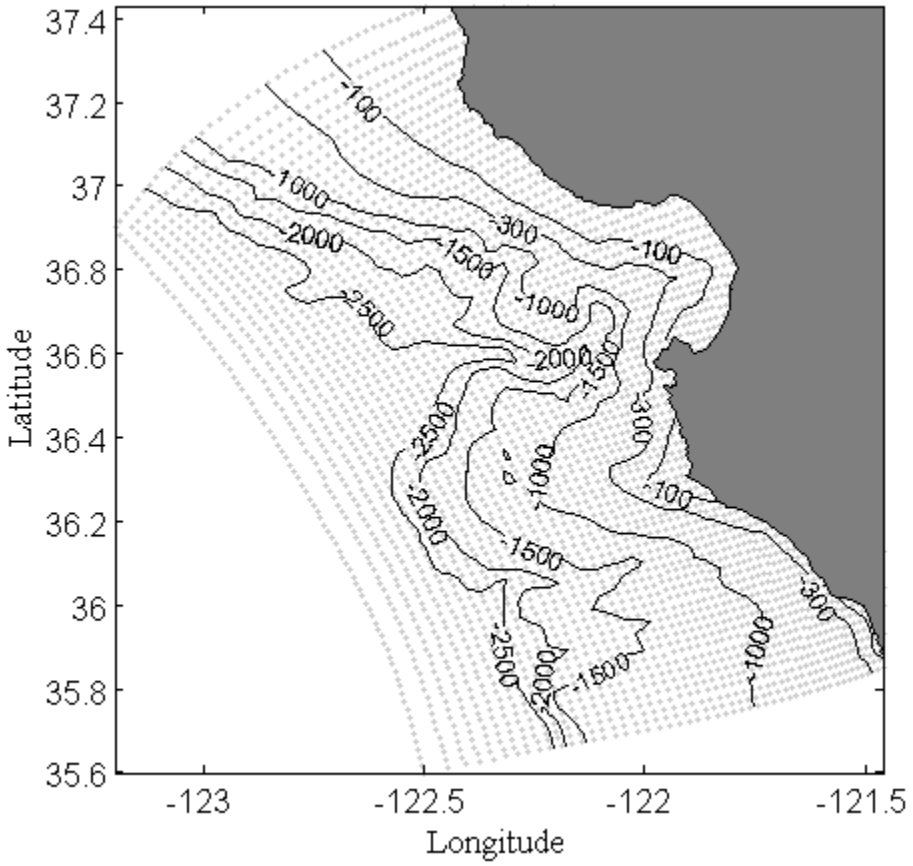


Figure 5. NCOM model grid (gray points) and bottom topography.

**Horizontal grid:** The model runs on an orthogonal curvilinear grid, which adapts to local complex geometry and has horizontally variable resolution (1-4 km) (Figure 5). The horizontal dimensions of grid-cells ( $\Delta x$ , $\Delta y$ ) vary spatially and are stored in two dimensional arrays (58 by 81). To convert Cartesian equations to finite difference form, the fluxes between grid cells and the exchange between u and v momentum are adjusted to adapt to the changing size of grid cells (Martin, 2000). Similar to POM, the Arakawa C grid is used for the horizontal arrangement of variables of NCOM (Figure 6a).

Specifically, the scalar variables (temperature and salinity) are located at the center of a cell while velocity components (u and v) are located at the center of the grid-cell face.

**Vertical grid:** Sigma coordinate with 29 sigma levels. Vertical grid arrangement for variables is showed in Figure 6b.

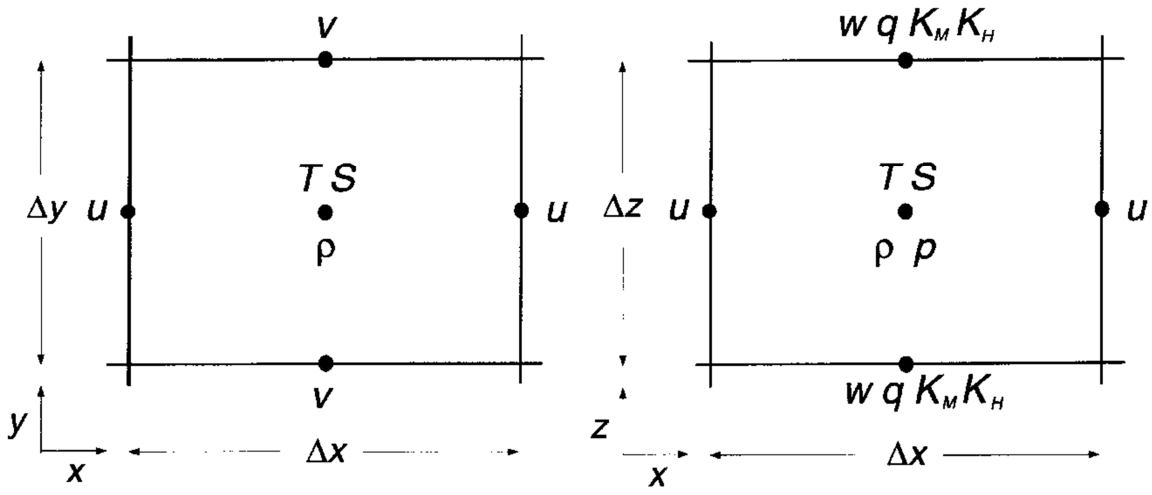


Figure 6. a. Arakawa C grid; b. Vertical grid (Martin, 2000).

*c. NCOM Schemes*

**Spatial differencing:** similar to POM, NCOM uses centered finite differencing for spatial differencing. For example:

$$\frac{\partial \phi}{\partial x} = \frac{\phi_{x+\Delta x/2} - \phi_{x-\Delta x/2}}{\Delta x}$$

where $\phi$ could be temperature, salinity, velocity and surface elevation.

**Temporal differencing:** similar to POM, NCOM uses leapfrog scheme for temporal differencing. Most of the terms are centered in time at n. Horizontal diffusion terms are taken from n-1 time level because a variable being diffused taken from central time level n in leap frog scheme is numerically unstable. The vertical diffusion terms are treated implicitly (with n+1 time level) to avoid time-step restriction for explicit scheme (a small time step is required to maintain stability for the explicit scheme, but the time-step of

NCOM is large when calculating diffusion).

To suppress time splitting problem for the leapfrog scheme, Asselin filter is applied to n time levels:

$$\phi_f^n = \phi^n + \nu(\phi^{n+1} - 2\phi^n + \phi^{n-1})$$

where $\nu$ denotes filter coefficient with typical value of 0.05.

**Horizontal mixing:** NCOM provides the option of using Smagorinsky scheme or grid cell Reynolds number scheme for horizontal mixing. In present study, the Smagorinsky scheme is adopted for horizontal mixing in NCOM.

Smagorinsky scheme:

Smagorinsky scheme has the following horizontal friction terms for momentum:

$$F_u = \frac{\partial}{\partial x}\left(2A_M \frac{\partial u}{\partial x}\right) + \frac{\partial}{\partial y}\left(A_M\left(\frac{\partial u}{\partial y} + \frac{\partial v}{\partial x}\right)\right)$$

$$F_v = \frac{\partial}{\partial y}\left(2A_M \frac{\partial v}{\partial y}\right) + \frac{\partial}{\partial x}\left(A_M\left(\frac{\partial u}{\partial y} + \frac{\partial v}{\partial x}\right)\right)$$

where $A_M$ takes the form:

$$A_M = C_{smag}\Delta x \Delta y\left(\left(\frac{\partial u}{\partial x}\right)^2 + \frac{1}{2}\left(\frac{\partial v}{\partial x} + \frac{\partial u}{\partial y}\right)^2 + \left(\frac{\partial v}{\partial y}\right)^2\right)^{1/2}$$

The constant $C_{smag}$ ranges from 0.02 to 0.5. A typical value for $C_{smag}$ is 0.1, which is used in the model set up in this study.

**Vertical Mixing:** NCOM provides the option of using Meller & Yamada Level 2.5 (MYL 2.5) or Meller & Yamada Level 2 (MYL) for vertical mixing. MYL 2.5 scheme is adopted in this study.

Meller and Yamada Level 2.5:

MYL 2.5 provides an equation to calculate turbulence kinetic energy (TKE) $q^2/2$. Another equation for estimation of vertical turbulence length scale $l$ is also provided. The vertical eddy coefficients $K_M$ and $K_H$ has the form:

$$K_M = qlS_M(G_H)$$

$$K_H = qlS_H(G_H)$$

$S_M$ and $S_H$ are functions of Richardson number ($G_H$). The equations of $S_M$ and $S_H$ involves several non-dimensional constants $a_1$, $a_2$, $b_1$, $b_2$, $c_1$. Nondimensional constants $a_1$, $a_2$, $b_1$, $b_2$, $c_1$ take the values of 0.92, 16.6, 0.74, 10.1 and 0.08, respectively. These values were obtained from laboratory experiments. Richardson number $G_H = l^2(-N^2)/q^2$ ($N^2$ is the buoyancy frequency).

In the prognostic equation of $q^2 l$, Mellor and Yamada (1982) introduced a "wall proximity" function to increase the dissipation near the surface and bottom:

$$W = 1 + E_2\left(\frac{l}{\kappa L}\right)^2$$

where

$$L^{-1} = (\zeta - z + z_s)^{-1} + (z - H + z_0)^{-1}$$

Non-dimensional constant $E_2$ has value of 1.33. $\zeta$ is the surface elevation. $\kappa$ is the Von Karman constant with a value of 0.4. The expression of $L^{-1}$ is modified from POM to account for surface roughness length $z_s$ and bottom roughness length $z_0$ (Martin, 2000). $z_s$ and $z_0$ usually have small values; thus, this modification is not significant in most cases, but the surface roughness can cause significant mixing in the surface mixed layer when there are strong winds and breaking waves.

Turbulent kinetic energy boundary conditions:

$$\text{Surface:} \qquad q^2 = b_1^{\frac{2}{3}} \left( \frac{\tau}{\rho_0} \right)$$

$$\text{Bottom:} \qquad q^2 = b_1^{\frac{2}{3}} \left( u^2 + v^2 \right)^{1/2}$$

where $\tau$ denotes wind stress.

**Free-Surface Mode:** the Princeton Ocean Model (POM) uses an explicit time-splitting scheme to calculate the free surface, while NCOM uses an implicit scheme. Therefore, the pressure gradient in the right hand side of the vertically averaged momentum equation, and the divergence terms in the right hand side of the vertically integrated continuity equation have a component from the n+1 time level. This implicit scheme is much simpler than the split-explicit scheme used in POM. The implicit scheme has a larger time step; thus, it is not as accurate in simulating propagation of surface gravity waves as the POM scheme. However, the implicit scheme is sufficiently to accurately simulate physical features with large time-scales (Martin, 2000). Steps to calculate free-surface mode: (a) Before the free-surface mode can be calculated, the 3D horizontal velocities have to be calculated and the forcing terms from the 3D momentum equations are vertically integrated to provide forcing terms for the free-surface mode, and (b) the depth-averaged momentum and continuity equations are solved for the new surface elevation. An iterative solver is used to calculate the new surface elevation.

**Bottom Drag:** NCOM uses partially implicit scheme to calculate bottom drag.

$$K_M \frac{\partial u}{\partial z} = c_b u^{n+1} \left| \vec{v}^{n-1} \right|$$

$$K_M \frac{\partial v}{\partial z} = c_b v^{n+1} \left| \vec{v}^{n-1} \right|$$

The explicit part of the bottom drag is taken from time level n-1, so that it does not cause time splitting.

*d. NCOM Disadvantages*

Although NCOM has been used in many oceanic research and applications, it has been recognized to have certain limitations. First, because NCOM uses hydrostatic approximation, non-hydrostatic phenomena, such as propagation of internal waves or propagation of freshwater plumes, may not be able to be described accurately (Martin, 2000). The results may not be good for certain processes in which vertical accelerations and small scale phenomena are important. Since our investigation is limited to the Monterey Bay and surrounding area, which both have relatively large horizontal scales, NCOM should be capable of producing confident results (Martin, 2000). Second, the sigma vertical coordinates used in NCOM might result in large truncation errors for the mixing terms when dealing with steep slopes, such as the large gradient of MSC bathymetry. To solve this problem, the bathymetry has been properly smoothed to be compatible with the horizontal model grid resolution (1-4 km). Given that our study is concentrated at the upper level of the ocean (generally less than 500 m), the truncation error resulting from sigma coordinate in steep topography region should be reasonably small. Third, the implicit treatment of the free surface used in NCOM is not as accurate as the explicit time-splitting scheme used by POM, especially for surface wave propagation. Fourth, the second-order centered advection scheme suffers from advective overshoots at sharp fronts. Fifth, a signal (wave or diffusion of a field) cannot travel more than a single grid interval in a single time step (time step limitation). Sixth, if the surface elevation reaches the bottom of a grid cell or the bottom of the sigma coordinate grid,

NCOM will stop (drying of grid cells). The minimum depth of the model grid cells must be set deeper than the minimum depth of the free surface (this involves guessing).

### 3.6 Observations

During the second Autonomous Ocean Sampling Network (AOSN-II) experiment (late July – early September 2003), five Spray gliders (Sherman *et al*., 2001) and 10 Slocum gliders (Webb *et al*., 2002) were deployed in the Monterey Bay region, collecting temperature and salinity profiles (Ramp *et al*., 2008). The 10 Slocum gliders typically measure the temperature and salinity of the upper 200 m and were deployed near shore (approximately from 2 km to 30 km offshore). The five Spray gliders are capable of collecting vertical profiles down to 400 m (and occasionally 700 m) and covered longer distances from the shore (up to about 100 km offshore) (Ramp *et al*., 2008). Since NCOM model grids cover less horizontal distance (less than 100 km) offshore, some of the Slocum glider data outside of our study area aren't used. Glider profile locations are shown in Figure 7. Given that the horizontal diving distance of a glider (about 0.5 km) is much smaller than the grid resolution (1-4 km), all temperature and salinity profiles are treated as vertical profiles (Yaremchuk *et al*., 2011).

All raw glider profiles are subjected to data quality control before being utilized in data assimilation. The data quality control includes three steps. The first step is to get rid of outliers and unrealistic temperature and salinity. A 2-D histogram is designed for this step. The water column from surface down to 750 m is separated into 31 layers. For every layer, a 2-D histogram is generated (example: Figure 8). Outliers and unrealistic data points are excluded according to the histogram. The original number of glider data points of all layers is 42872842, and this number is reduced to 42708987. The cut off percentage

for all layers is about 0.53% (Figure 9). Second, a stability test (density should increase with depth) are performed on each profile. The density is calculated from the temperature and salinity using the proper equation of state. The data points that failed this test are removed from the data set. Third, all the data that passed the first and second steps are linearly interpolated into the grid points of the NCOM model for further utilization.

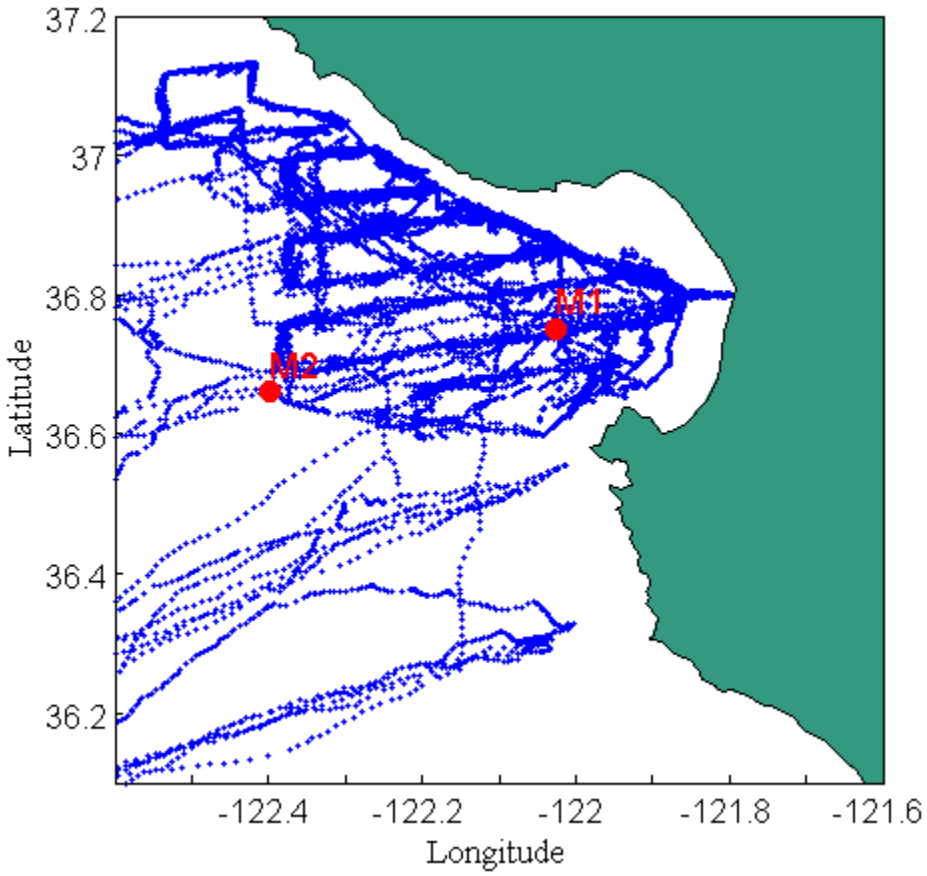


Figure 7. Locations of glider profiles near Monterey Bay during AOSN-II experiment (gray dots). The two black dots are locations of independent moorings M1 and M2.

Two independent mooring points M1 and M2 (Figure 7) were set up by Monterey Bay Aquarium Research Institute (MBARI), recording vertical temperature, salinity and current velocity (Ramp *et al.*, 2005). The mooring observations are used to verify real data experiment results and are not directly involved in the data assimilation.

Figure 10 presents distribution of the number of glider data over the considered time

period and depth.

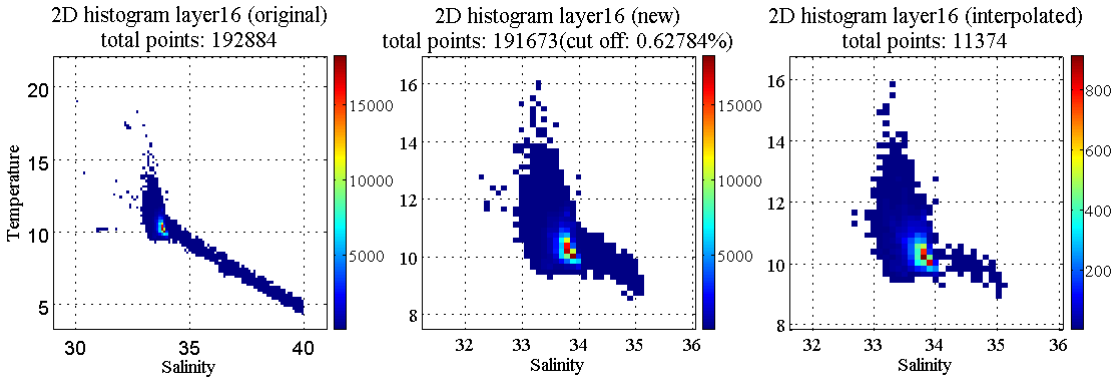


Figure 8. 2D histogram for layer 16 (54 - 65 m) before quality control step 1 (a) and after quality control step 2 (b).

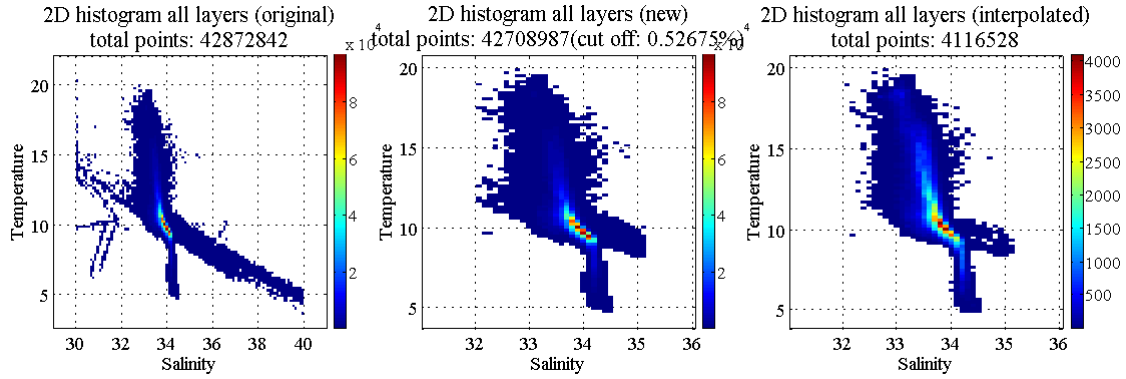


Figure 9. 2D histogram for all layers before quality control step 1 (a) and after quality control step 1 (b).

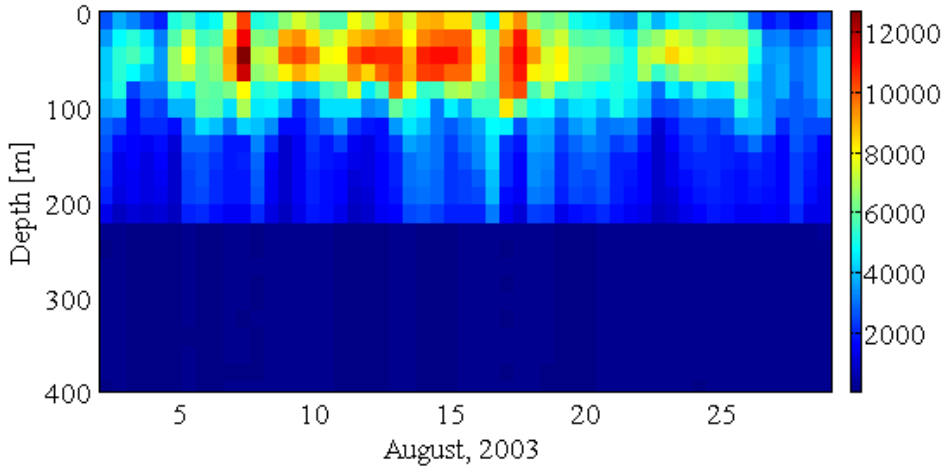


Figure 10. Distribution of the number of glider data over the considered time period and depth.

## 3.7 Distance between States (Yaremchuk et al., 2011)

To estimate the numerical distance between two states, a diagonal matrix $\boldsymbol{g}$ is defined as follows: the diagonal elements of $\boldsymbol{g}$, i.e. $g_T, g_S, g_u, g_v, g_\zeta$, are horizontally averaged time variances (depth-dependent) of temperature, salinity, velocity u, v and SSH $\zeta$, respectively. At a grid point r, the diagonal elements can be represented as:

$$g_\xi(z) = \left\langle \overline{[\xi(r) - \overline{\xi(r)}]^2}^{1/2} \right\rangle_z \tag{3.7.1}$$

where $\xi$ stands for either T, S, u, v or $\zeta$. The angular brackets denote horizontal average at level z.

The distance between two states can be estimated in both observational and state spaces:

$$r_\xi^g(\boldsymbol{x}_1, \boldsymbol{x}_2) = \left\langle (\xi_1 - \xi_2)^2 R_\xi^{-2} \right\rangle_g^{1/2} \text{ (observational space)} \tag{3.7.2}$$

$$r_\xi^S(\boldsymbol{x}_1, \boldsymbol{x}_2) = \left\langle (\xi_1 - \xi_2)^2 g_\xi^{-1} \right\rangle^{1/2} \text{ (state space)} \tag{3.7.3}$$

The angular brackets above stand for averaging over glider locations $r_k^g$ and over the 3D model domain covered by gliders, respectively.

# CHAPTER IV

# EXPERIMENT DESIGN

A key step in developing the hybrid 3D-VAR system is successfully assimilating oceanic data into existing ocean models. Hence, all the experiments here are designed to verify if this 3D-VAR system has the capability of assimilating glider temperature and salinity observations into NCOM. As mentioned before, a 12-hourly data assimilation interval was applied in the original 3D-VAR experiments (Yaremchuk *et al*., 2011). Although the original assimilation scheme is still applicable for temporally intensive data assimilation, the computational cost is too high for this scheme to be used in practical application. To solve this problem, the FTW window is added to the scheme (see section 3.3). Another issue of the original 3D-VAR experiments (Yaremchuk *et al*., 2011) is that about 90% of the glider data were excluded from the assimilation because of the 12-hour assimilation interval. An hourly data assimilation interval is, thus, applied in all of the following experiments in order to make use of all the glider observations.

## 4.1 Twin Data Experiments

Before real data is used in assimilation, a series of twin data experiments are performed because the "true state" can be produced by a model free run in twin data experiments while a "true state" does not exist in real data experiments. The procedure of twin data experiments is described below:

Step 1: the generation of a "true state." A NCOM model free run is performed and used as the "true state" in twin data experiments. The free run is initiated from 0:00 August 02 and ends at 15:00 August 31 (712 hours in total). The output interval of NCOM is set to be 1 hour in order to match the data assimilation interval.

Step 2: the generation of "bogus glider data." The real glider data are not used in the twin data experiments. Instead, bogus glider data are generated from the "true state." Specifically, every glider observation value is replaced by corresponding "true state" value plus a small perturbation. The perturbation is created by multiplying a random number (with 0 mean and 0.3 rms variation) with the variance of the true glider data at the corresponding depth. The reason for this step is described as follows. In the assimilation step (step 4), these bogus glider data are assimilated into NCOM. Since the bogus glider data are generated from the "true state," the results of assimilation can be compared with the "true state." If the assimilation results are close to the "true state," the assimilation is successful. The "true state" model state represents the true state of the ocean, which cannot be measured in the real world. The bogus data represents observations in the real world, which can be measured, but with errors (perturbations in our case) with respect of the true value.

Step 3: the generation of a first guess. To initiate the assimilation run and estimate proper weighting of the hybrid BEC terms, the first guess model solution is generated by integrating NCOM for 712 hours starting from the initial condition specified by the fifth hour of the "true state." This step makes sure that the first guess doesn't differ too far from the "true state."

Step 4: "glider data" assimilation. (a) Using the first (t = 1) state of the first guess as the background field, the bogus glider data in the first hour are assimilated and the analyses are formed by adding the analysis increment to the first guess: $\boldsymbol{x}^a = \boldsymbol{x}^{fg} + \delta\boldsymbol{x}$ ($x^{fg}$ denotes first guess state vector); (b) New model forecasts are obtained by integrating NCOM for 1 hour using the analyses $\boldsymbol{x}^a$ as the initial condition; (c) The bogus glider

data in this hour are assimilated and new analyses are produced by updating the model forecasts with the analyses increment: $\boldsymbol{x}^a = \boldsymbol{x}^f + \boldsymbol{\delta x}$ ( $x^f$ represents NCOM forecasts state vector); and (d) Repeat steps (b) and (c) until t = 712.

Two runs are compared in twin data experiments. Run 1 is a 3D-VAR assimilation run using traditional BEC (static BEC only). Run 2 is another assimilation run using the hybrid BEC (see section 3.1). Both runs are initiated from 0:00 August 02 and terminates at 15:00 August 31 (712 hours in total). Table 1 summarizes all NCOM runs and respective characteristics.

Table 1. Description of ALL NCOM runs.

| Experiments | Run | Data Assimilation | $B_0$ | $B_m$ | FTW | Observations |
|---|---|---|---|---|---|---|
| Twin | 1 | Yes | Yes | No | Yes | Bogus |
| | 2 | Yes | Yes | Yes | Yes | Bogus |
| Real I | 3 | No | - | - | - | - |
| | 4 | Yes | Yes | No | Yes | Genuine |
| | 6 | Yes | Yes | Yes | Yes | Genuine |
| Real II | 5 | Yes | Yes | Yes | No | Genuine |
| | 6 | Yes | Yes | Yes | Yes | Genuine |

## 4.2 Real Data Experiments

Real data experiments are conducted to test the ability of the hybrid 3D-VAR system to assimilate glider observations. The differences between the real data experiments and the twin data experiments are: (a) The “true state” does not exist in the real data experiments while “true state” can be produced by a simple model free run in the twin data experiments; (b) instead of extracted bogus glider data from the “true state,” real glider observations are assimilated into NCOM in the real data experiments; and (c) instead of verifying assimilation results with “true state,” observations of two independent moorings (see section 3.6) are used in the verification process. The

procedure of real data experiments is described below.

Step 1: the generation of a first guess field. An NCOM model free run is performed and used as the first guess in the real data experiments. The free run is initiated from 0:00 August 02 and ends at 21:00 August 31 (718 hours in total). The output interval of NCOM is set to be 1 hour. A number of NCOM free runs are compared with historical numerical results and observations (see section 3.5). The free run that most objectively reflects the physical phenomena of this region is selected as the first guess field.

Step 2: glider data assimilation. (a) Using the first (t = 1) state of the first guess as the background field, the glider data within the first hour are assimilated and the analyses are formed by adding the analysis increment to the first guess: $\boldsymbol{x}^a = \boldsymbol{x}^{fg} + \delta\boldsymbol{x}$ ($x^{fg}$ denotes first guess state vector). The ensemble in this step is formed by the first guess states; (b) New model forecasts are obtained by integrating NCOM for 1 hour using the analyses $\boldsymbol{x}^a$ as the initial condition. The ensemble member at this time step is replaced by the new forecast; (c) The glider data within this hour are assimilated and new analyses are produced by updating the model forecasts with the analyses increment: $\boldsymbol{x}^a = \boldsymbol{x}^f + \delta\boldsymbol{x}$ ($x^f$ represents NCOM forecasts state vector); and (d) Repeat steps (b) and (c) until t = 718.

Four runs are compared in the real data experiments. Run 3 is a NCOM model free run with no data assimilation treatment. Run 4 is a 3D-VAR assimilation run with the traditional BEC scheme (static BEC only). Run 5 is a 3D-VAR assimilation run with the old hybrid scheme (no FTW or geostrophic adjustment added). Run 6 is another assimilation run with the adjusted hybrid scheme (FTW and geostrophic added). All assimilation runs are verified by real observations from the two independent moorings

M1 and M2 (Figure 7). Table 1 summarizes all NCOM runs and respective characteristics. All real data assimilation runs are initiated from 0:00 August 02 and terminate at 21:00 August 31 (718 hours in total).

# CHAPTER V

# RESULTS AND DISCUSSION

## 5.1 Twin Data Experiments

### *a. Comparison With The "True State" at 60 m*

Northwesterly winds cause pronounced upwelling events in the Monterey Bay area (Tracy, 1990; Tseng *et al*., 2005). According to Shulman *et al*. (2009), August 2-20 was an extended upwelling period. It was followed by a brief relaxation during the period August 20-23. Another upwelling period happened during August 23-31. Table 2 summarizes the characters of run 1 and run 2 and the results of a comparison between these two runs during upwelling and relaxation periods at 60m. Although the bogus temperature and salinity data from the M1 and M2 moorings are available on 11 levels ranging from 0 to 300 m (where the bogus data are located), only the results of the 60 m level are present here since the performance of both run 1 and run 2 is the most typical on this level. Comparisons of the model temperature and salinity fields with the "true state" over the entire water column will be presented in section b. The comparisons are made between the "true state" and one hour NCOM forecasts, initiated by the analysis made 1 hour prior to observations.

Table 2. Description of the NCOM assimilation runs and the comparison of temperature and salinity solution errors at 60 meters in twin data experiments.

| Run | Static BEC | Flow-dependent BEC | M1 August 23-27 temperature | | M1 August 23-27 salinity | | M2 August 22-31 temperature | | M2 August 22-31 salinity | |
|---|---|---|---|---|---|---|---|---|---|---|
| | | | Bias ($^{o}$C) | RMS ($^{o}$C) | Bias | RMS | Bias ($^{o}$C) | RMS ($^{o}$C) | Bias | RMS |
| 1 | Yes | No | 0.26 | 0.32 | -0.04 | 0.05 | 0.24 | 0.41 | -0.07 | 0.08 |
| 2 | Yes | Yes | 0.04 | 0.14 | 0.002 | 0.02 | 0.20 | 0.32 | -0.02 | 0.04 |

Results from both runs at 60m as well as the "true state" located at M1 are

presented in Figure 11. Because the bogus data are extracted from the "true state," the results of a successful assimilation run will match, or come close to, the "true state." Overall, the results of both run 1 and run 2 match the "true state" except for the time period of August 23-27. During this period, temperature was predicted well by run 1 (with only the static BEC) and is about 0.5°C higher than the "true state," while salinity is about 0.06 lower than the "true state." Run 2 (with hybrid BEC) successfully predicts both temperature and salinity variation during August 23-27. According to Table 1, the temperature bias is reduced from 0.26°C (run 1) to 0.04°C (run 2), and the root mean square error (RMS) is reduced from 0.32°C (run 1) to 0.14°C (run 2). During the same period, salinity bias is reduced from -0.04 (run 1) to 0.002 (run 2), and the respective RMS is reduced from 0.05 (run 1) to 0.02 (run 2).

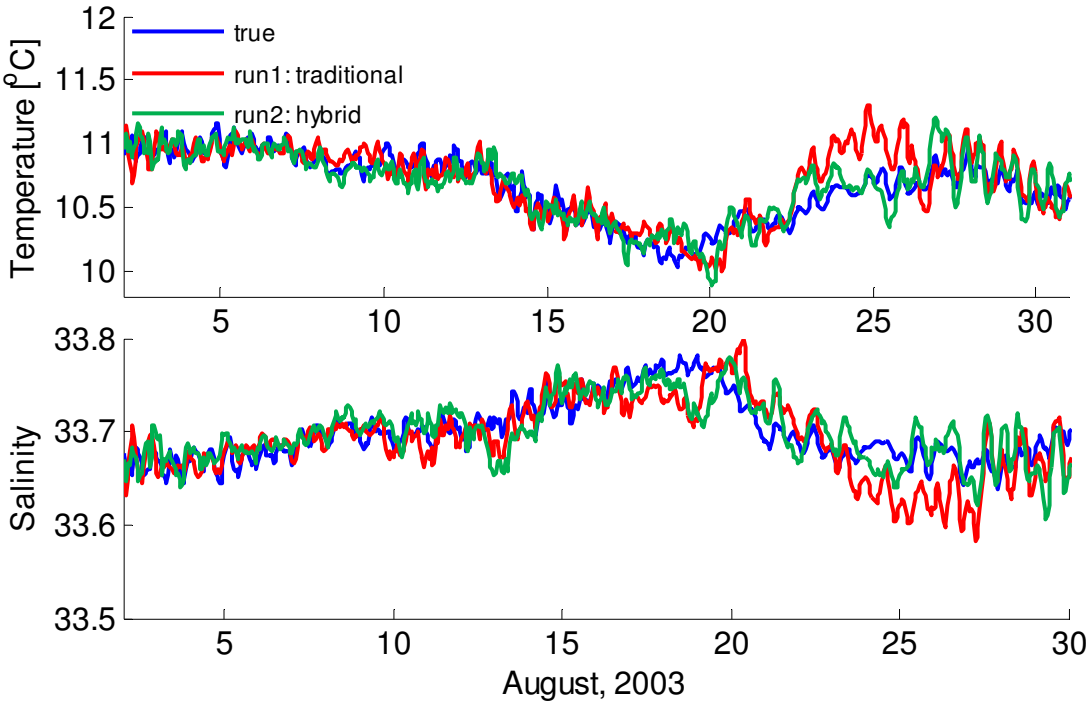


Figure 11. (a) Temperature comparisons between the results of run 1, run 2, and "true state" at M1 location at 60 m depth. (b) Salinity comparisons between the results of run 1, run 2, and "true" at the M1 location at 60 m depth.

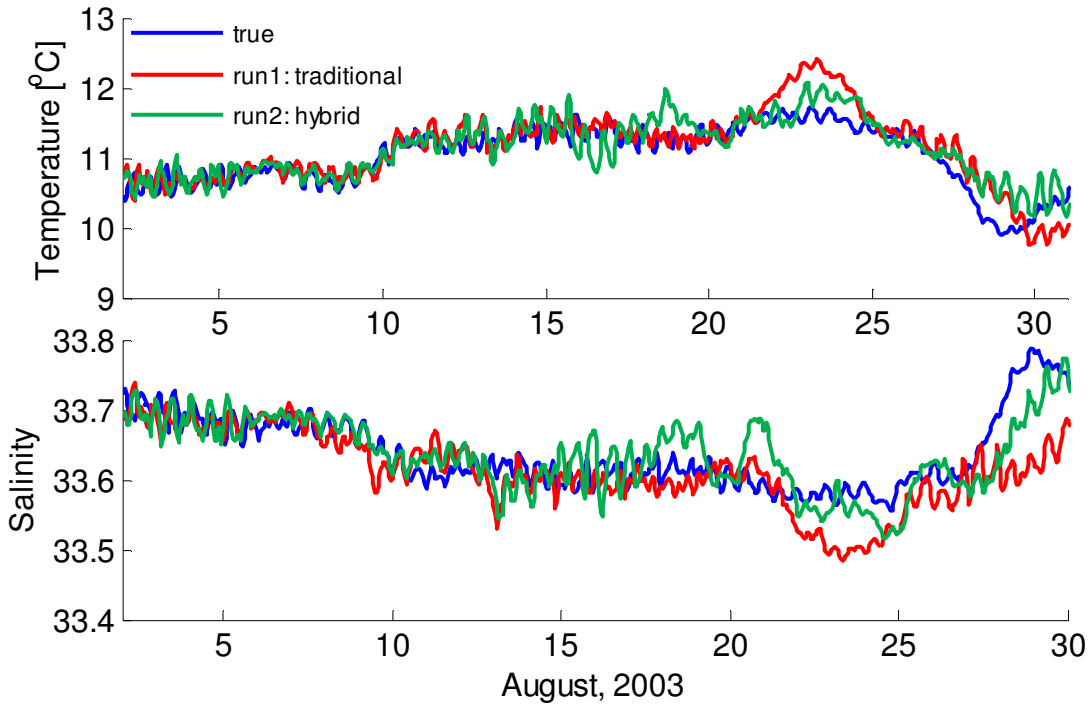


Figure 12. (a) Temperature comparisons between the results of run 1, run 2, and "true state" at M2 location at 60 m depth. (b) Salinity comparisons between the results of run 1, run 2, and "true state" at M2 mooring location at 60 m depth.

"True state" temperature and salinity at M2 mooring location are also used to evaluate model results (Figure 12). The dynamics at M2 is much more complicated than at M1 because of the onshore-offshore translation of Monterey Bay Eddy (MBE) during wind relaxation and upwelling events (Rosenfeld *et al*., 1994; Ramp *et al*., 2005; Shulman *et al*., 2009). Similar to Figure 11, run 1 results overestimate temperature by approximately 0.8°C (Figure 12) and underestimate salinity by about 0.1 during August 22-25. Run 2 salinity results are higher than those of the "true state" during the time periods August 18-19 and 20-22. According to Shulman *et al*. (2009), August 18-22 is a transition period of MBE moving on-shore. This could complicate the dynamics of this region and result in instability of the performance of assimilation schemes. Towards the end of the model runs (August 27-30), both run 1 and run 2 deviate from the "true state" temperature and salinity. Temperature results of both runs are about 0.5°C higher than the

"true state" temperature during this period (Figure 12a). Comparing with run 1, run 2 salinity results are in better agreement with the "true state" model state during August 27-31 (Figure 12b). During the last 9 days (August 22-31), the salinity bias is reduced from -0.07 to -0.02, and the respective RMS is reduced from 0.08 to half (Table 2).

*b. Comparison With "True State" throughout the Water Column*

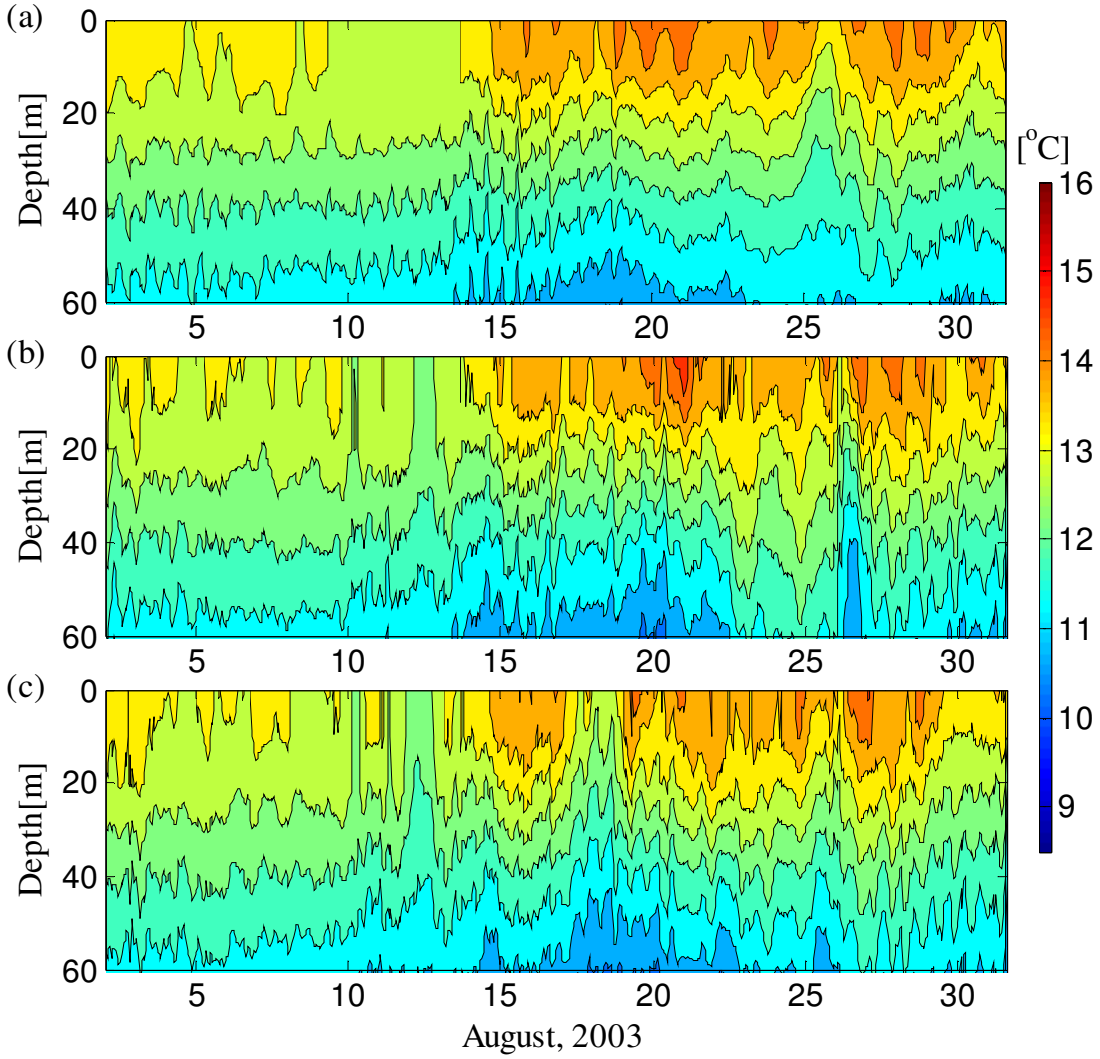


Figure 13. Temperature comparisons between model forecasts and the "true state" at M1 location from the surface down to 60 meters: (a) "true state"; (b) run 1; (c) run 2.

Comparisons of model temperature fields with the "true state" temperature at M1 location over the whole water column are presented in Figure 13. Overall, run 1 and run 2

are similar. Both assimilation runs are capable of predicting major spatial and temporal variations of the thermocline and vertical water column structure. Run 1, however, seems to overestimate surface temperature on August 21 (Figure 13b). In addition, temperature of the whole water column of run 1 appears to be colder than the "true state" temperature during August 26-27 (Figure 13b), while run 2 results for the same period are more consistent with the "true state" temperature (Figure 13c).

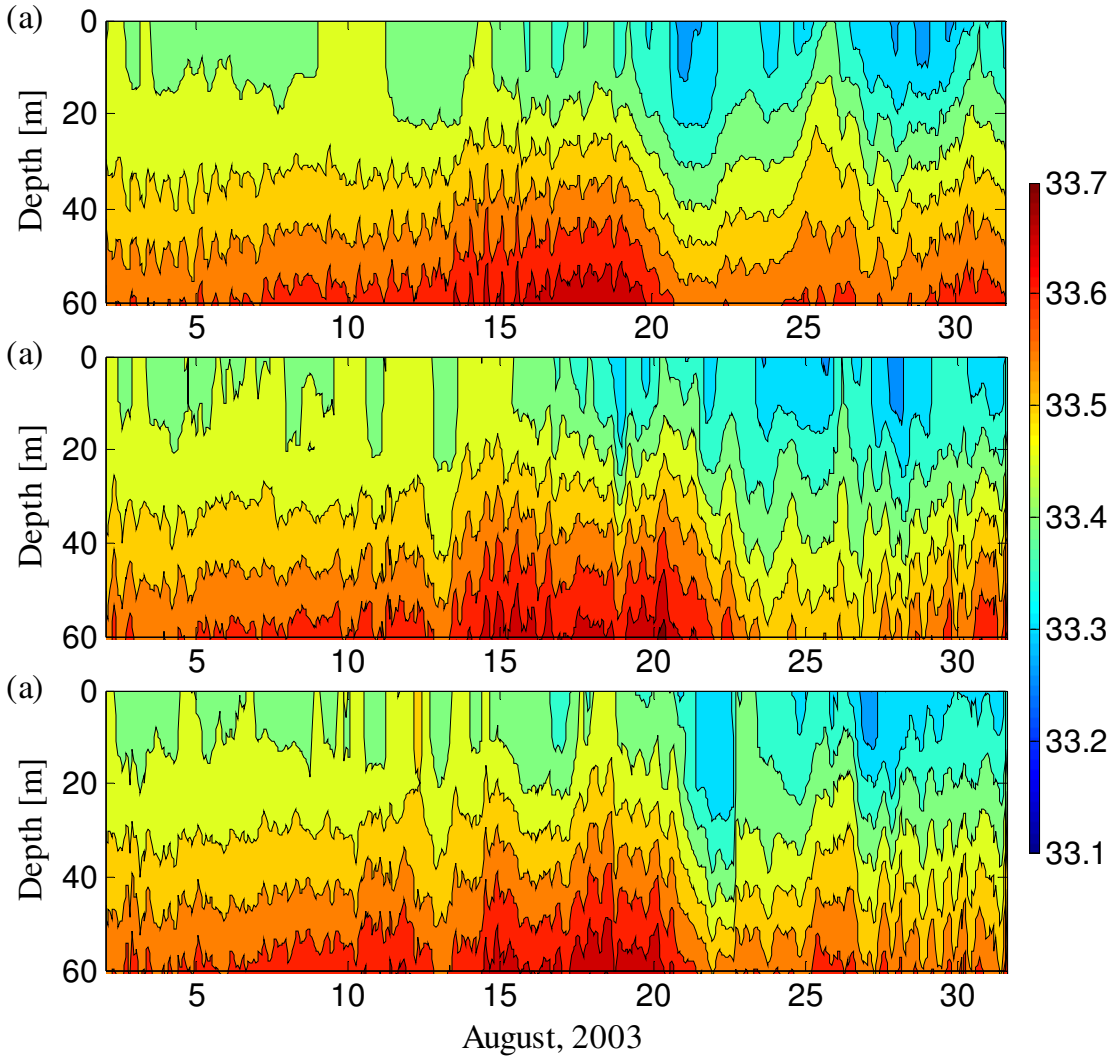


Figure 14. Salinity comparisons between model forecasts and "true state" at M1 mooring location from the surface down to 60 meters: (a) "true state"; (b) run 1; (c) run 2.

Vertical structure of salinity model solutions and "true state" at M1 mooring location are presented in Figure 14. Both assimilation runs (run 1 and run 2) are in good

agreement with the “true state” (Figure 14a), although both runs overestimate surface salinity during August 29-30. During the relaxation event (August 21-22), salinity in the upper layer (0-30 m) for run 1 is overestimated. In the results of run 2 during the same period, the overestimation of salinity is alleviated but is still present at the surface (Figure 14c). Shallowing of the halocline can be observed during the period August 25-27 (Figure 14a). Run 2 is in better agreement with the “true state” than run 1 during this period (Figure 14b, c).

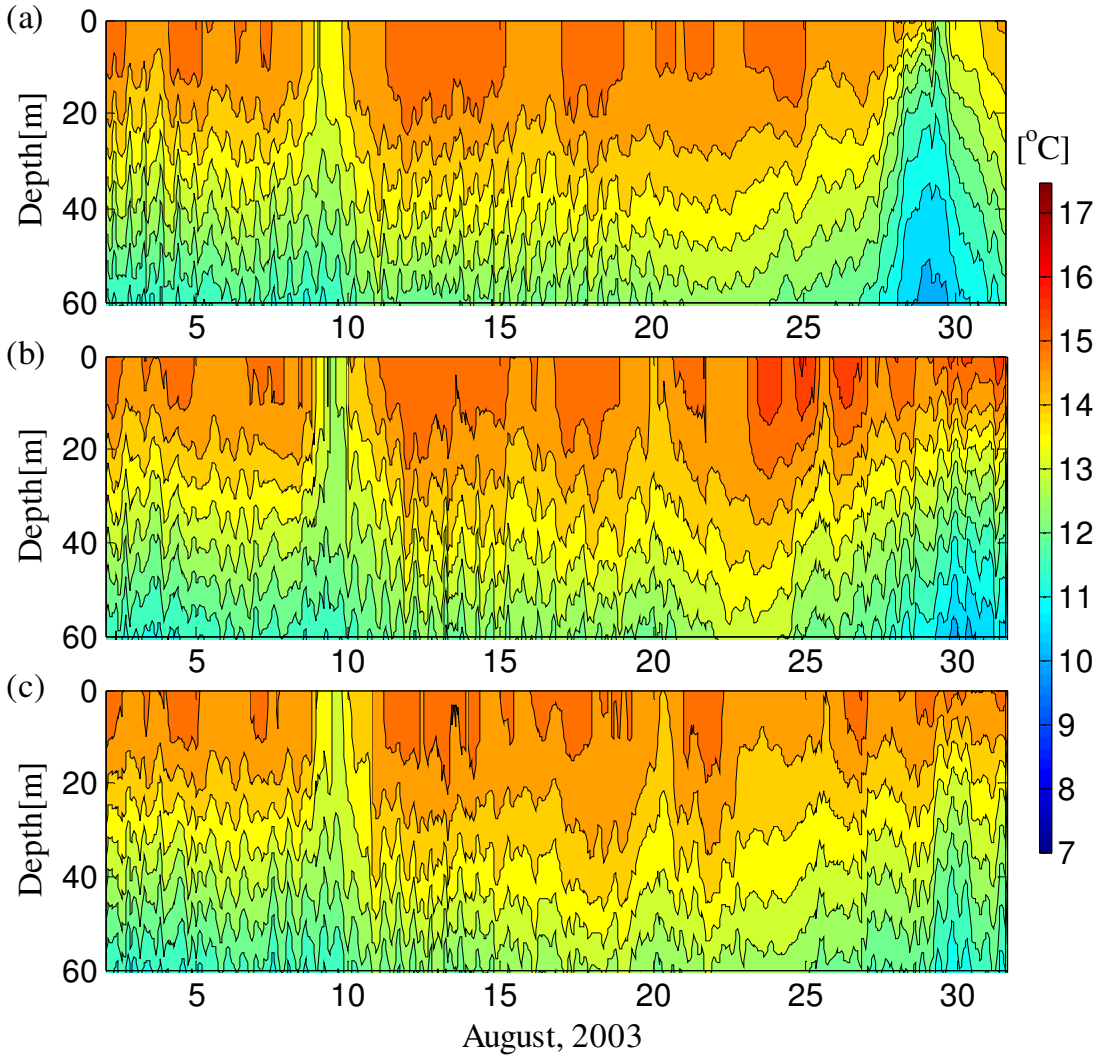


Figure 15. Temperature comparisons between model forecasts and “true state” at M2 mooring location from the surface down to 60 meters: (a) “true state”; (b) run 1; (c) run 2.

Figure 15 compares the vertical structure of model temperature with the “true state” at M2 mooring location. Although the dynamics at M2 are more complicated than M1, considering the onshore and offshore translation of MBE, both assimilation runs (run 1 and run 2, Figure 15b, c) are capable of predicting the general vertical structure of the “true state” (Figure 15a). During the upwelling events on August 24-27, run 1 seems to overestimate temperature on upper layers (0-20 m). There is a shallowing of the thermocline during the upwelling events on August 28-30 and a deepening after August 30 (Figure 15a). Run 2 with the hybrid BEC successfully shows these variations (Figure 15c) while run 1 only predicts the shallowing of the thermocline during August 28-30 (Figure 15b).

Figure 16 shows the comparison of the vertical structure between model salinity and the “true state” at M2 mooring location. There are two halocline elevations evident during August 7-10 and August 28-30 (Figure 16a). Note that the “true state” is essentially an NCOM free run; thus, the shallowing and deepening of the thermocline and halocline of the “true state” do not indicate variation of the observation but only the variation of the NCOM model free run results. Both assimilation runs predict the first event of halocline shallowing during August 7-10. Run 1 shows agreement with the “true state” during the second halocline elevation event (August 28-30), but the salinity seems to be underestimated throughout the entire water column. The underestimation of salinity for run 2 is alleviated, but it still exists. Both run 1 and run 2 seem to deviate significantly from the “true state” during August 10-25, especially from the surface down to 30 m. Given a relatively small range of salinity variation (32.8 - 33.8) of the “true state” and complicated dynamics in this region, this amount of error is acceptable.

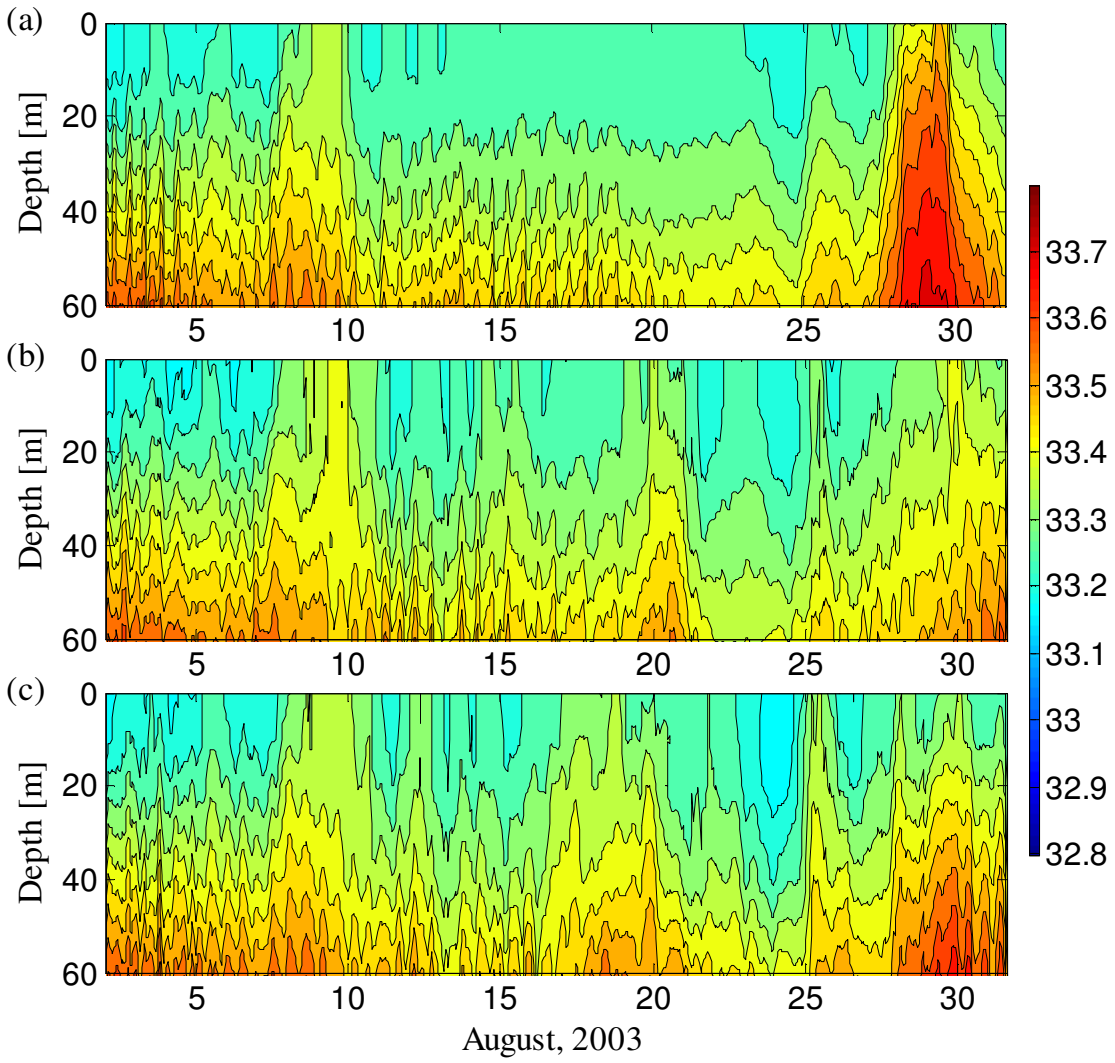


Figure 16. Temperature comparisons between model forecasts and "true state" at M2 mooring location from the surface down to 60 meters: (a) "true state"; (b) run 1; (c) run 2.

*c. Comparison of Model Forecast Skills*

To quantitatively measure the improvement of run 2 with respect to run 1, we utilize the assimilation skill examination method modified from Yaremchuk *et al*. (2011). The skill of assimilation $q(t)$ was estimated by calculating the normalized distances between the model forecasts and the true states:

$$q(t) = \frac{r_{\xi}^{twin}(t)}{r_{\max}} \tag{5.1.1}$$

where $r_{\xi}^{twin}(t)$ indicates distance between model forecasts and true states in state space (see section 3.7).

Since we are focused on comparing forecasts of run 1 and run 2, the maximum value $r_{\max}$ is chosen by:

$$r_{\max} = \max(r_{\max}^{run1}, r_{\max}^{run2}) \tag{5.1.2}$$

here $r_{\max}^{run1}$ is the maximum value of $r_{\xi}^{run1}(t)$ and $r_{\max}^{run2}$ is the maximum value of $r_{\xi}^{run2}(t)$ over the entire time interval.

Table 3. Comparison of temporally averaged normalized errors of assimilation runs.

| Run | Averaged normalized temperature error ($q_T$) | Averaged normalized salinity error ($q_S$) | Averaged normalized velocity error ($q_V$) |
|---|---|---|---|
| 1 | 0.65 | 0.62 | 0.60 |
| 2 | 0.55 | 0.52 | 0.53 |

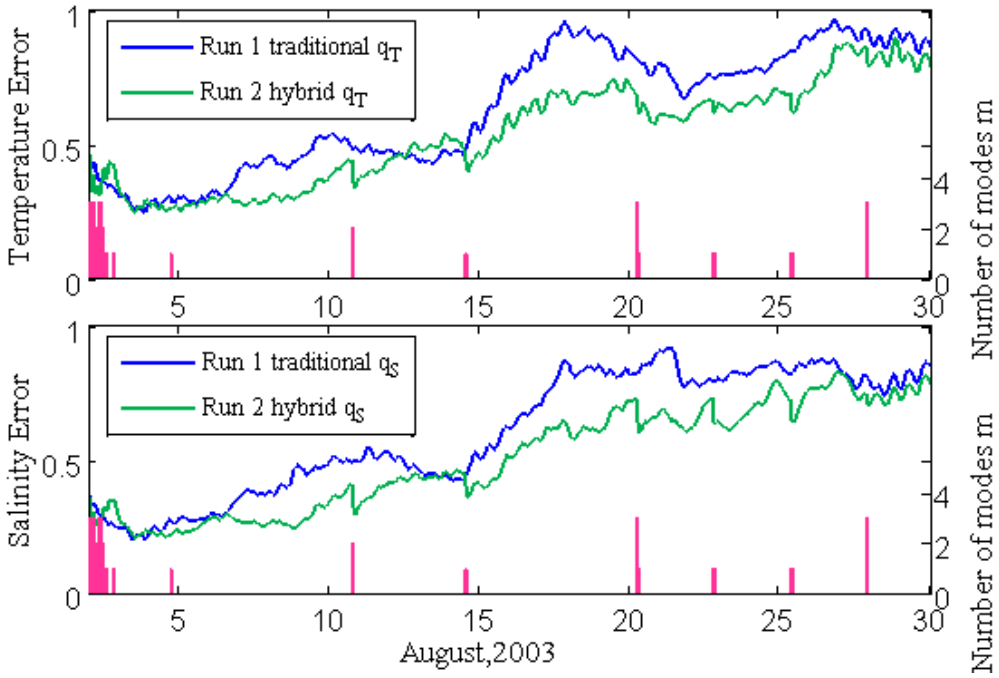


Figure 17. Normalized distance between "true state" and model solutions for run 1 and run 2: (a) temperature; (b) salinity.

Figure 17 compares the assimilation skill of run 1 and run 2. Both temperature error and salinity error have a tendency to grow with time in run 1 as well as in run 2. This is caused by the difference between the "true state" and the first guess. The first guess is generated by integrating NCOM for 712 hours stating from the initial condition specified by the fifth hour of the "true state" (see section 4.1). Hence, the initial difference between the "true state" and first guess is small, but the first guess fields deviate from the "true state" as time grows. Despite some higher $q_T$ and $q_S$ for run 2 (e.g., August 13-15, Figure 17a), the performance of run 2 is generally better than run 1. Table 2 shows that the time-averaged normalized temperature error is reduced from 0.65 (run1) to 0.55 (run 2), and the salinity error is reduced from 0.62 (run1) to 0.52 (run 2). The bar plot indicates the number of detected eigenvectors (right axis) during the assimilation run with hybrid BEC (run 2). Although the detected eigenvectors only present approximately 4% of the time, it is evident that the hybrid scheme has a positive impact in reducing both the temperature and salinity error.

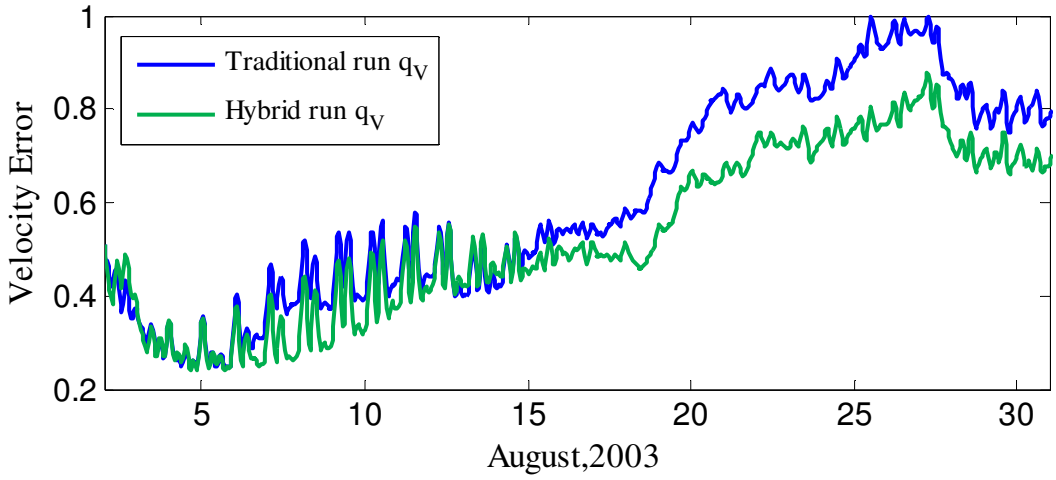


Figure 18. Normalized distance between velocity of the "true state" and model solutions.

The analysis of current velocity assimilation is beyond the scope of this study, but

the change of temperature and salinity fields caused by data assimilation still has a positive impact on model. Comparison of the normalized velocity error $q_V$ for runs 1 and 2 is given in Figure 18. It is evident that the overall velocity results of run 2 tend to be more accurate than those of run 1 except for the first few days and the 13th-14th in August. Time-averaged $q_V$ value is reduced from 0.60 to 0.53 for run 2 (Table 2).

## 5.2 Real Data Experiments I

Four runs (runs 3, 4, 5 and 6) are compared in real data experiments. To avoid confusion, runs 3, 4 and 6 are compared in real data experiment I (section 5.2). Runs 5 and 6 will be compared in real data experiment II (section 5.3).

*a. Comparison with Mooring Observations at 60 m*

Similar to twin data experiments, only the results from the 60 m level are presented here because we expect to see strong variability of the oceanic parameters and the largest discrepancies between the three model runs at this depth. While the direct influence of the surface fluxes (which are the same for all three runs) at the depth of 60m is significantly reduced, the impact of the length of analysis cycle on the quality of assimilation at this depth should be pronounced due to the high density of glider data (see Figure 10). Table 4 summarizes the characteristics of runs 3, 4, and 6 and the results of comparisons between these runs during upwelling and relaxation periods at 60m.

Table 4. Description of the NCOM free run and assimilation runs and comparisons of temperature and salinity solution errors at 60 meters in real data experiments.

| Run | Static BEC | Flow-dependent BEC | M1 August 15-26 temperature | | M1 August 12-26 salinity | | M2 August 17-21 temperature | | M2 August 17-21 salinity | |
|---|---|---|---|---|---|---|---|---|---|---|
| | | | Bias ($^o$C) | RMS ($^o$C) | Bias | RMS | Bias ($^o$C) | RMS ($^o$C) | Bias | RMS |
| 3 | No | No | 0.59 | 0.63 | -0.03 | 0.06 | 1.09 | 1.14 | -0.13 | 0.13 |
| 4 | Yes | No | 0.09 | 0.40 | -0.01 | 0.10 | -0.40 | 0.56 | -0.27 | 0.29 |
| 6 | Yes | Yes | -0.03 | 0.28 | 0.001 | 0.06 | 0.27 | 0.41 | -0.14 | 0.16 |

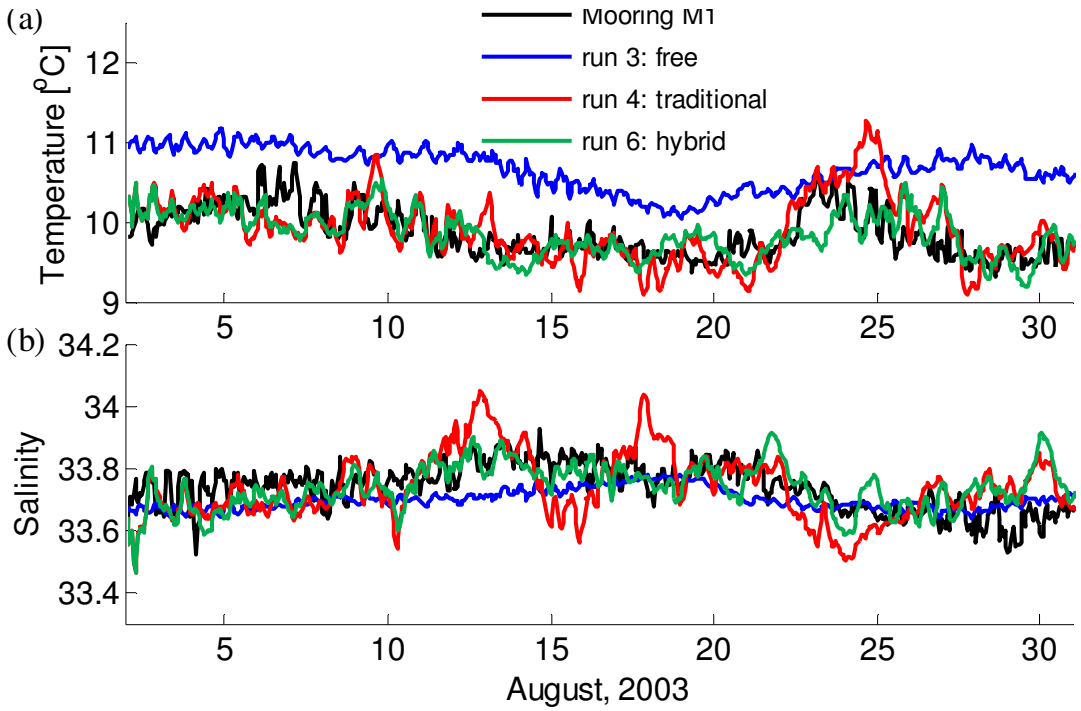


Figure 19. (a) Temperature comparisons between results of runs 3, 4 and 6 and observations at M1 mooring location at 60 m depth. (b) Salinity comparisons between the results of runs 3, 4 and 6 and observations at M1mooring location at 60 m depth.

Results from all 3 runs at 60 m as well as from mooring observations located at M1 are presented in Figure 19. The general behavior of the run 3 results does not match the M1 observations, and the magnitudes of both modeled temperature and salinity are considerably different from those observed. Temperatures predicted by run 3 are about 0.8°C higher than those observed over the whole model run period (Figure 19a), while salinity is about 0.05 lower than observations during August 2-18 (Figure 19b). Besides, the model fields of run 3 are too smooth to capture temporal variation of the observed temperature and salinity. Shulman *et al*. (2009) reported similar results for the free NCOM run.

Run 4 substantially improves model results by assimilating glider temperature and salinity data. Both temperature and salinity are in better agreement with observations. However, during the transition period from relaxation events to upwelling events (August

23-26) temperature solutions deviate considerably from observations (modeled temperature becomes about 0.8°C warmer, Figure 19a). During the same period, results of run 4 underestimate salinity by approximately 0.1 (Figure 19b). Salinity results of run 4 also show fluctuation with a magnitude of approximately 0.2 (Figure 19b) during upwelling events on August 12-19.

Run 6 successfully predicts both temperature and salinity variations (Figure 19), especially during the relaxation to upwelling transition period (August 23-26, for temperature) and August 12-26 (both upwelling and relaxation events, for salinity). Table 1 shows that the temperature bias is reduced from 0.09°C (run 4) to -0.03°C (run 6), and the RMS is reduced from 0.40°C (run 4) to 0.28°C (run 6) during August 15-26. Salinity bias is reduced from -0.01 (run 4) to 0.001 (run 6), and respective RMS is reduced from 0.10 (run 4) to 0.06 (run 6) during August 12-26.

Observations from the M2 mooring are also used to evaluate model results (Figure 20). As mentioned before, M2 is located in a dynamically complicated area where MBE moves onshore or offshore during wind relaxation and upwelling events (Rosenfeld *et al*., 1994; Ramp *et al*., 2005; Shulman *et al*., 2009). Similar to Figure 19, run 3 results deviate substantially from observations most of the time (Figure 20). Temperature predicted by run 3 is about 1.00°C higher than the observed temperature from August 10-27 (Figure 20a) while salinity is about 0.2 lower than observations during August 2-9 and 19-24 (Figure 20b). The highest bias of temperature (run 3) reaches 1.5°C on August 24 (Figure 20a). During the transition period from upwelling to relaxation events (Shulman *et al*., 2009) on August 17-21, run 4 underestimates temperature by approximately 0.8°C (Figure 20a). Salinity for both run 4 and run 6 differs substantially from observations

during this period and an earlier upwelling period (August 5-8, Figure 20b), indicating poor performance of the assimilation scheme at the M2 mooring location. This could be attributed to the complex dynamics of this region and to an insufficient number of glider observations during these periods (Figure 10). Nonetheless, the temperature bias is still reduced from -0.40°C (run 4) to 0.27°C (run 6) during August 17-21 and respective RMS bias is reduced from 0.56°C (run 4) to 0.41°C (run 6) (Table 4). The salinity bias for the same period is reduced from -0.27 (run 4) to -0.14 (run 6), and the respective RMS is also reduced from 0.29 (run 4) to 0.16 (run 6) (Table 4).

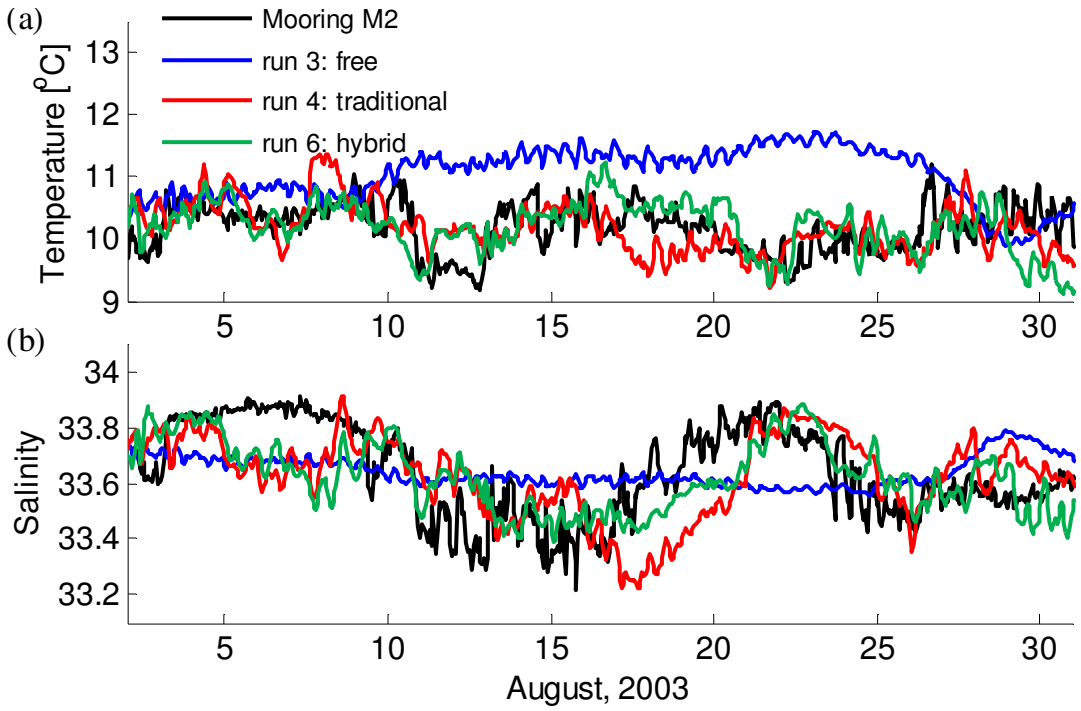


Figure 20. (a) Temperature comparisons between results of runs 3, 4, and 6 and observations at M2 mooring location at 60 m depth. (b) Salinity comparisons between results of run 3, 4 and 6 and observations at M2 mooring location at 60 m depth.

*b. Comparison with Mooring Observations throughout the Water Column*

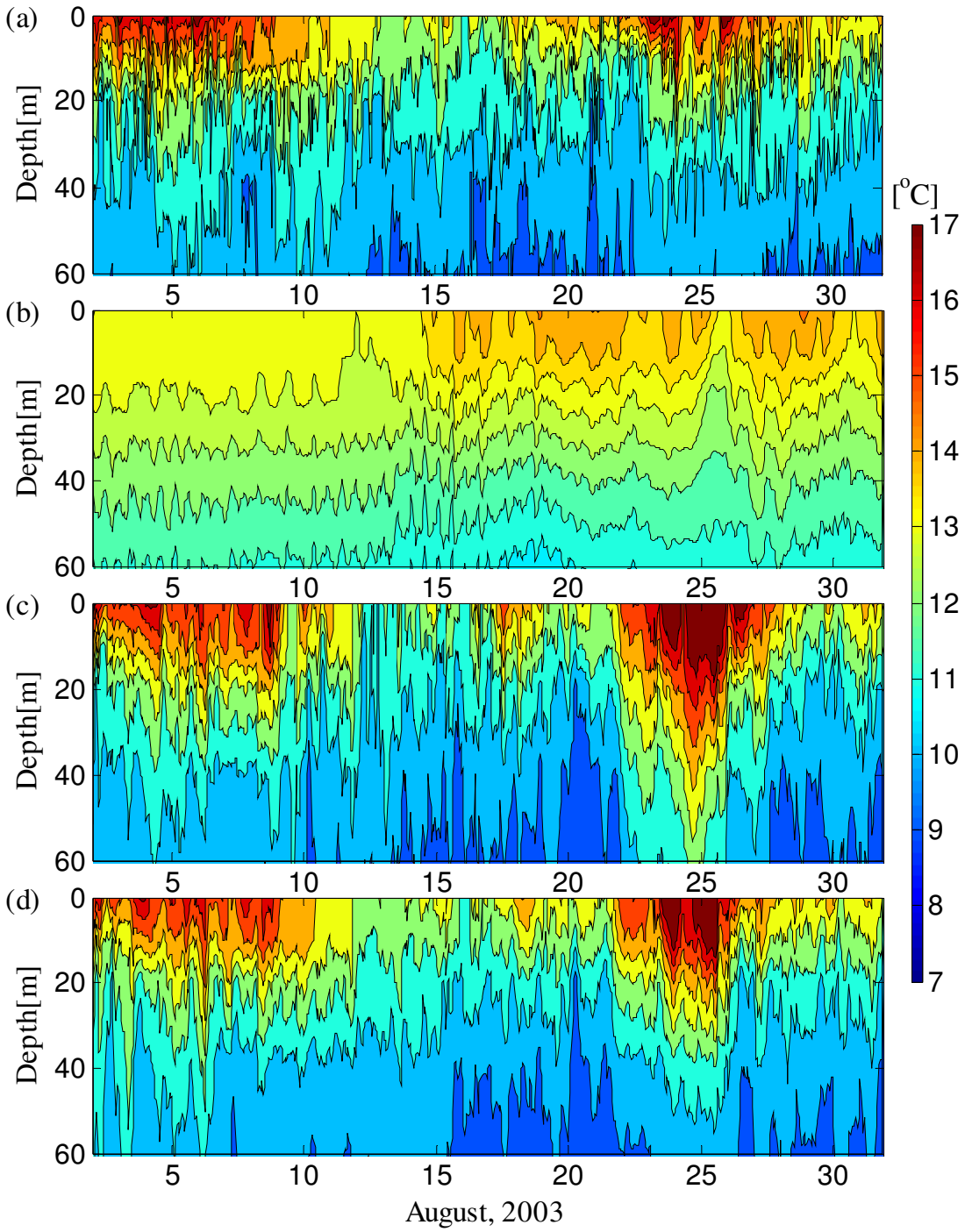


Figure 21. Temperature comparisons between model forecasts and the M1 mooring observations from the surface down to 60 m: (a) M1 mooring observations; (b) run 3; (c) run 4; (d) run 6.

Comparisons of model temperature fields with the M1 mooring observations over

the whole water column are presented in Figure 21. Assimilation of glider data (runs 4 and 6, Figure 21c, d) significantly improves model results as compared with the free model run (run 3, Figure 21b). Both runs 4 and 6, however, seem to overestimate temperature in the upper layer (0~30 m) on August 2-8 and 22-26 (Figure 21c, d). Excessive deepening of the thermocline with respect to observations during these two periods is also observed. This might be caused by the overestimation of short wave radiation (SWR) in COAMPS predictions (Shulman *et al*., 2009). The deepening of thermocline seems to be alleviated for run 6 as compared with run 4, especially on August 25 (Figure 21c, d). Overall, temperature solutions of runs 4 and 6 are similar. Both assimilation runs are capable of predicting major spatial and temporal variations of thermocline and vertical water column structure.

Vertical structure of salinity solutions and M1 observations are presented in Figure 22. Once again, the results of free model run are too smooth to capture temporal variations of corresponding salinity observations (Figure 22b). Both assimilation runs (run 4 and 6) are in good agreement with observations although results of both run 4 and run 6 are a little saltier than that observed at M1 mooring (Figure 22c, d). Given a relatively small range of salinity variation (32.6 - 34.0) and complicated dynamics in this region, this level of error is acceptable. There is a deepening of halocline during August 16-18 (Figure 22a). Run 4 (Figure 22c) isn't able to show this phenomenon while run 6 (Figure 22d) is. On August 18 (upwelling events) and August 22 (relaxation events), salinity for run 4 is overestimated below 20 meters. For run 6 results during the same period, the overestimation of salinity is alleviated.

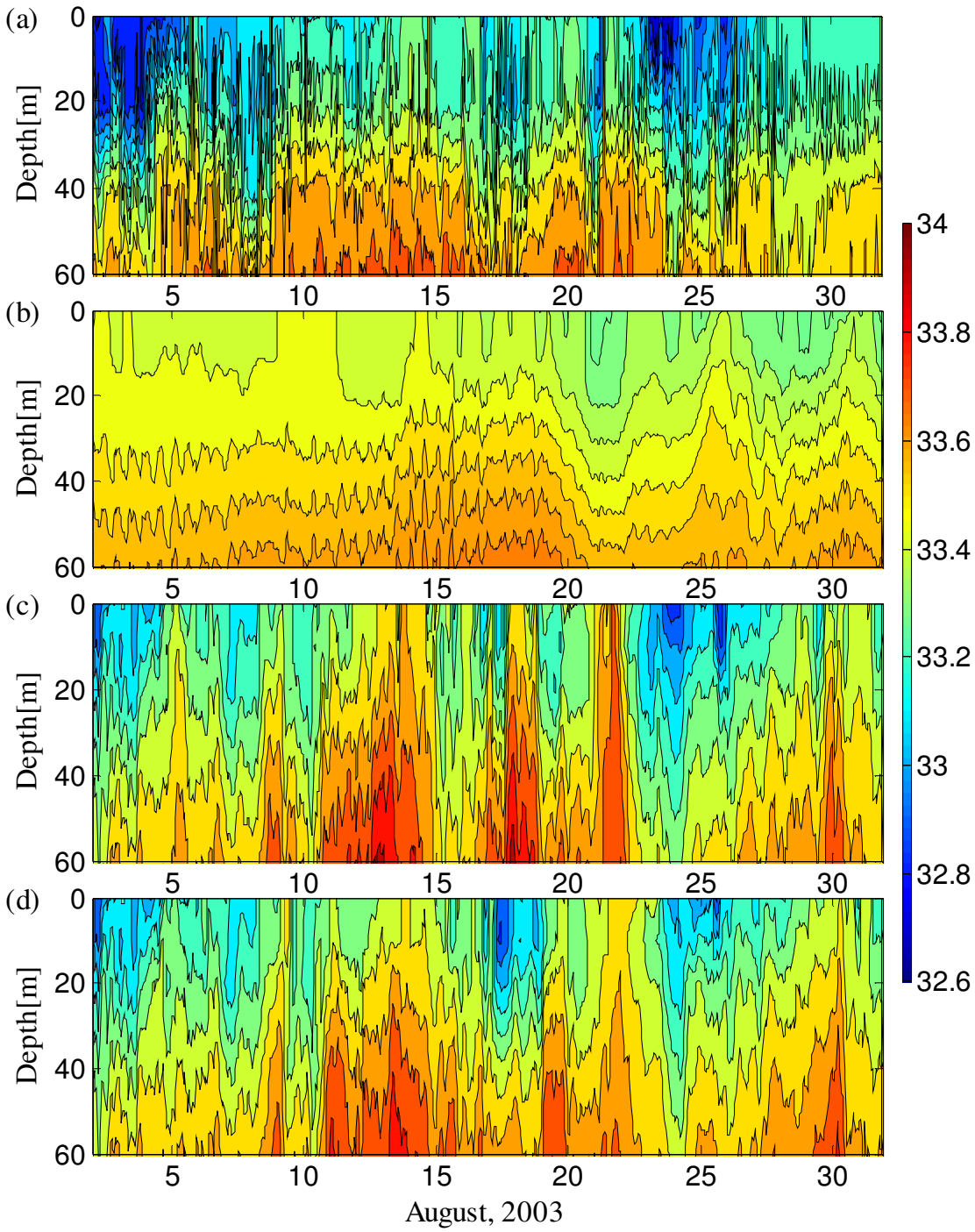


Figure 22. Salinity comparisons between model forecasts and the M1 mooring observations from the surface down to 60 m: (a) the M1 mooring observations; (b) run 3; (c) run 4; (d) run 6.

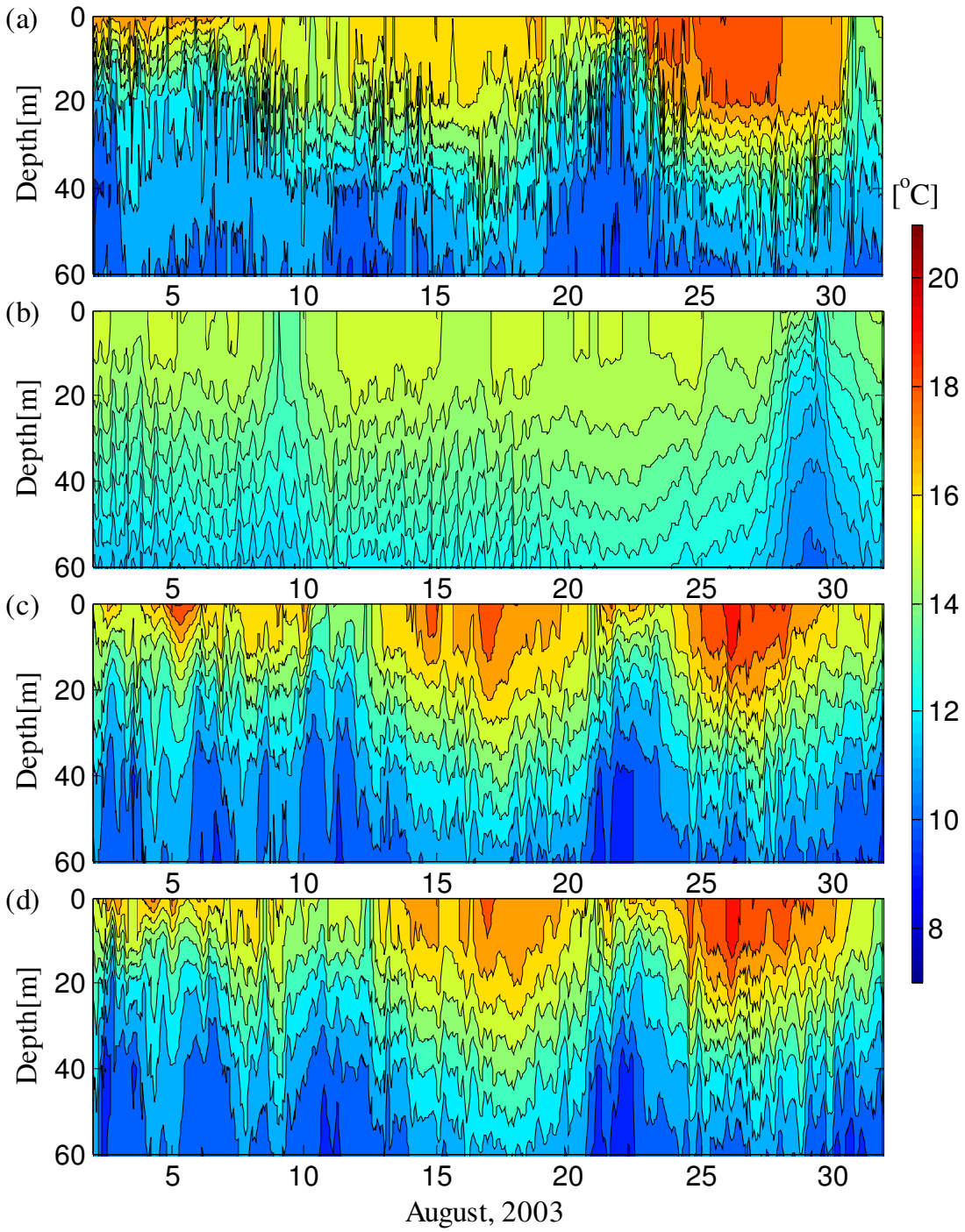


Figure 23. Temperature comparisons between model forecasts and the M2 mooring observations from the surface down to 60 m: (a) the M2 mooring observations; (b) run 3; (c) run 4; (d) run 6.

Figure 23 compares the vertical structure of model temperature with observations at the M2 mooring location. Similar to M1 mooring location, results from the NCOM free

run (run 3, Figure 23a) deviate significantly from observation. The two assimilation runs (runs 4 and 6, Figure 23c, d) are similar, and are both capable of predicting the general vertical structure of observations (Figure 23a). During the relaxation events on August 20-23, there is an evident elevation of the thermocline (Figure 23a) because of onshore translation of the MBE (Shulman *et al*., 2009). Both assimilation runs (run 4 and run 6, Figure 23c, d) are able to reproduce the shallowing of the thermocline during this period. The depths of the thermocline after relaxation events (August 25-30) for runs 4 and 6 seem shallower than observations (Figure 23c, d). Both assimilation runs overestimate the temperature below 55 meters (Figure 23c, d). These errors in assimilation runs could be affected by the NCOM free run at deeper water (below 50 meters) and during August 25-30. The complicated dynamics at the M2 mooring could also affect the assimilation results.

Figure 24 presents the comparison of the vertical structure between model salinity and observations at the M2 mooring location. Similar to the thermocline elevation in Figure 23a, there is also a shallowing of halocline when MBE moves onshore during relaxation events on August 20-23 (Figure 24a). Both assimilation runs successfully predict the halocline shallowing during this period (Figure 24c, d). Both run 4 and run 6 show a false elevation of halocline during August 14-16, once again demonstrating affection of NCOM free run (Figure 24b) to the assimilation. Run 4 has another false elevation of halocline during August 28-31 (Figure 24c) while run 6 is in better agreement with observations during this period (Figure 24d). There is also a shallowing of halocline in NCOM free run 3 (Figure 24b) during the same period, and run 4 seems to inherit this solution from the free run. The effect of the free run appears to be small for

the assimilation run 6 with the hybrid BEC scheme during this period.

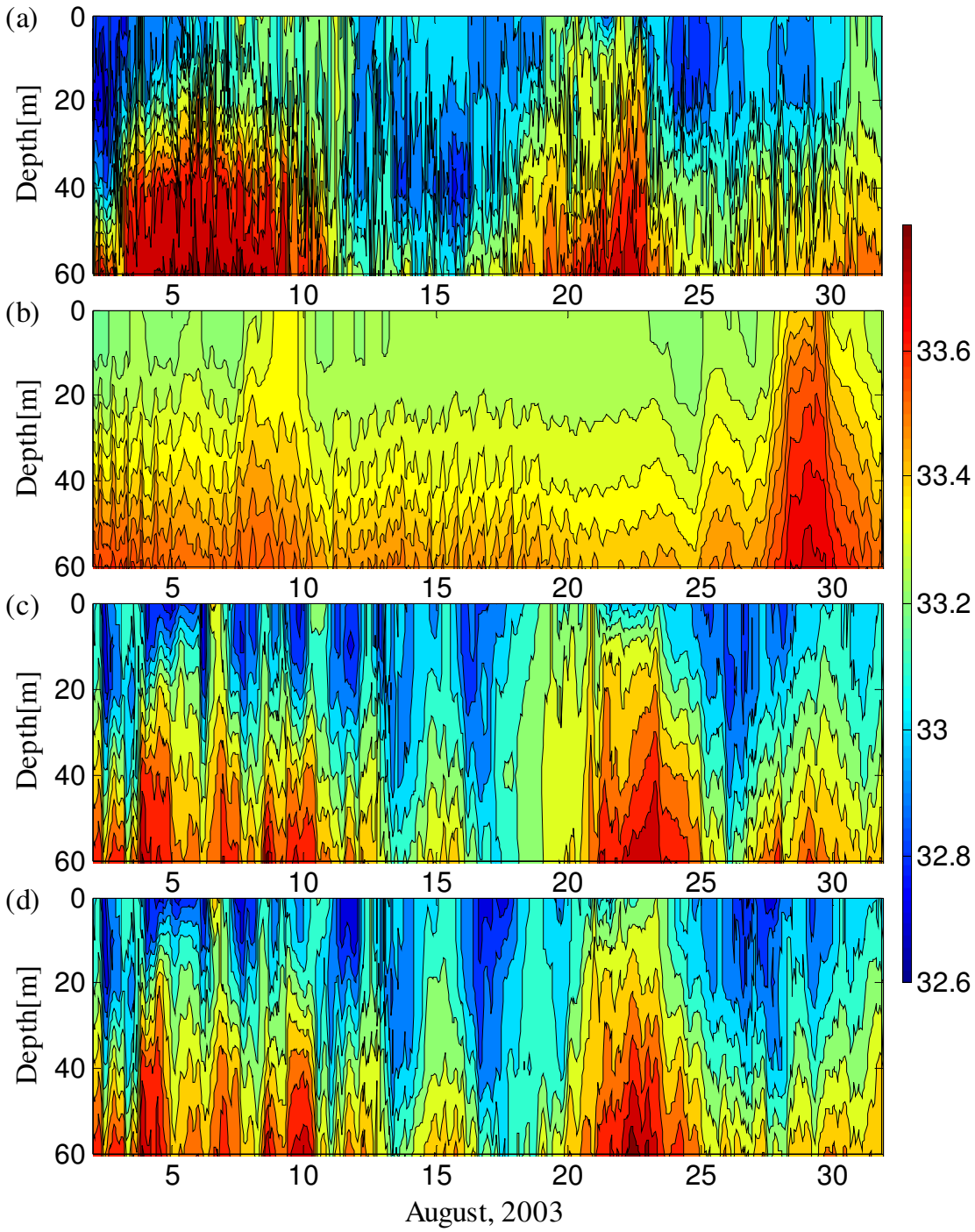


Figure 24. Salinity comparisons between model forecasts and the M2 mooring observations from the surface down to 60 meters: (a) the M2 mooring observations; (b) run 3; (c) run 4; (d) run 6.

*c. Comparison of Model Forecast Skills*

To measure the improvement of run 6 (assimilation run with hybrid BEC) with respect to run 4 (assimilation run with static BEC), model forecast skill examination method modified from Yaremchuk *et al*. (2011) is adopted here. The method is similar to the one used in twin data experiments. Given that there is no "true state" in real data experiments, a new parameter is introduced to examine the algorithm's performance. The normalized distance between the model forecast field $\xi_f$ and respective moored observations $\xi_m$ can be expressed by:

$$r_\xi = \left\langle (\xi_f - \xi_m)^2 \sigma_m^{-2} \right\rangle^{1/2} \tag{5.2.1}$$

where $\xi$ could be temperature, salinity or velocity. $\sigma_m$ denotes depth-dependent, temporal variance of moored temperature T, or salinity S, or horizontal velocity u and v. Angular brackets denote averaging over depth (surface to bottom) and over the two moorings.

The skill of assimilation $q(t)$ is estimated by dividing $r_\xi$ by a maximum value $r_{\max}$:

$$q(t) = \frac{r_\xi(t)}{r_{\max}} \tag{5.2.2}$$

Since we are focused on comparing assimilation run 4 and run 6, the maximum value $r_{\max}$ is chosen by:

$$r_{\max} = \max(r_{\max}^{run4}, r_{\max}^{run6}) \tag{5.2.3}$$

Table 5. Comparison of temporally averaged normalized errors of assimilation runs.

| Run | Averaged normalized temperature error ($q_T$) | Averaged normalized salinity error ($q_S$) | Averaged normalized velocity error ($q_V$) |
|---|---|---|---|
| 4 | 0.38 | 0.38 | 0.54 |
| 6 | 0.33 | 0.34 | 0.46 |

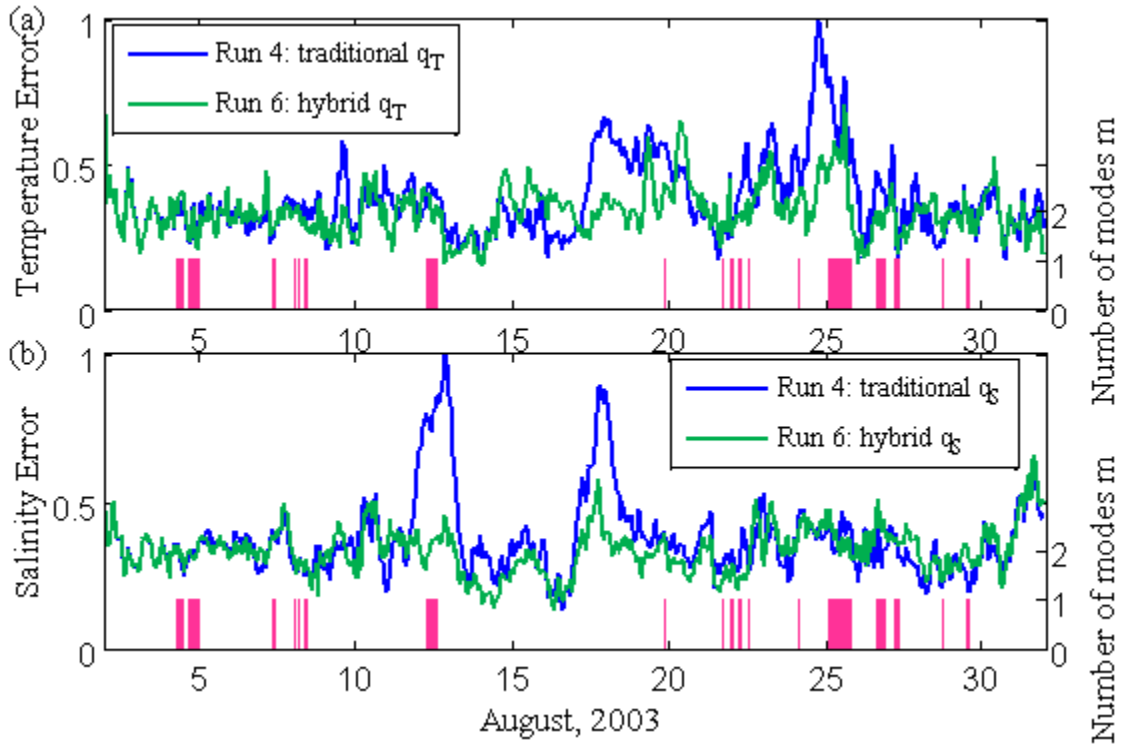


Figure 25. Normalized distance between moored observations and model forecasts for run 4 and run 6: (a) temperature; (b) salinity.

Figure 25 compares the assimilation skill of run 4 and run 6. Consistent with the single layer results comparison (Figure 19a), there is a normalized temperature error ($q_T$) peak near August 23-26 for run 4 (Figure 25a), indicating a loss of skill by the algorithm with only the static BEC. Run 4 also shows loosing of skill for temperature before relaxation events (August 17-20) (Figure 25a). This phenomenon is in agreement with the results of glider assimilation studies by different methods (Shulman *et al.*, 2009). Despite some higher $q_T$ for run 6 (e.g., August 14-17, Figure 25a), the performance of run 6 generally exceeds the performance of run 4. Table 5 shows that the time-averaged normalized temperature error is reduced from 0.38 to 0.33 for run 6. The bar plot shows the number of detected eigenvectors (right axis) during the assimilation run with hybrid BEC (run 6, Figure 25a). Although there is only 1 reliable eigenvector detected every

time when the eigen-modes present, the assimilation skill of run 6 still shows improvement as compared with run 4.

Comparison of salinity forecast skill for run 4 and run 6 is presented in Figure 25b. Run 4 exhibits two higher peaks of $q_S$ than run 6 during the upwelling periods August 12-14 and 17-19 (right before relaxation events), while $q_S$ of run 6 does not possess evident higher peaks than run 4. This suggests that the traditional assimilation scheme (with static BEC only) tends to lose skill during the transition from upwelling to relaxation events, especially for salinity results. According to Table 5, the time-averaged $q_S$ value is reduced from 0.38 to 0.34 for run 6.

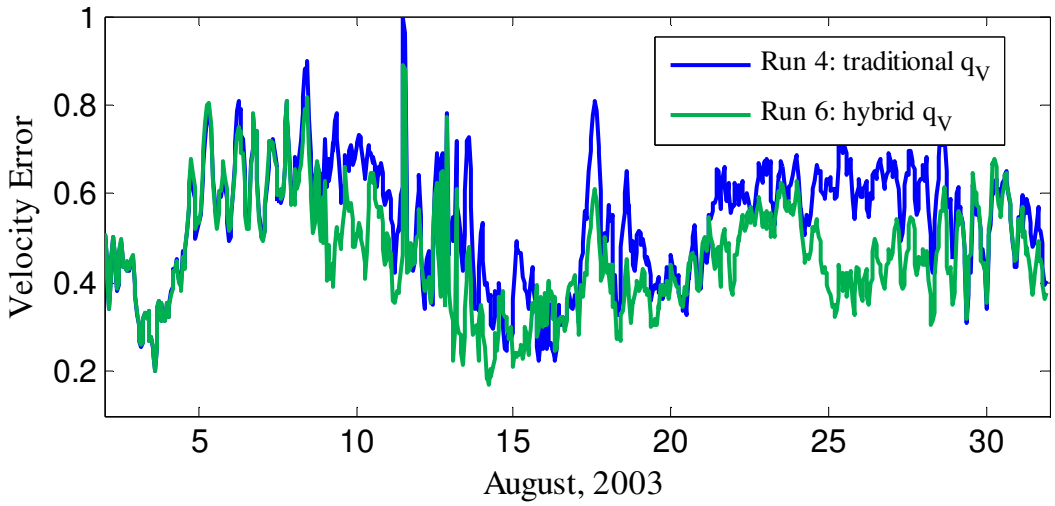


Figure 26. Normalized distance between moored velocity observations and model forecasts for assimilation run 4 and run 6.

Although there is no velocity assimilation involved in both assimilation schemes, the change of temperature and salinity fields resulting from glider data assimilation still has impact on velocity fields. A comparison of the normalized velocity error $q_V$ for runs 4 and 6 is presented in Figure 26. On the first few days of August, the $q_V$ from both runs seems to overlap with each other. During August 8-30, the normalized error of run 4 is

almost always larger than that of run 6, indicating that velocity fields of run 6 are closer to observations than run 4. Table 5 shows that the time-averaged $q_V$ value is reduced from 0.54 (run 4) to 0.46 (run 6).

## 5.3 Real Data Experiments II

The assimilation run without FTW (run 5) and the assimilation run with FTW (run 6) are compared in this section. Note that both runs use hybrid BEC scheme with the only difference being that the scheme used in run 6 includes the FTW (see section 3.3) and dynamical constraints (see section 3.4).

*a. Comparison with Mooring Observations at 60 m*

Similar to previous twin data experiments and real data experiments, only the results of 60 m level are present here. Table 6 summarizes the characteristics of run 5 and run 6 and the results of comparison between these two runs during upwelling and relaxation periods at 60m.

Table 6. Description of run 5 and run 6 and comparison of temperature and salinity errors at 60 meters during the transition from relaxation to upwelling events in real data experiments.

| Run | Hybrid BEC | FTW | M1 August 23-27 temperature | | M1 August 23-27 salinity | | M2 August 23-25 temperature | | M2 August 18-22 salinity | |
|---|---|---|---|---|---|---|---|---|---|---|
| | | | Bias ($^o$C) | RMS ($^o$C) | Bias | RMS | Bias ($^o$C) | RMS ($^o$C) | Bias | RMS |
| 5 | Yes | No | 0.80 | 0.85 | -0.07 | 0.10 | -0.48 | 0.63 | -0.18 | 0.20 |
| 6 | Yes | Yes | 0.12 | 0.31 | 0.02 | 0.06 | 0.24 | 0.43 | -0.13 | 0.15 |

Results from run 5 and run 6 at 60 m as well as the M1 mooring observations are presented in Figure 27. Temperature and salinity results from both runs are in good agreement with observations. However, during the transition period from relaxation to upwelling events (August 23-27), both temperature and salinity solutions from run 5 deviate considerably from observations. The highest biases are 1$^o$C for modeled

temperature (Figure 27a) and 0.8 for modeled salinity (Figure 27b). Run 6 also shows small fluctuation for both temperature and salinity during the same period (Figure 27), indicating instability of the hybrid scheme during the transition period from relaxation to upwelling. Nonetheless, the magnitude of fluctuation of run 6 is not as large as that of run 5. According to Table 1, temperature bias is reduced from 0.80°C (run 5) to 0.12°C (run 6), and the RMS is reduced from 0.85°C (run 5) to 0.31°C (run 6) during August 23-27. Salinity bias is reduced from -0.02 (run 5) to 0.02 (run 6), and respective RMS is reduced from 0.10 (run 5) to 0.06 (run 6) during the same period. At the very end of the model run (August 30-31), temperature predicted by run 5 is about 0.6°C higher than observations (Figure 27a) while salinity predicted by run 6 is about 0.2 higher than mooring salinity (Figure 27b). This could be attributed to the lack of observations during this period and to different ensembles used in the assimilation schemes.

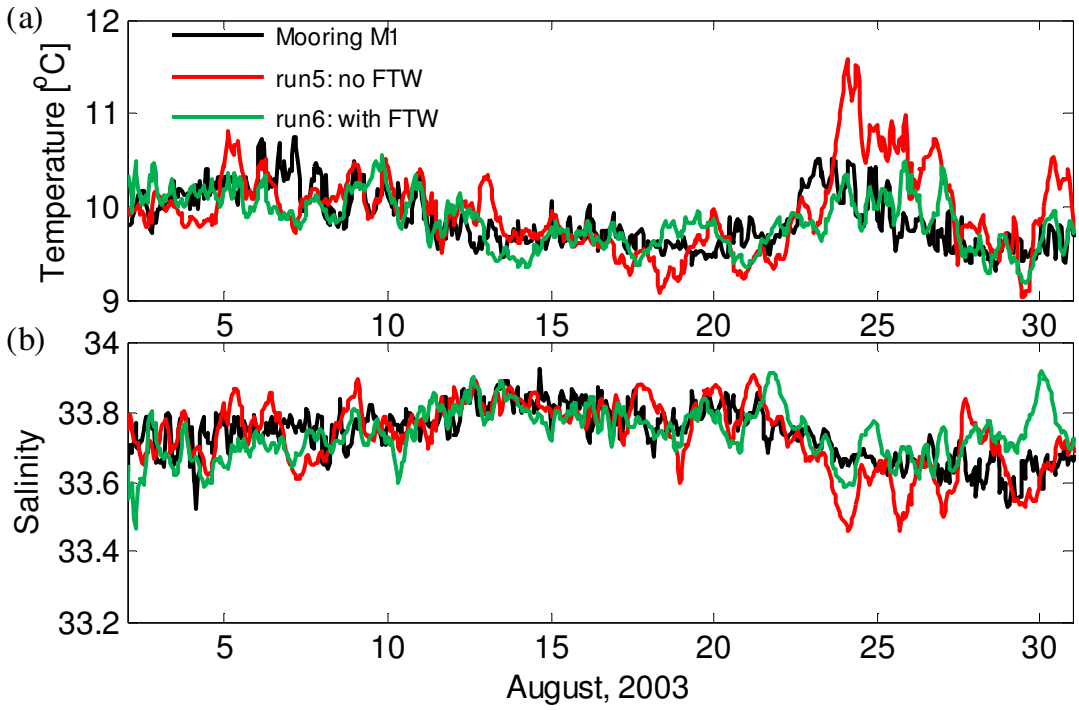


Figure 27. (a) Temperature comparisons between the results of run 5, run 6 and observations at the M1 mooring location at 60 m depth. (b) Salinity comparisons between the results of run 5, run 6 and observations at the M1 mooring location at 60 m depth.

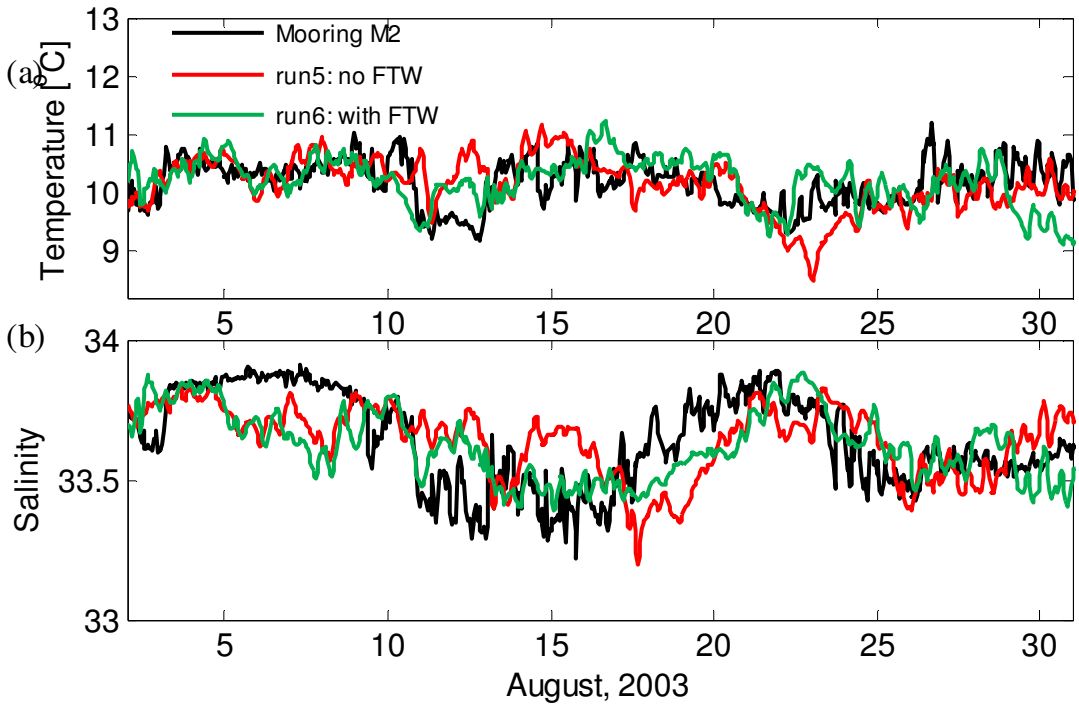


Figure 28. (a) Temperature comparisons between run 5, run 6 and observations at the M2 mooring location at 60 m depth. (b) Salinity comparisons between the results of run 5, run 6 and observations at the M2 mooring location at 60 m depth.

Figure 28 compares results from run 5 and run 6 at 60m and M2 mooring observations. During the transition period from relaxation to upwelling events on August 23-25, run 5 underestimates temperature by approximately 0.5°C (Figure 28a). The temperature bias is reduced from -0.48°C (run 5) to 0.24°C (run 6) during August 23-25 time period and respective RMS bias is reduced from 0.63°C (run 5) to 0.43°C (run 6; Table 6). Overestimation of temperature for run 5 can also be observed during upwelling events on August 12-15. During upwelling events on August 14-17, salinity predicted by run 5 are approximately 0.2 higher than observations while salinity results from run 6 are in better agreement with observations. Salinity from both run 5 and run 6 differs substantially from observations during the transition period from upwelling to relaxation (August 18-22) and during an earlier upwelling period (August 5-8, Figure 28b), indicating poor performance of assimilation scheme at the M2 mooring location.

Nonetheless, the salinity bias of the same period is still reduced from -0.18 (run 5) to -0.13 (run 6) and respective RMS is also reduced from 0.20 (run 5) to 0.15 (run 6) during August 18-22 (Table 6). Run 6 also underestimates both temperature and salinity at the end of model run (August 29-31). Once again the complex dynamics of this region and insufficient number of glider observations during these periods (Figure 10) could be the cause of these errors.

*b. Comparison with Mooring Observations throughout the Water Column*

Comparisons of model temperature fields from run 5 and run 6 with the M1 mooring observations over the whole water column are presented in Figure 29. Both runs 5 and 6 appear to overestimate temperature in the upper layer (0~30 m) during upwelling events on August 2-8 and during the transition period from relaxation to upwelling events on August 22-26 (Figure 29b, c). Excessive deepening of the thermocline with respect to observations during these two periods is also observed. As discussed on section 5.2b, this might be the result of overestimation of short wave radiation (SWR) in COAMPS predictions (Shulman *et al*., 2009). The false deepening of the thermocline seems to be alleviated for run 6 (Figure 29c) as compared with run 5 (Figure 29b), especially on August 25. The general vertical structure of temperature solutions from runs 5 and 6 are similar. Both assimilation runs are capable of predicting major spatial and temporal variations of thermocline and vertical water column structure. However, it is important to keep in mind that the computational cost of run 6 is much lower than that of run 5 because of the implementation of FTW in run 6.

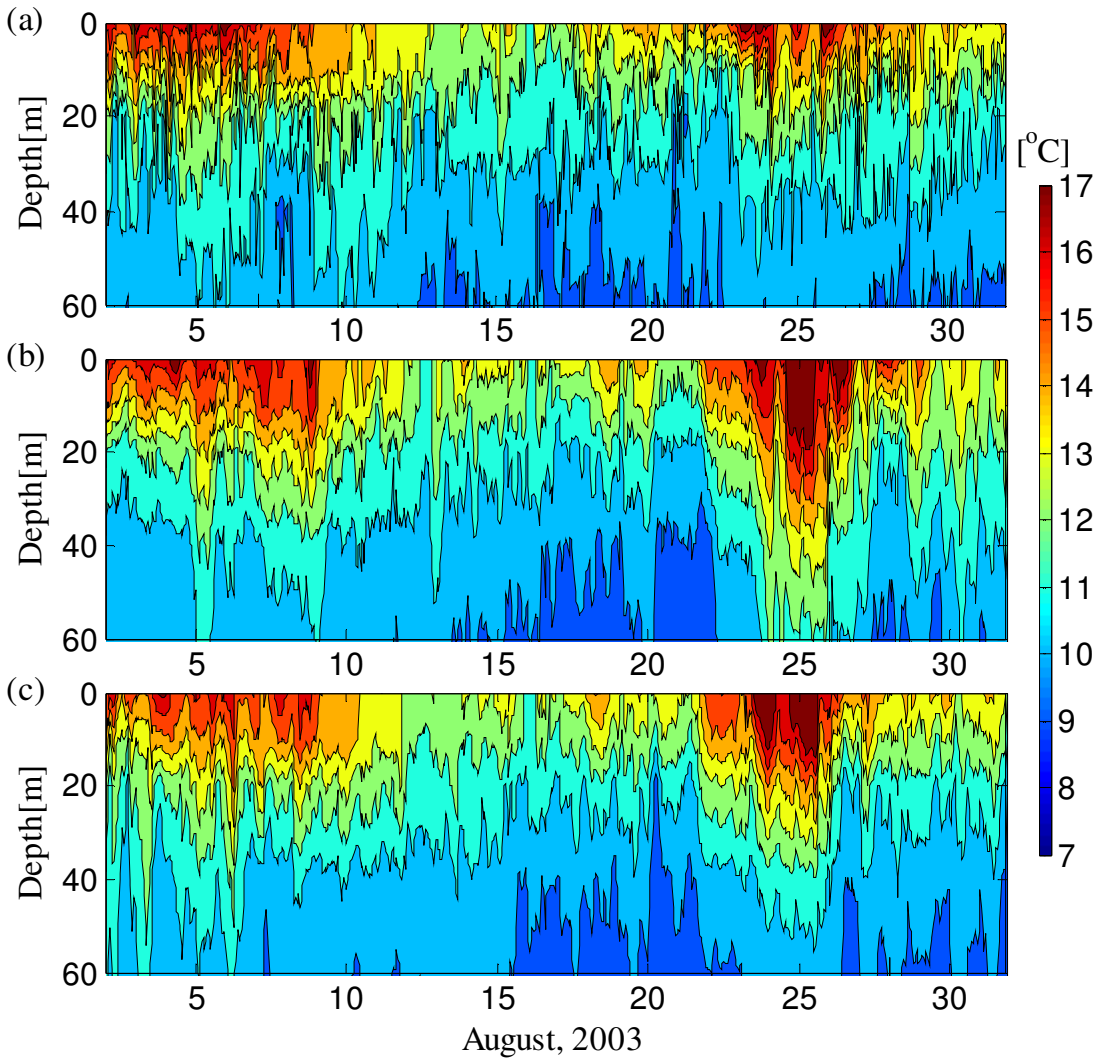


Figure 29. Temperature comparisons between model forecasts and the M1 mooring observations from the surface down to 60 meters: (a) the M1 mooring observations; (b) run 5; (c) run 6.

Figure 30 compares vertical structure of salinity solutions from run 5 and run 6 as well as the M1 mooring salinity observations. Both assimilation runs (run 5 and run 6) are in good agreement with observations despite the fact that results of both run 5 and run 6 are a little saltier than observed salinity at the M1 mooring (Figure 30b, c). A relatively small range of salinity variation (32.6 - 34.0) and complicated dynamics seem to raise more difficulties for data assimilation in this region. Run 5 (Figure 30b) isn't able to

predict the deepening of the halocline during August 16-18 (Figure 30a). During wind relaxation on August 21-22, the salinity from run 5 is overestimated for the whole water column. For the run 6 results during the same period, the overestimation of salinity is alleviated.

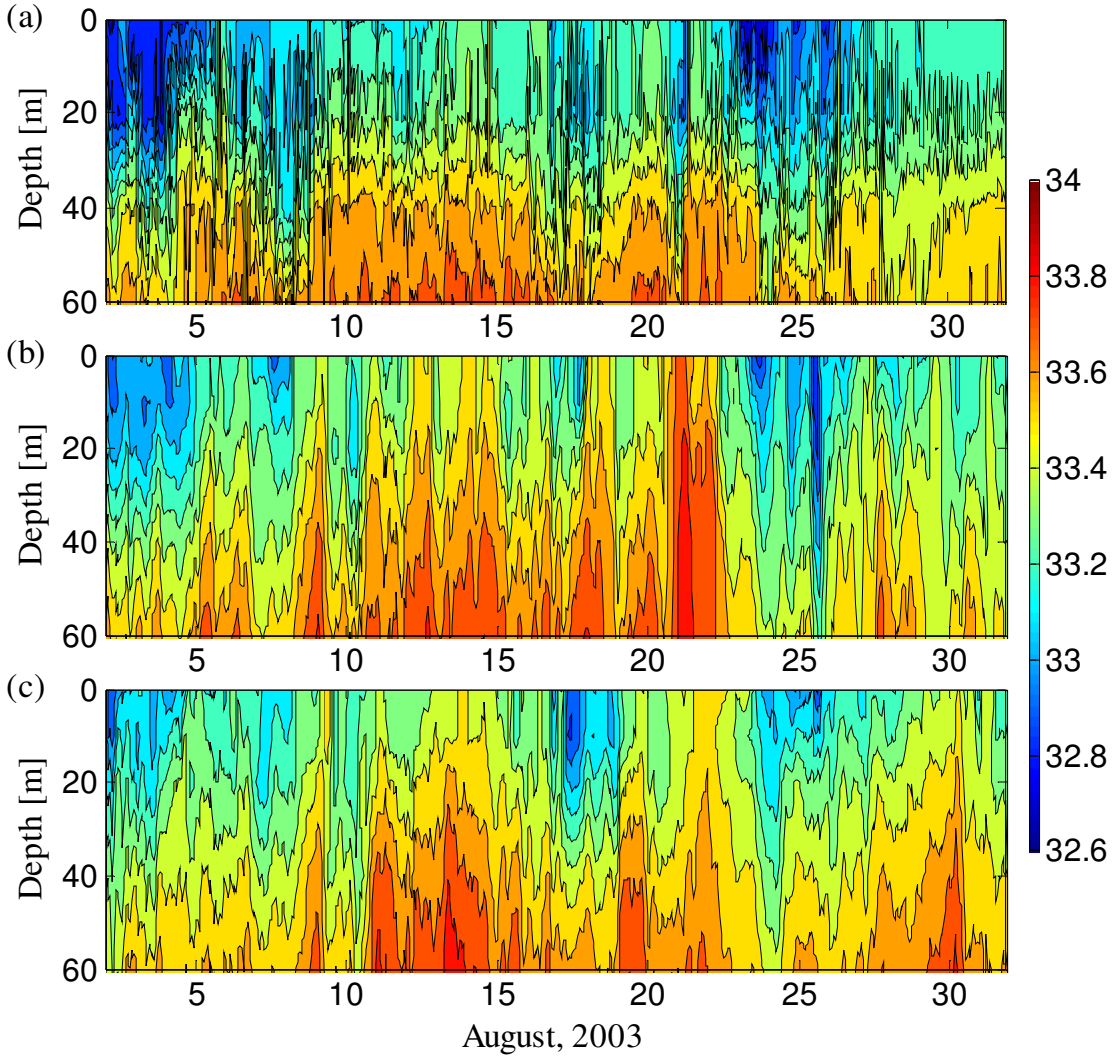


Figure 30. Salinity comparisons between model forecasts and the M1 mooring observations from surface down to 60 meters: (a) the M1 mooring observations; (b) run 5; (c) run 6.

Vertical structure of temperature solutions and the M2 mooring observations are presented in Figure 31. Overall, run 4 and run 6 (Figure 31b, c) are similar, and they are

both capable of predicting the general vertical structure of observations (Figure 31a), including the shallowing of the thermocline during the relaxation events on August 20-23 and the deepening of the thermocline after the relaxation events (August 23-28). Both assimilation runs seem to overestimate surface temperature on August 17-19 and 25-26, which could also be attributed to the overestimation of short wave radiation (SWR) in COAMPS predictions. But the overestimation of temperature is not as severe as at the M1 mooring location in Figure 29.

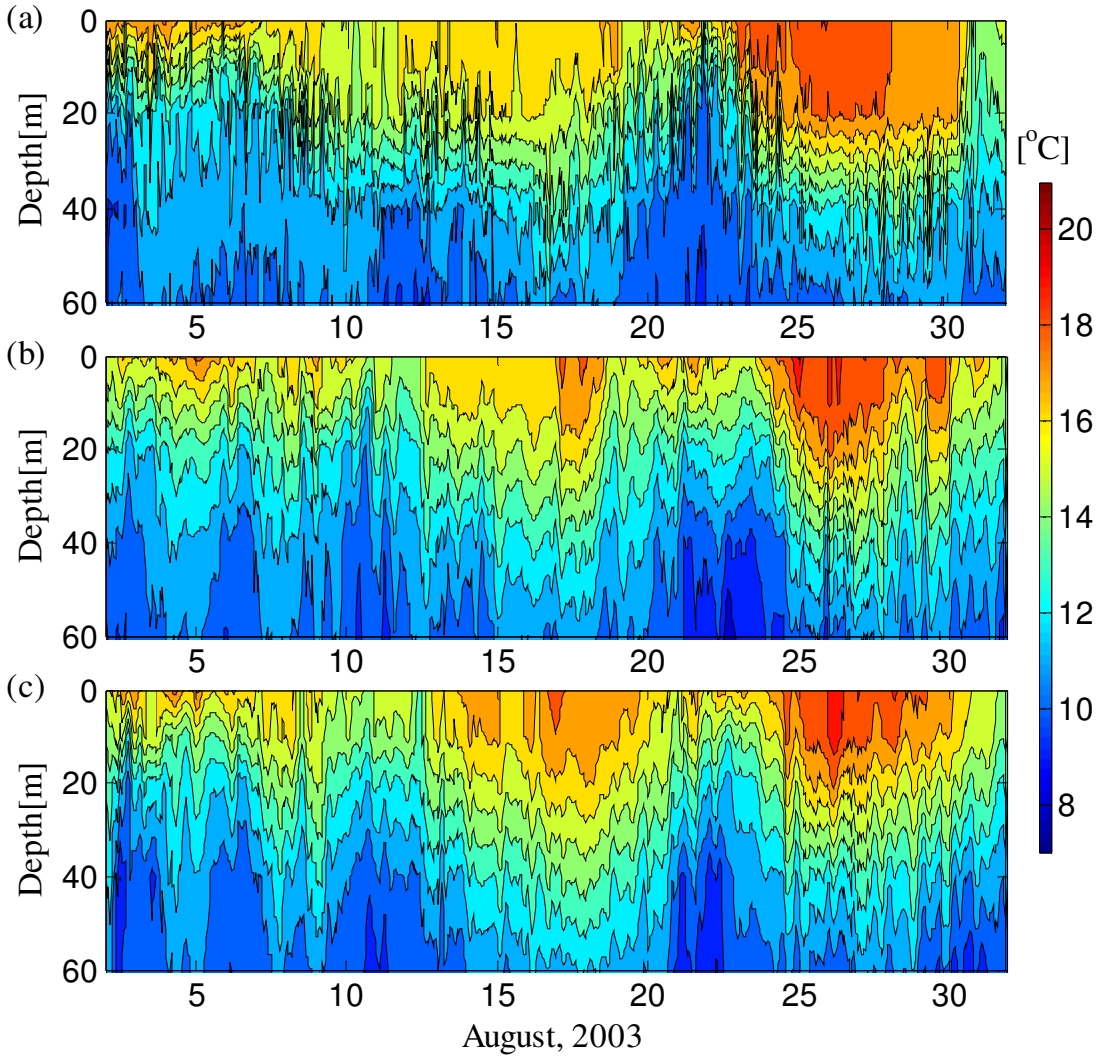


Figure 31. Temperature comparisons between model forecasts and the M2 mooring observations from the surface down to 60 m: (a) the M1 mooring observations; (b) run 5; (c) run 6.

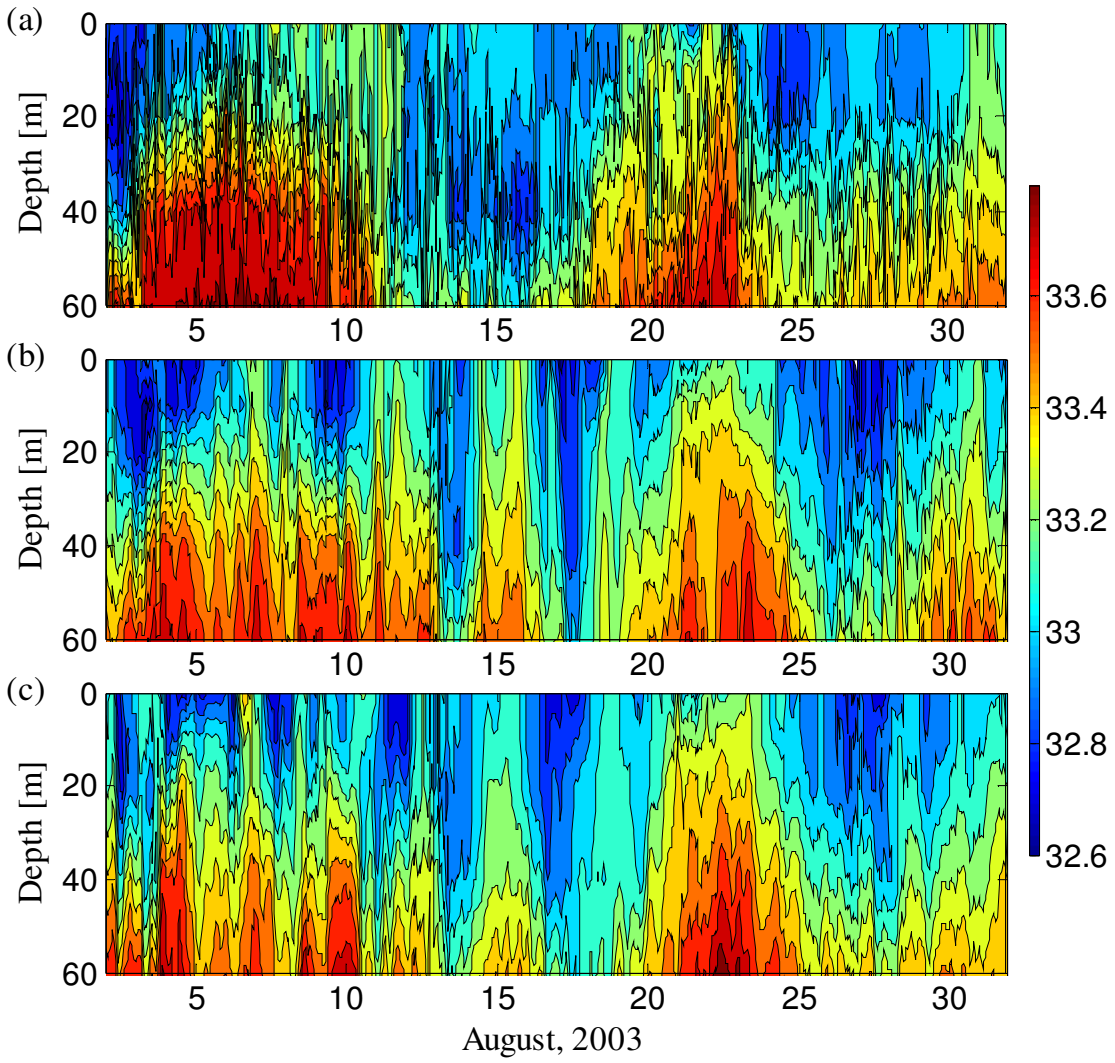


Figure 32. Salinity comparisons between model forecasts and the M2 mooring observations from the surface down to 60 m: (a) the M1 mooring observations; (b) run 5; (c) run 6.

Figure 32 displays the comparison of the vertical structure between model salinity from run 5 and run 6 and observations at the M2 mooring location. Both assimilation runs successfully predict the halocline shallowing during wind relaxation events on August 20-23 (Figure 24c, d). The false elevation of halocline during August 14-16, which is showed in both run 4 and run 6, is also presented in run 5. The magnitude of overestimation of salinity of the whole water column during this period for run 5 appears

to be larger than that for run 6. Unlike run 4 (Figure 24c), both run 5 and run 6 are free of inheriting the false elevation of halocline from the free run (August 28-31, Figure 24b), indicating a minor influence of the free run to the hybrid schemes.

*c. Comparison of Model Forecast Skills*

Similar to section 5.2c, equations (5.2.1) and (5.2.2) are used to measure data assimilation skills. Since the comparison is made between run 5 and run 6, $r_{\max}$ is thus chosen by

$$r_{\max} = \max(r_{\max}^{run5}, r_{\max}^{run6}) \qquad (5.3.1)\ .$$

Table 7. Comparison of temporally averaged normalized errors of assimilation run 5 and run 6.

| Run | Averaged normalized temperature error ($q_T$) | Averaged normalized salinity error ($q_S$) | Averaged normalized velocity error ($q_V$) |
|---|---|---|---|
| 5 | 0.42 | 0.51 | 0.49 |
| 6 | 0.37 | 0.47 | 0.36 |

Figure 33 compares the assimilation skill of run 5 and run 6. Although there are some higher $q_T$ values for run 6 (e.g., August 19-21, Figure 33a), the performance of run 6 is generally better than that of run 5, especially during the transition period from relaxation to upwelling events on August 23-26 and 30-31 (Figure 33a). The normalized temperature error ($q_T$) peak near August 23-26 for run 5 (Figure 33a) indicates a loss of skill by the algorithm with the full ensemble. Table 7 shows that the time-averaged normalized temperature error is reduced from 0.42 (run 5) to 0.37 (run 6).

Comparison of salinity forecast skill for run 5 and run 6 is presented in Figure 33b. Run 5 has several higher peaks of $q_S$ than run 6, the most evident ones being on August

21 (relaxation events), August 27 and 29 (upwelling events). Run 6 also has some higher $q_S$ values than run 5, but the magnitude of $q_S$ peaks for run 6 is generally not as evident as those in run 5. This indicates that the hybrid assimilation scheme with FTW adjustment tend to be more stable than the hybrid scheme with the full size ensemble, especially during relaxation events (for salinity) and the transition period (for temperature). According to Table 7, the time-averaged $q_S$ value is reduced from 0.51 to 0.47 for run 6.

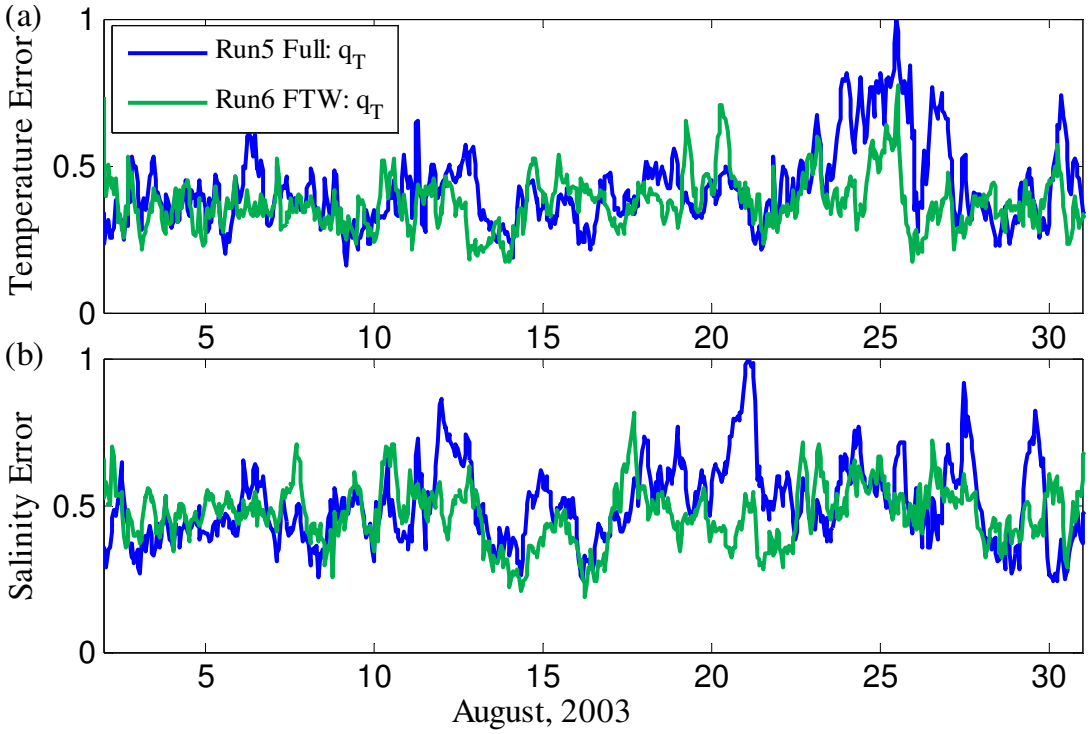


Figure 33. Normalized distance between moored observations and model forecasts for run 5 and run 6: (a) temperature; (b) salinity.

Comparison of the normalized velocity error $q_V$ for runs 5 and 6 is presented in Figure 34. On August 2-7, the $q_V$ from run 6 appears to exceed that of run 5. Starting on August 8, the normalized error of run 5 starts to surpass that of run 6 and keeps showing higher error values until the end of August (except a small peak of run 6 on August 17-

18). The higher $q_V$ values of run 5 from the beginning of relaxation events until August 30 indicates that the hybrid scheme with FTW substantially improves the forecast skill during this period. Table 7 shows that time-averaged $q_V$ value is reduced from 0.49 (run 5) to 0.36 (run 6).

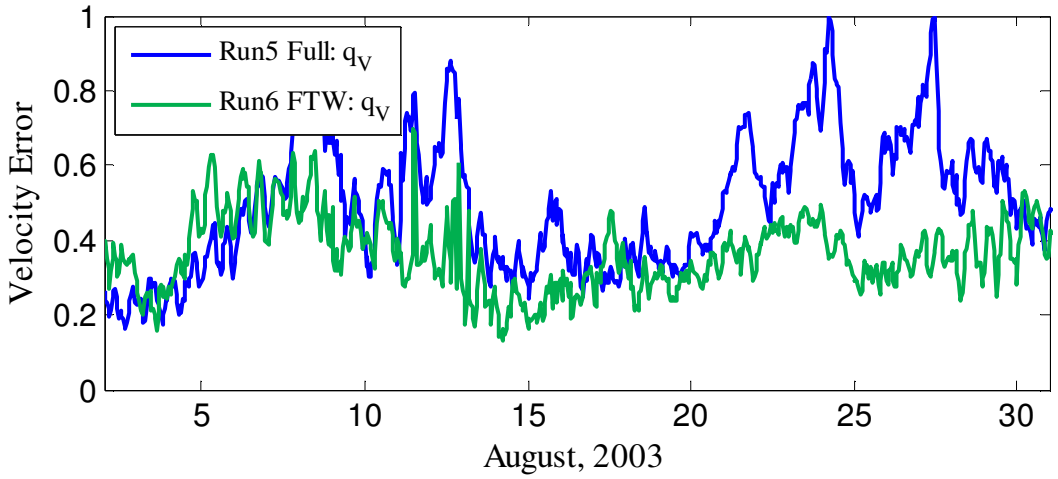


Figure 34. Normalized distance between moored velocity observations and model forecasts for assimilation run 5 and run 6.

## 5.4 Comparison with Historical Research

Monterey Bay is a dynamically complicated region where eddies, meanders, upwelling filaments and fronts of different water masses can be observed throughout the year (Chelton, 1984; Batteen and Vance, 1998). During a specific time period, such as upwelling events or wind relaxation events, the physical phenomena in this region were observed to be similar although temporal and spatial variations do exists (Shulman *et al.*, 2002; Ramp *et al.*, 2005; Shulman *et al.*, 2009). As a successful data assimilation system, the numerical model with hybrid 3D-VAR scheme should be able to reproduce the major dynamical features in the Monterey Bay. Hence, we will compare the model results (with hybrid 3D-VAR scheme) with historical observation records in this section. To

emphasize the effect of data assimilation, the results from model free run (without data assimilation) will also be presented for comparison.

*a. Monterey Bay Eddy (MBE)*

The most distinct feature of Monterey Bay area is the permanent, anti-cyclonic, warm core eddy, which is part of the CC meander and is termed Monterey Bay Eddy (MBE, see section 2.6). The onshore-offshore translation of MBE has been described regularly in previous studies (Rosenfeld *et al*., 1994; Ramp *et al*., 1997; Ramp *et al*., 2005).

Ramp *et al*. (2005) reported an event of MBE moving onshore during a wind relaxation period on August 27-31, 2000 (Figure 35). According to Ramp *et al*., the front that distinguishes MBE from ambient water is the 14 - 14.5$^{o}$C isotherm (yellow to light green in Figure 35). The location of this front on August 27 was 122.35 $^{o}$W (Figure 35A), and 122.30 $^{o}$W on August 28 (Figure 35B). Although the front stopped moving eastward on August 29, it expanded southward and the center temperature of the eddy was also elevated (Figure 35C). The front continued to translate eastward to 122.25 $^{o}$W on August 30 (Figure 35D). By August 31, the eddy front could not be identified due to the local surface heating (Figure 35E).

Surface temperature and velocity fields from NCOM with hybrid 3D-VAR scheme also show onshore translation of MBE during wind relaxation events on August 20-23 in 2003 (Figure 36, right panel). In order to highlight the data assimilation solutions, the results of the NCOM free run are presented on the left panel of Figure 36.

Before the relaxation events (August 19, Figure 36a, right panel), the location of the MBE front (14-14.5$^{o}$C, yellow to green in Figure 36) was 36.55 $^{o}$N, 122.20 $^{o}$W. When the

wind relaxation began on August 20, this front moved eastward to 122.15 $^{o}$W (Figure 36b, right panel) and started to expanded southward (Figure 36c, right panel). By 14:00 on August 21, the surface temperature of most of the area had exceeded 14.5$^{o}$C except the water inside the Bay, and the MBE front had reached south of the Bay mouth (Figure 36d, right panel). The pattern of eastward movement and southward expansion is very similar to the observations reported by Ramp *et al*. (2005) (Figure 35), although the moving distance of the MBE front (from 122.20 $^{o}$W to 122.15 $^{o}$W) is shorter than their results (from 122.35 $^{o}$W to 122.25 $^{o}$W). NCOM free run results (without data assimilation) was able to simulate the existence of the MBE outside of the Bay mouth, but the surface temperature of the entire region is relatively lower than the results produced by data assimilation NCOM run (Figure 36, left panel). Moreover, the onshore translation of the MBE simulated by the model free run is not as evident as the results from the data assimilation run.

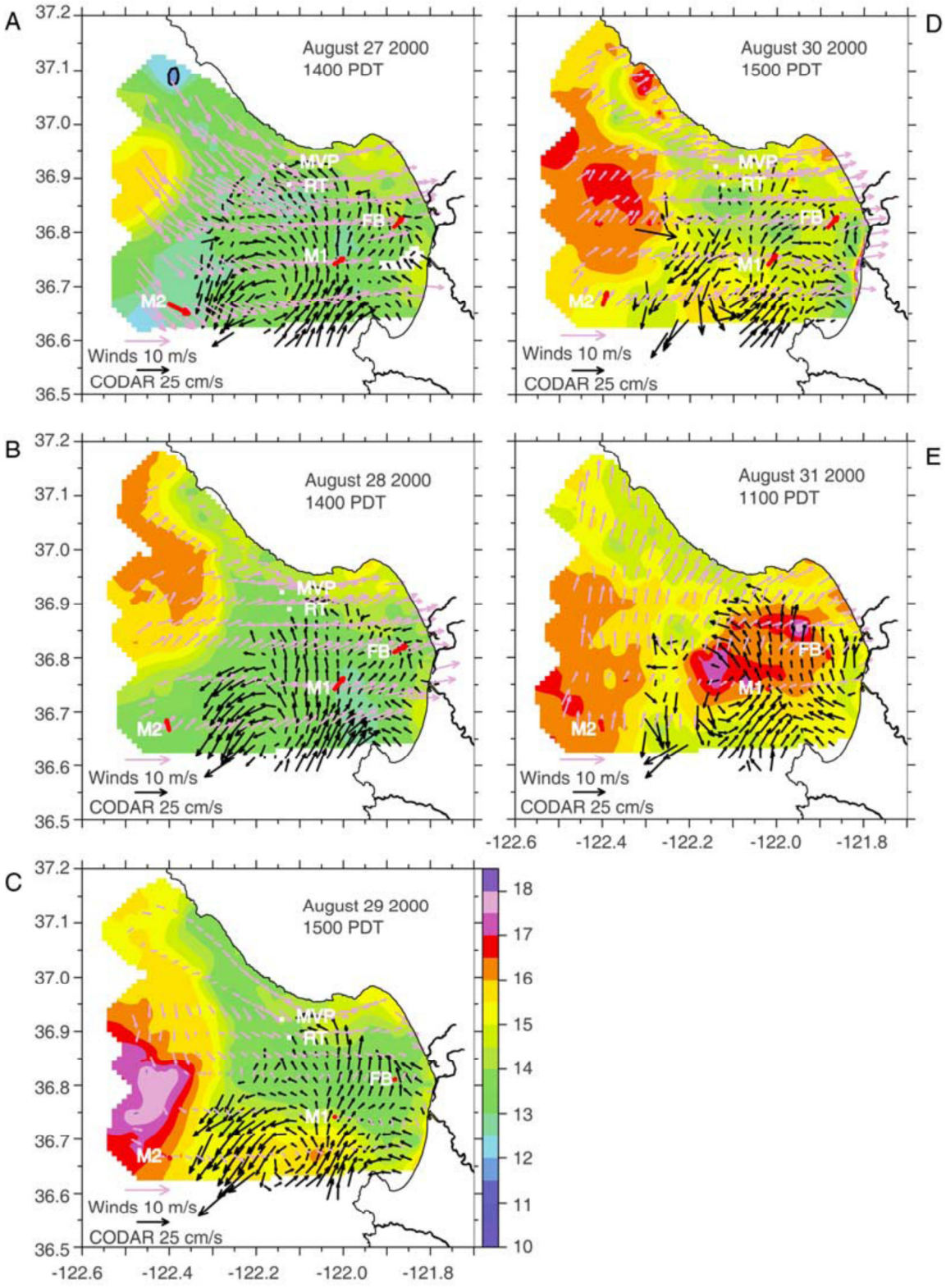


Figure 35. A time series of surface temperature and velocity measured by aircraft and in situ data during a wind relaxation event in August 2000 (Ramp *et al*., 2005)

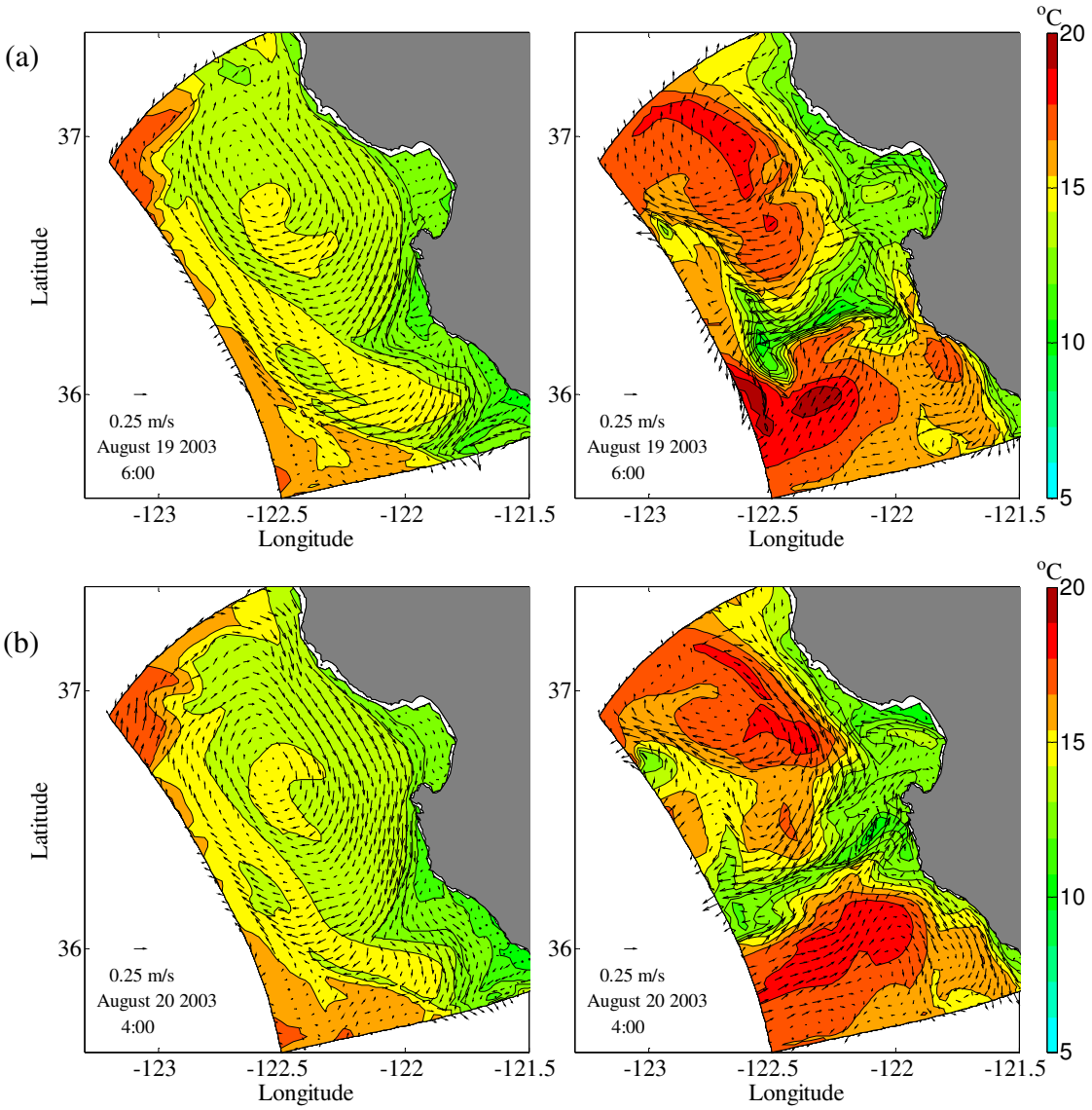


Figure 36. Time series of surface temperature and velocity fields from NCOM free run (left panel) and NCOM data assimilation run (right panel) from August 19-21, 2003.

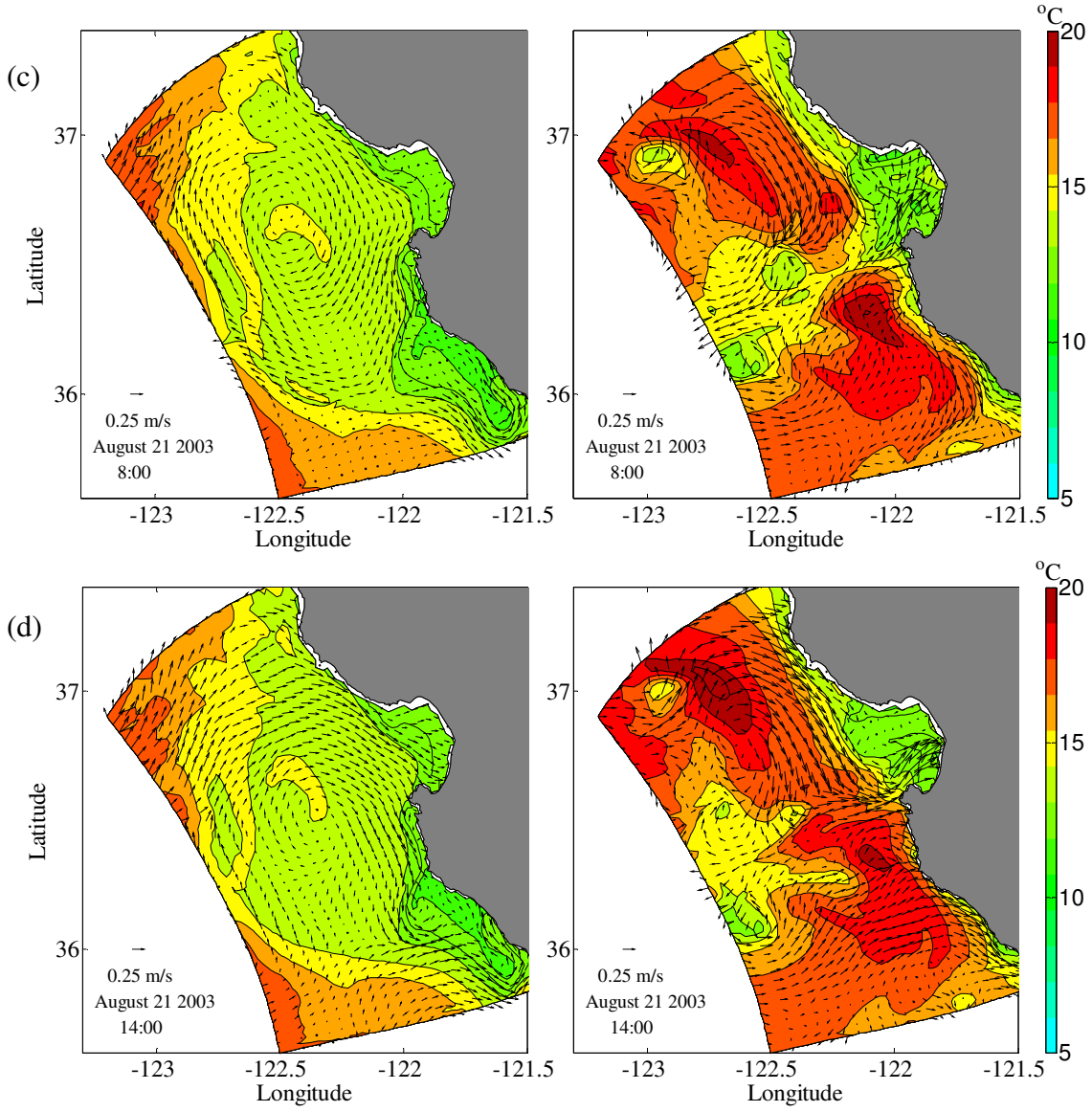


Figure 36. (continued).

The onshore translation of the MBE normally followed by the MBE moving offshore when the wind relaxation period ends and northwesterly wind starts (Rosenfeld *et al*., 1994; Ramp *et al*., 1997; Ramp *et al*., 2005). Figure 37 presents NCOM results during the second upwelling event from August 24 to 29. The offshore translation of MBE during this period can be tracked, again, by pinpointing the maximum eastward position of the MBE front 14.0-14.5°C (yellow to green in Figure 37). Although the

relaxation event ends on August 23, the MBE front was still lingering at the mouth of the Bay on August 24 (Figure 37a, right panel). From August 24 to 26, there was still no sign of retreating of the MBE, and the front even moved further eastward into the Bay (Figure 37b, right panel). On August 27, the surface temperature near the Bay mouth started to drop, although the front of 14.0-14.5$^{o}$C isotherm was still in the Bay (Figure 37c, right panel). The MBE front left the Bay mouth and moved westward to about 122.10 $^{o}$W on August 28 (Figure 37d, right panel). The offshore translation of MBE was evident from August 28 to 29 and the front had retreated back to about 122.25 $^{o}$W (Figure 37e, right panel). Figure 37e is very similar to Figure 36a, with the upwelling plume from Point Aňo Nuevo turning offshore at the mouth of the Bay. By August 31, the surface temperature over the area of MBE has dropped about 4$^{o}$C (Figure 37f, right panel). Without applying the hybrid data assimilation scheme, the NCOM free run fails to predict the above phenomena, especially for the temperature field (Figure 37, left panel).

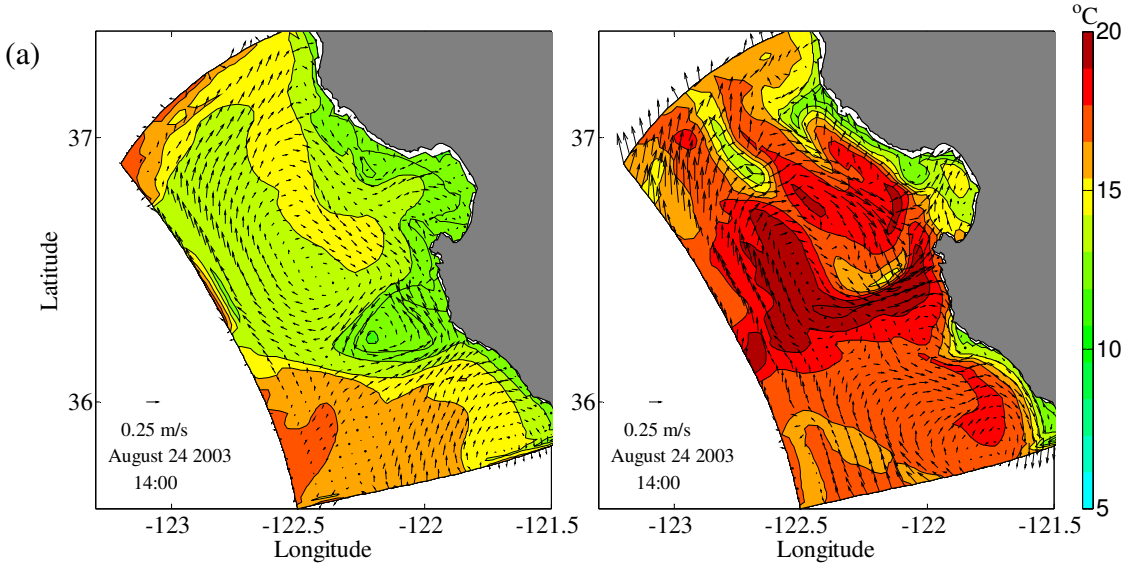


Figure 37. Time series of surface temperature and velocity fields from NCOM free run (left panel) and NCOM data assimilation run (right panel) from August 24-29, 2003.

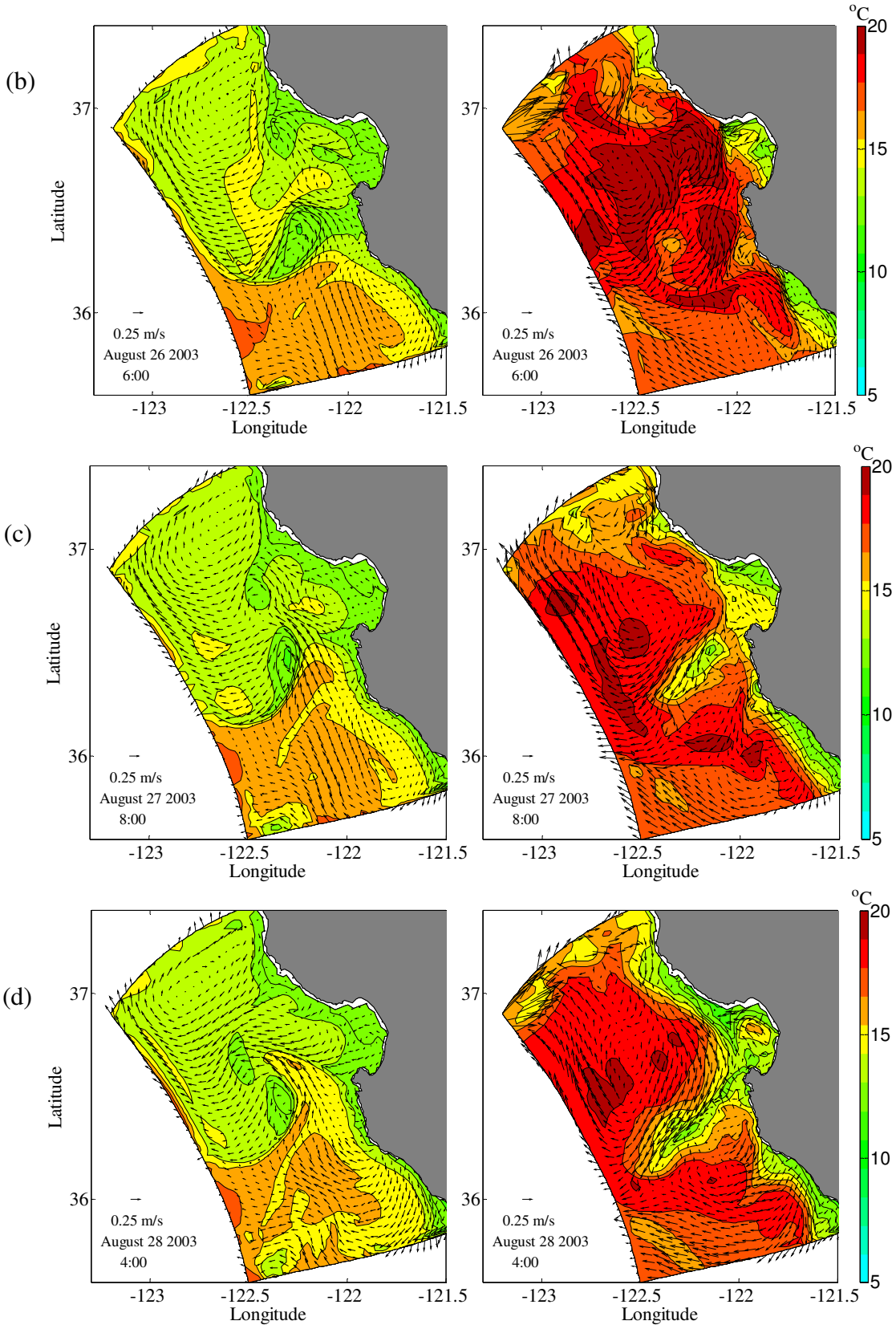


Figure 37. (continued).

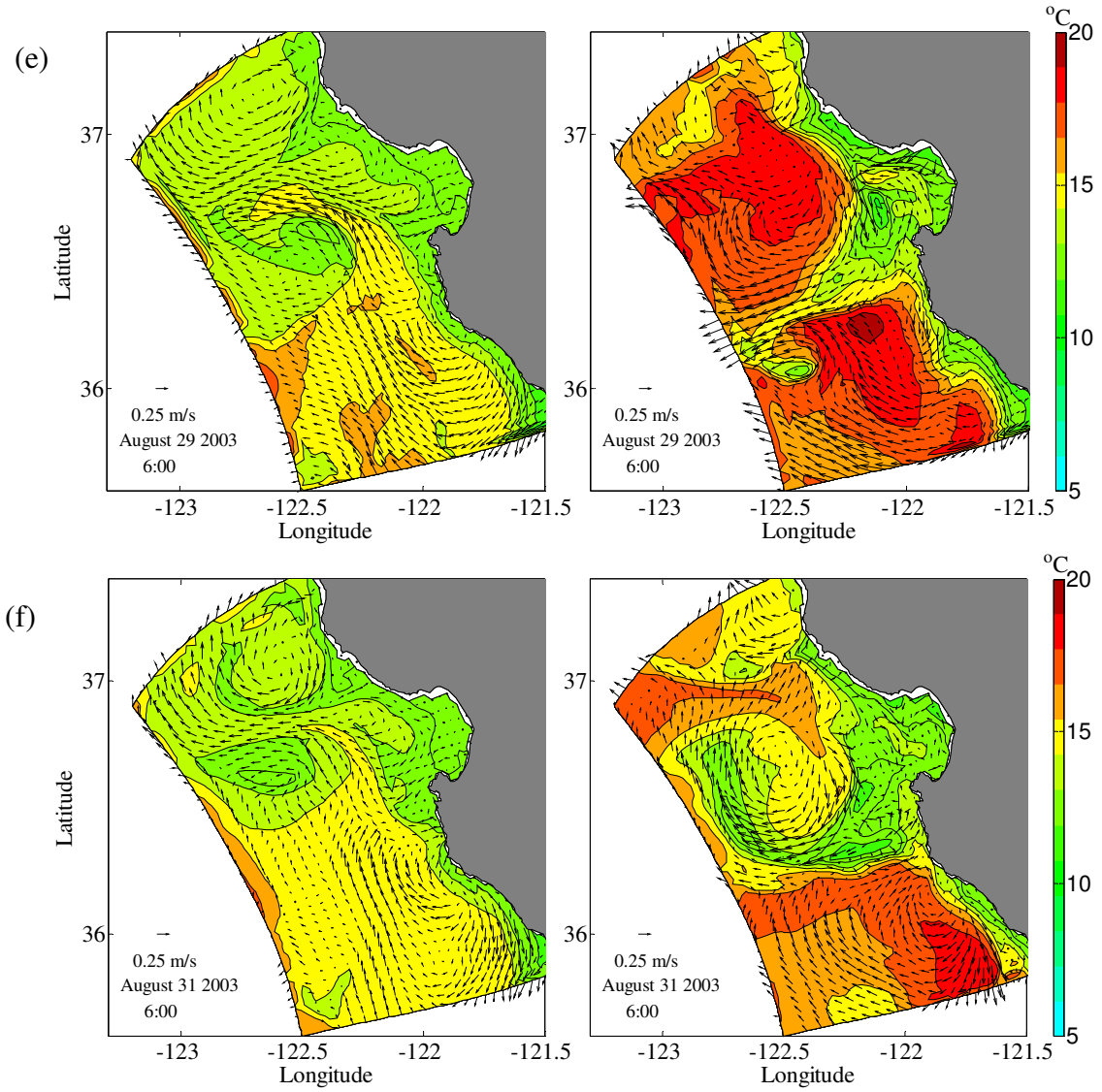


Figure 37 (continued).

From mooring observations obtained in 1991, Ramp *et al*. (1997) stated that the temperature at the M2 mooring location decreased more (about 0.9°C, from August 9 to 24) when the MBE translated offshore than it increased (0.5°C, from August 24 to September 8) when the MBE moved onshore (Figure 38). The time series of surface temperature at the M2 mooring location for data assimilation run 6 during our study period (August 2-31, 2003) is shown in Figure 39. From August 20 to 21 (when the wind relaxation period started), the surface temperature at the M2 mooring location increased

approximately 2.5°C. There is a sudden drop of temperature on August 22, caused by the passing by of a residual upwelling filament at the M2 mooring location (not shown). The high temperature (about 18°C) persisted about 7 days (August 23-30) and dropped rapidly to 14°C. Consistent with NCOM results in Fe and f (right panel), the dropping magnitude of surface temperature at the M2 mooring location is about 4°C. The pattern that the increasing magnitude of temperature (2.5°C) during relaxation events is smaller than the decreasing magnitude of temperature (4°C) during upwelling events is similar to the observation reported by Ramp *et al*. (1997) although the mooring temperature only rose by about 0.5°C and dropped by about 0.9°C in their case because their mooring level is at the depth of 416 m.

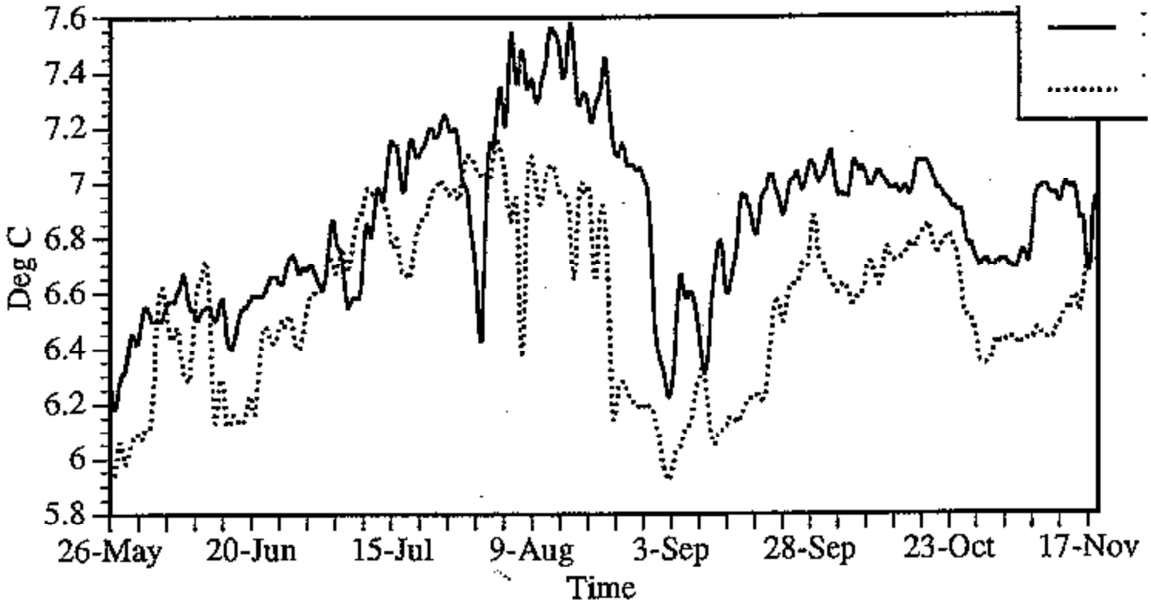


Figure 38. Mooring temperature obtained in 1991 (Ramp *et al*., 1997). Dotted line is mooring temperature at the M2 location.

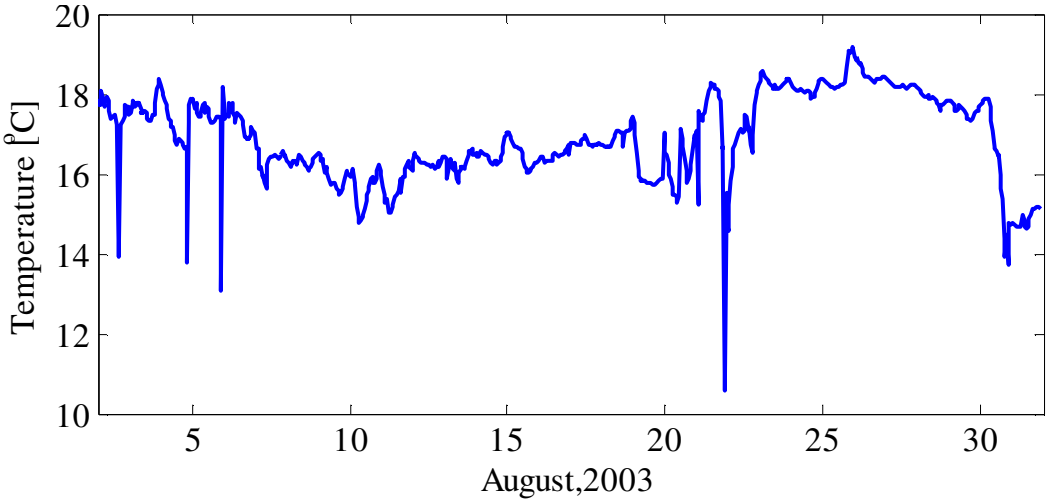


Figure 39. Surface temperature time series at the M2 mooring location for data assimilation run 6.

*b. Coastal Upwelling*

Local upwelling is another important physical phenomenon of interest in the Monterey Bay region (see section 2.5). Previous studies indicated that there exists two upwelling center in this area, one at Point Aňo Nuevo and the other at Point Sur (Figure 1). The upwelling filaments originating from these two points play an important role in affecting the surrounding local water properties (Tracy, 1990, Rosenfeld *et al*., 1994, Ramp *et al*., 1997, 2005).

Using aircraft data, Ramp *et al*. (2005) reconstructed the sea surface temperature from August 17 and 20 (upwelling events) in 2000 (Figure 40). On August 17, a well-defined cold upwelling filament originated from Point Aňo Nuevo and extended southeast to the Bay mouth (Figure 40a). This cold filament seperated into two branches during August 17 to 20. One branch flowed offshore and the other intruded into the Bay (Figure 40b). This is consistent with the bifurcated flow theory proposed by Rosenfeld *et al*. (1994).

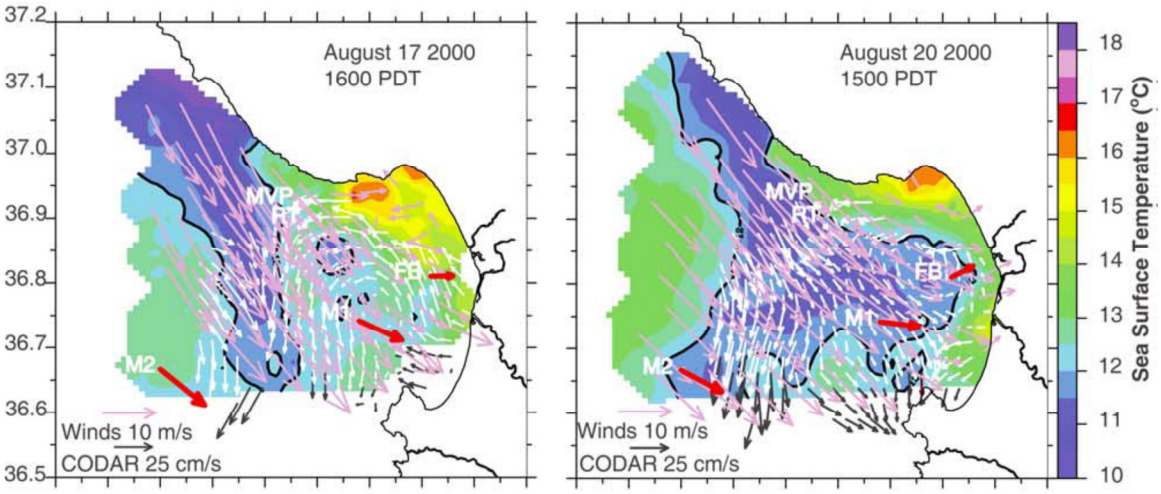


Figure 40. Sea surface temperatures measured by an infrared radiation pyrometer during upwelling events in 2000 (Ramp *et al*., 2005). Purple arrows indicate wind velocity. Black and white arrows represent sea surface velocity.

To compare with the observations from Ramp *et al*. (2005) (Figure 40), a time series of sea surface temperature and velocity maps derived from NCOM results are presented in Figure 41. Results from the NCOM free run (without data assimilation) are displayed on the left panel. Results from NCOM with the hybrid 3D-VAR scheme are showed on the right panel.

Similar to the results of Ramp *et al*., the upwelling cold filaments extended from Point Aňo Nuevo to the mouth of the Bay from August 11 to 12 (Figure 41a, b; right panel). The minimum temperature of the filament is also comparable with the results of Ramp *et al*. (approximately 11$^{o}$C). The upwelling filament showed the tendency to bifurcate at the mouth of the Bay on August 14 (Figure 41c, right panel). By noon of August 14, the bifurcation became evident (Figure 41d, right panel). As described in previous research, one branch of the filament flowed into the center of the Bay, and the other branch followed the MBE current and traveled offshore.

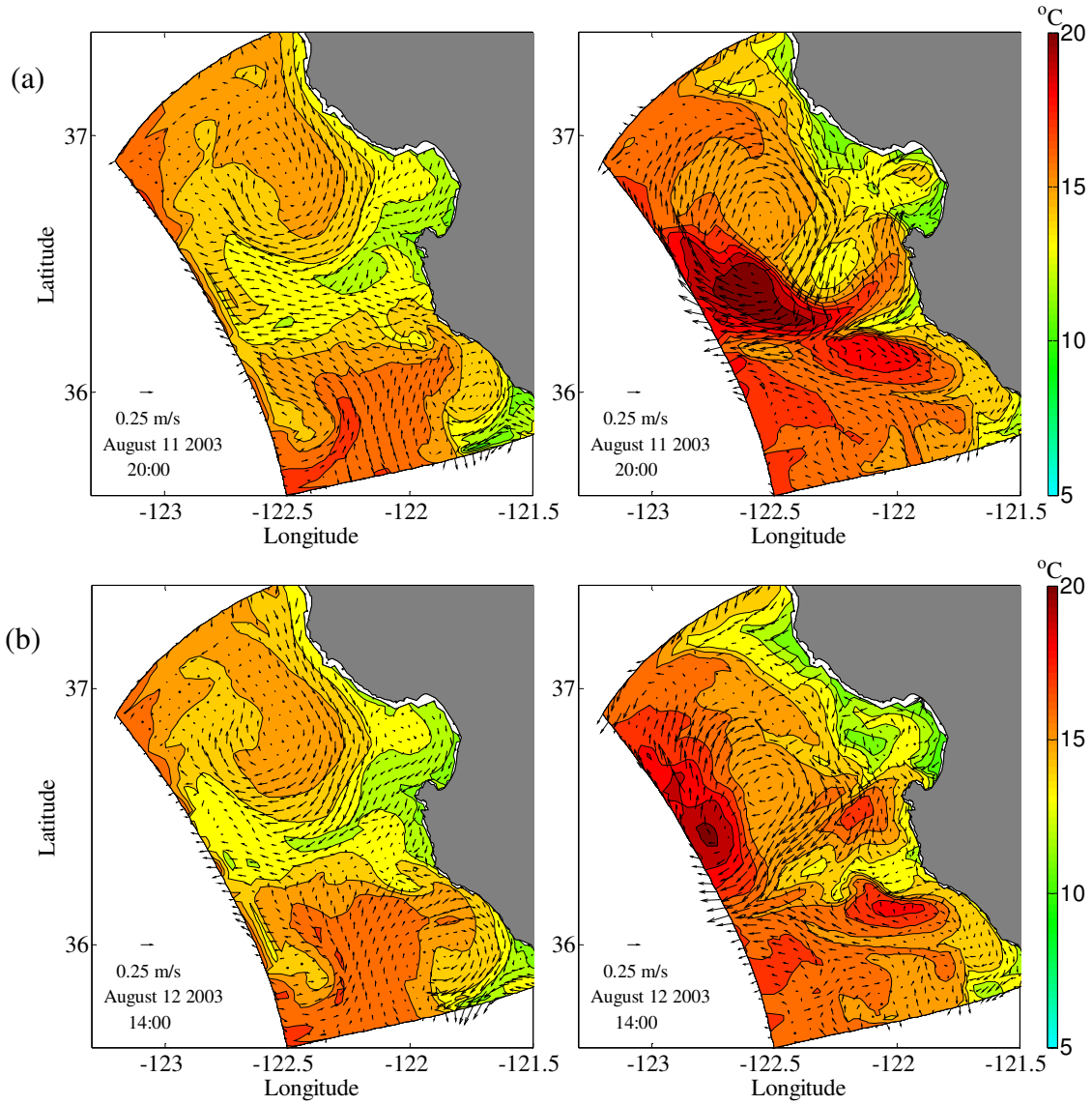


Figure 41. Time series of surface temperatures and velocity fields from the NCOM free run (left panel) and the NCOM data assimilation run (right panel) from August 11-14, 2003.

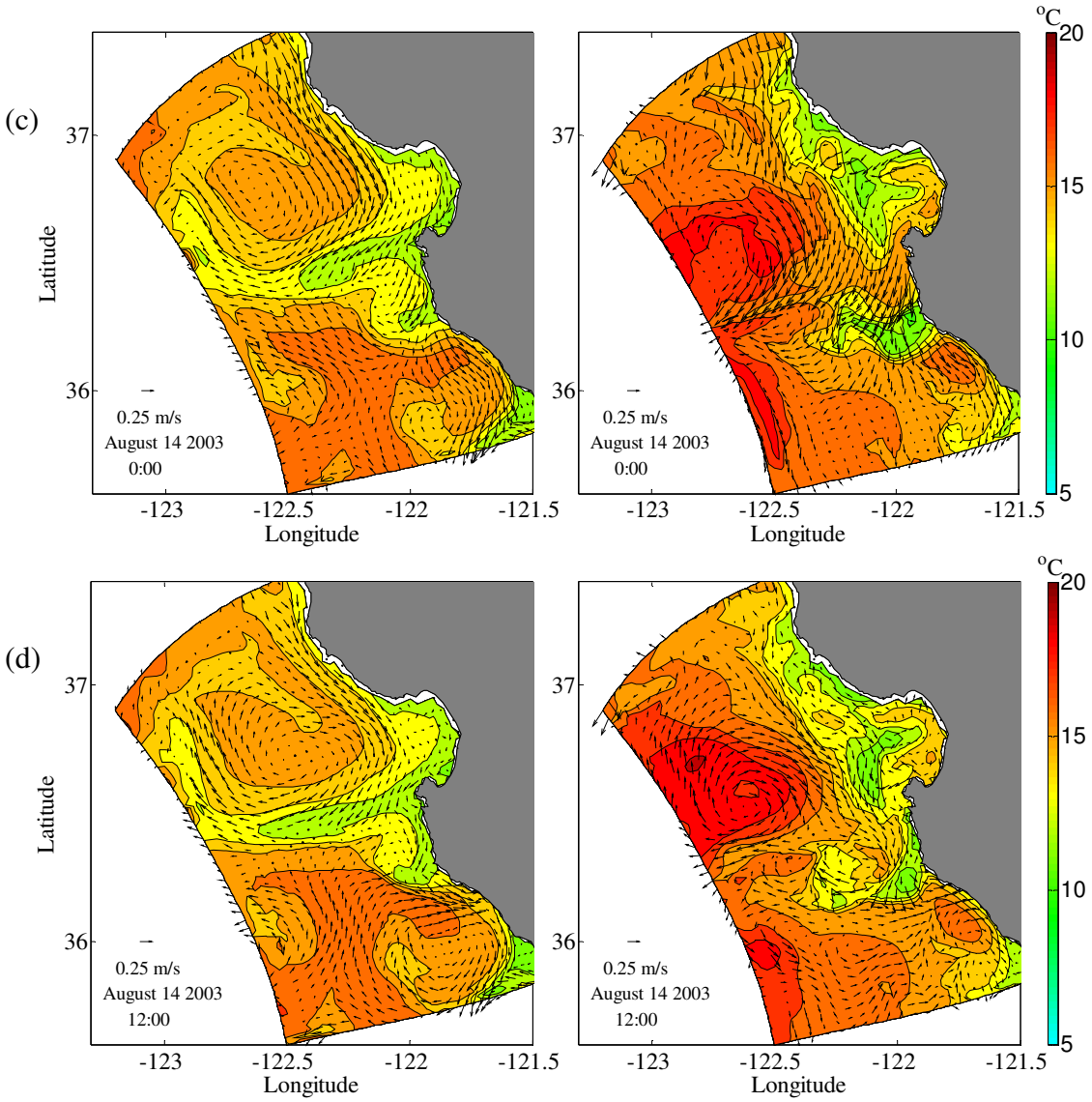


Figure 41. (continued).

The filament that originated from Point Sur was not as well-defined as the one coming from Point Aňo Nuevo during August 11-12 (Figure 41a, b; right panel). Nonetheless, the cold water that upwelled from Point Sur appeared to be broadening on August 14 (Figure 41c, d; right panel). The upwelling filament from Point Sur has a tendency to travel offshore, which is consistent with NOAA AVHRR satellite image from May 3, 1989 (upwelling period; Tisch *et al*., 1992; Figure 42).

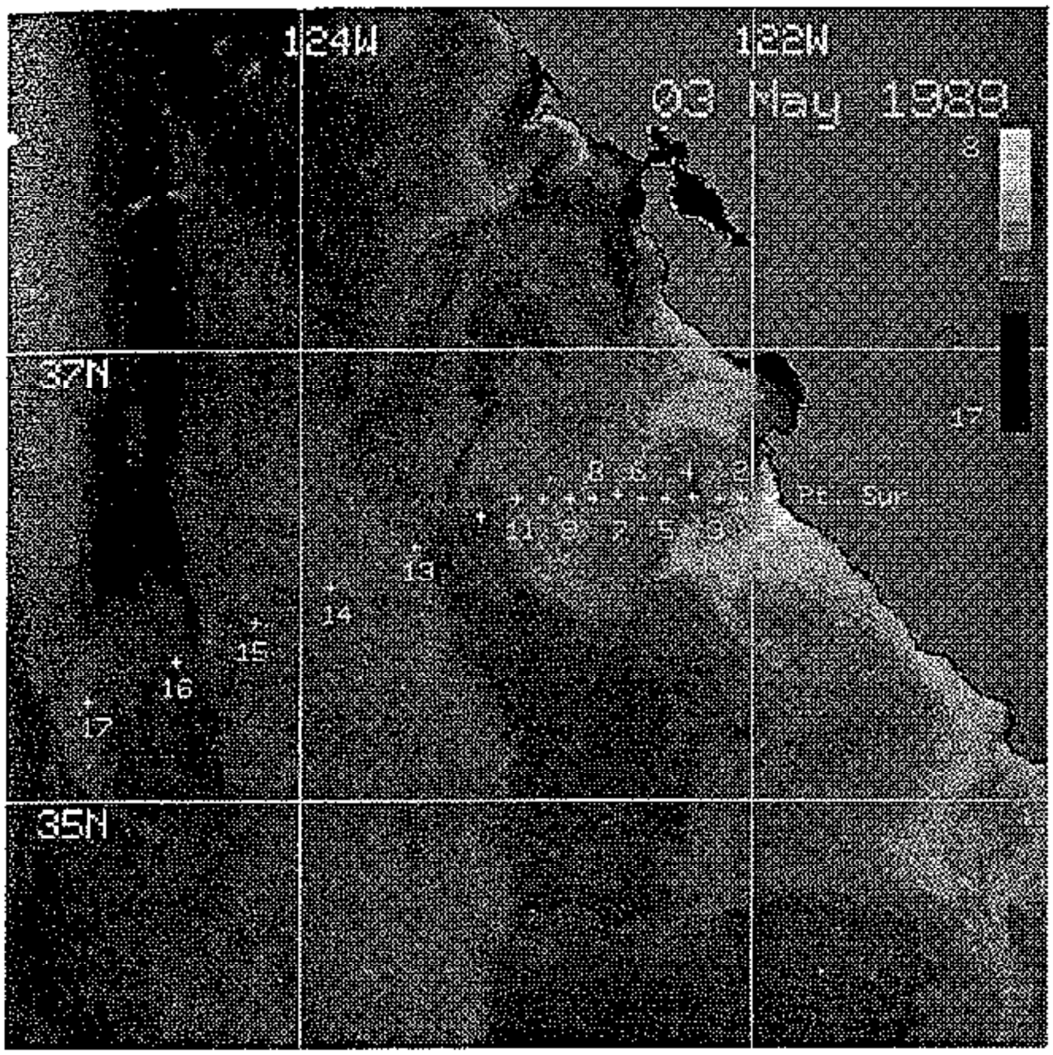


Figure 42. NOAA AVHRR satellite image on May 3, 1989 (Tisch *et al*., 1992).

On the SST maps from Ramp *et al*., there is a patch of warm water located in the north corner of the Bay (Figure 40). This area with high SST is often termed "upwelling shadow" (Graham, 1993; Graham and Largier, 1997). Both the NCOM free run and data assimilation run failed to reproduce this phenomenon during the upwelling events on August 11-14. This could be attributed to the lack of glider data in the north corner of the Bay (Figure 7).

*c. California Undercurrent (CUC)*

The coastal region off Point Sur is characterized by the existence of CUC during

both upwelling and relaxation periods. Although CUC was observed surfacing during some relaxation events, it is traditionally categorized as a subsurface current. Hence, a large-scale, spatially-continuous, horizontal observation for CUC is rare and difficult to accomplish. Instead, numerical model simulation for CUC was often preferred in previous studies. Ramp *et al*. (2005) simulated the salinity and current fields at the 100 m level during upwelling and relaxation events in August 2000 using hydro-dynamical ICON model (Figure 43). The subsurface current CUC carries salty water and flows poleward along the coast south of Point Sur during both upwelling and relaxation events. During upwelling event, however, CUC was relatively weak and couldn't reach Monterey Bay. CUC collided with CC and turned offshore near Point Sur during upwelling events on August 17-27 (Figure 43a, b and c). During relaxation events, CUC passed Point Sur flowing further north and eventually entered Monterey Bay, causing decreased salinity (due to the interaction between CC and CUC) in the Bay.

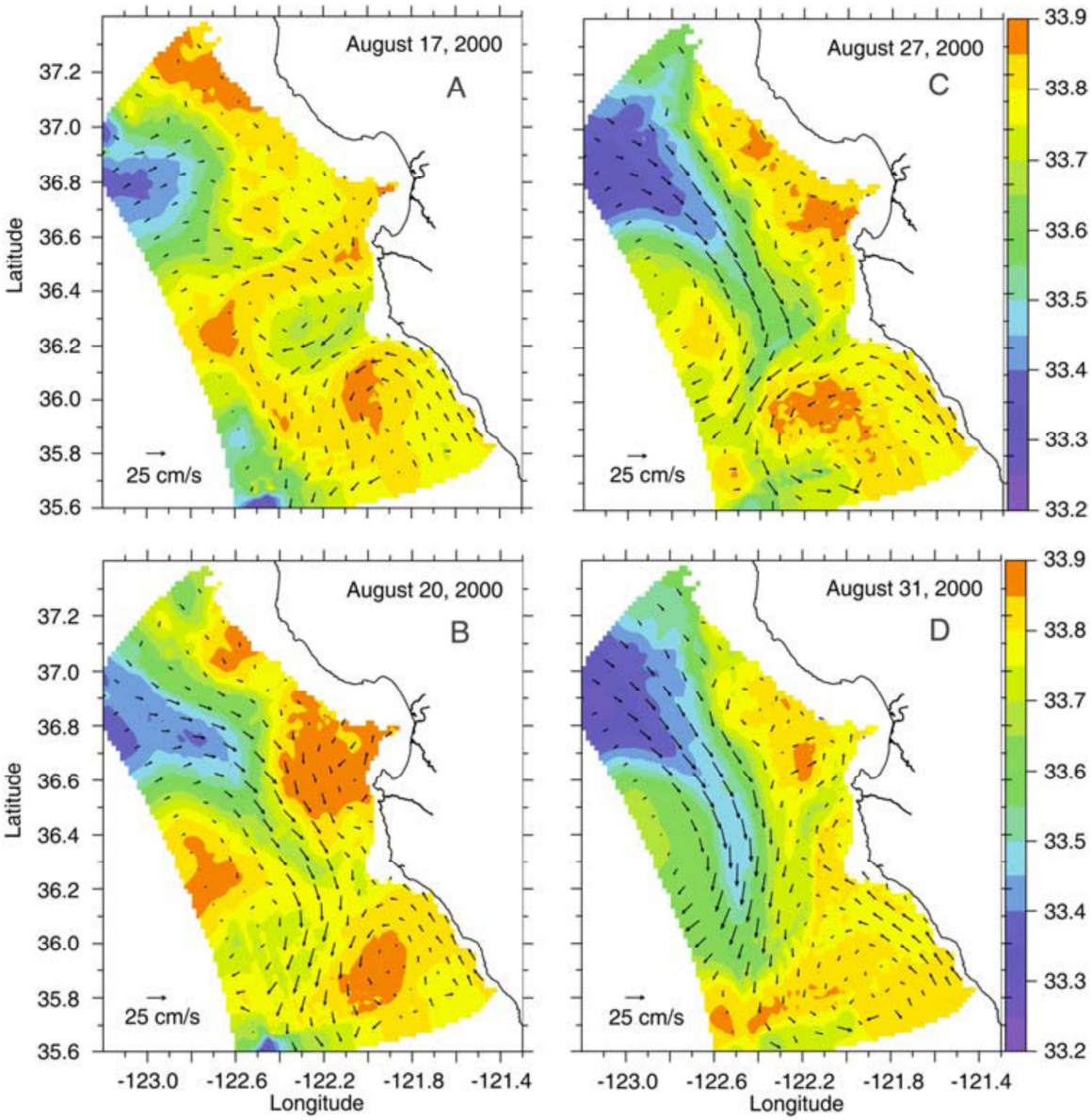


Figure 43. Salinity and velocity fields at 100 m from the ICON model during upwelling events (A, B) and relaxation events (C, D; Ramp *et al*., 2005).

Figure 44 shows typical horizontal structures for salinity and velocity fields at 100 m from NCOM results during upwelling and relaxation events. Similar to the results from Ramp *et al*. (2005), CUC existed during both upwelling and relaxation events (Figure 44a, b and c, right panel), although the velocity of CUC (about 0.1 m/s) is relatively weaker than their results (about 0.2 m/s) during upwelling period. A high salinity belt, which marks the track of CUC, was visible along the coast south of Point Sur. During upwelling

events on August 9 (Figure 44a) and August 17 (Figure 44b), CUC met intense CC and turned westward near Point Sur. There existed a current flowing from south of the model domain to about 36.2 $^{o}$N, which was absent from the results of Ramp *et al*. Given that this current also presents in the model free run (Figure 44a, b, left panel), this northward current might originate from the south open boundary of the model where the regional NCOM coupled with another large scale NCOM model. Whether this current really existed during August 2003 is difficult to verify without current data in this region. During relaxation event on August 21 (Figure 44c), part of the CUC merged into the CC and flowed offshore, and another part flowed northward and reached Monterey Bay. The salinity around the south part of the Bay also decreased due to the northward invasion of the CUC.

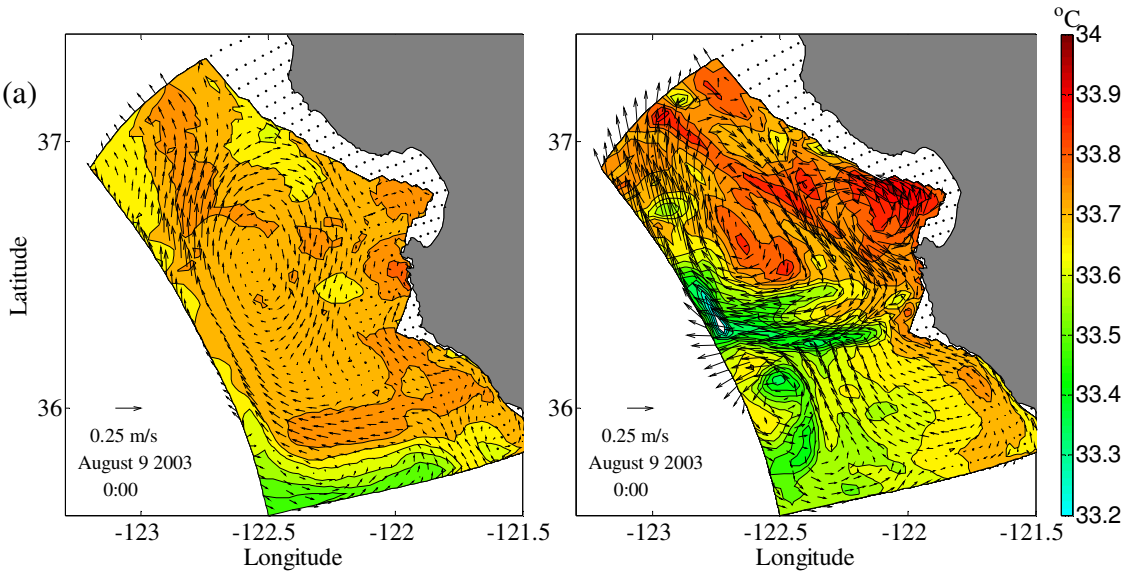


Figure 44: Salinity and velocity fields at 100 m from the NCOM free run (left panel) and the NCOM data assimilation run (right panel) during upwelling events on (a) August 9 and (b) August 17 and during relaxation events on (c) August 21.

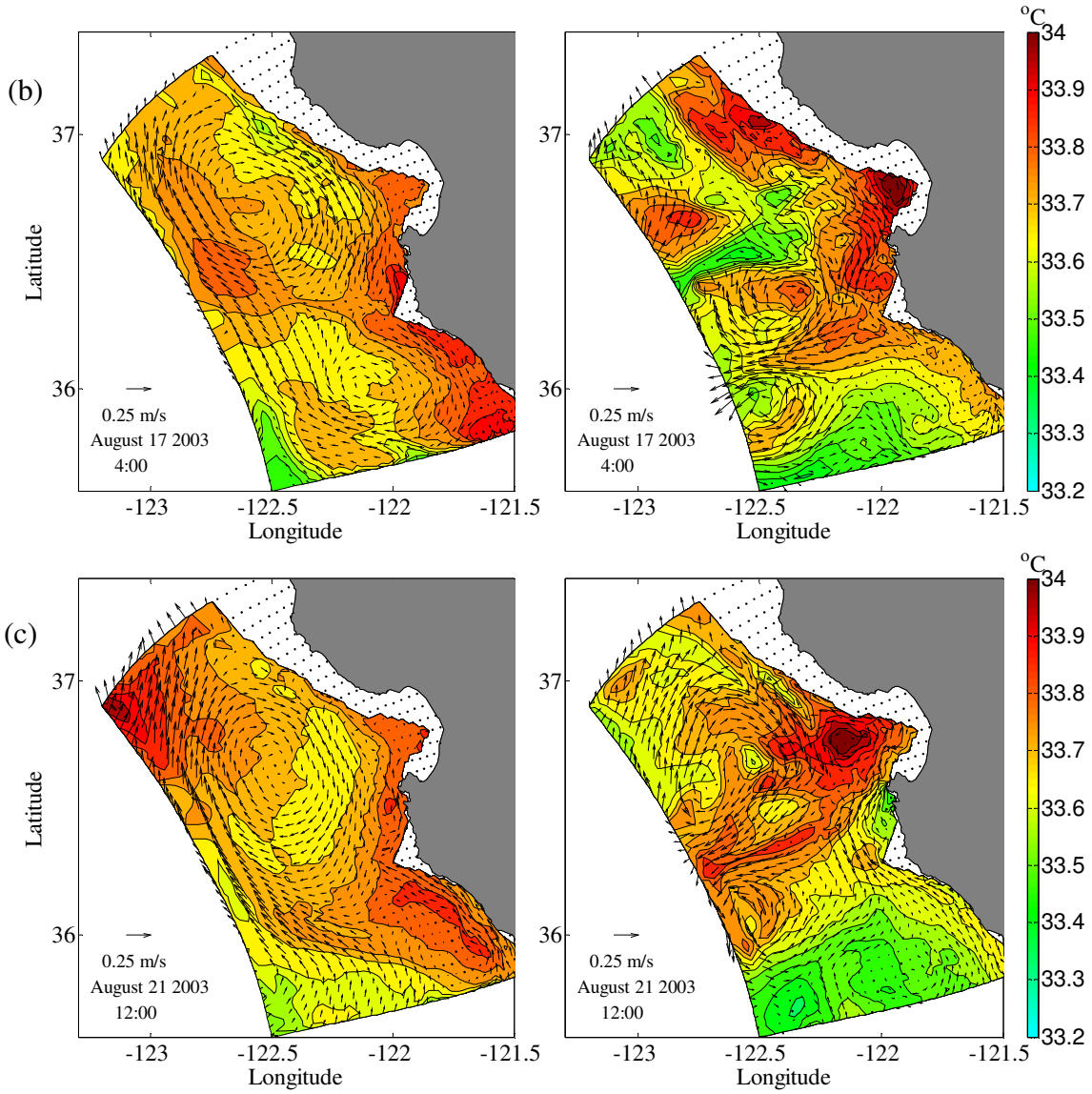


Figure 44. (continued).

Tisch *et al*. (1992) examined the variability of the alongshore currents along POST (Point Sur transect) using hydrographic data measured in 1988 and 1989 (Figure 45a). Figure 45 compares the vertical structure of the alongshore current between the results from Tisch *et al*. and results from NCOM with data assimilation. The velocity in Figure 45a was a geostrophic current calculated from temperature, salinity and pressure observations while our velocity results (Figure 45b) come from NCOM output. In Figure 45a, there exists a northward current with a core speed of 0.2 m/s on the shelf and slope

at about 200 dbar (close to 200 m) where the CUC is active. The current of the transect turns southward with low speed (less than or close to 0.1 m/s) further offshore (40 km to 80 km away from Point Sur). The results from NCOM (Figure 45b) also show the CUC, occupying the shelf and slope although the magnitude of the northward flow is much weaker (less than 0.15 m/s). The southward flow located 30 – 50 km away from Point Sur is strong (core speed larger than 0.4 m/s). The northward current at the west (60 - 80 km) is consistent with northward flow originating from the southern open boundary in Fa (right panel). Overall, the vertical structure of Figure 45a and Figure 45b is similar.

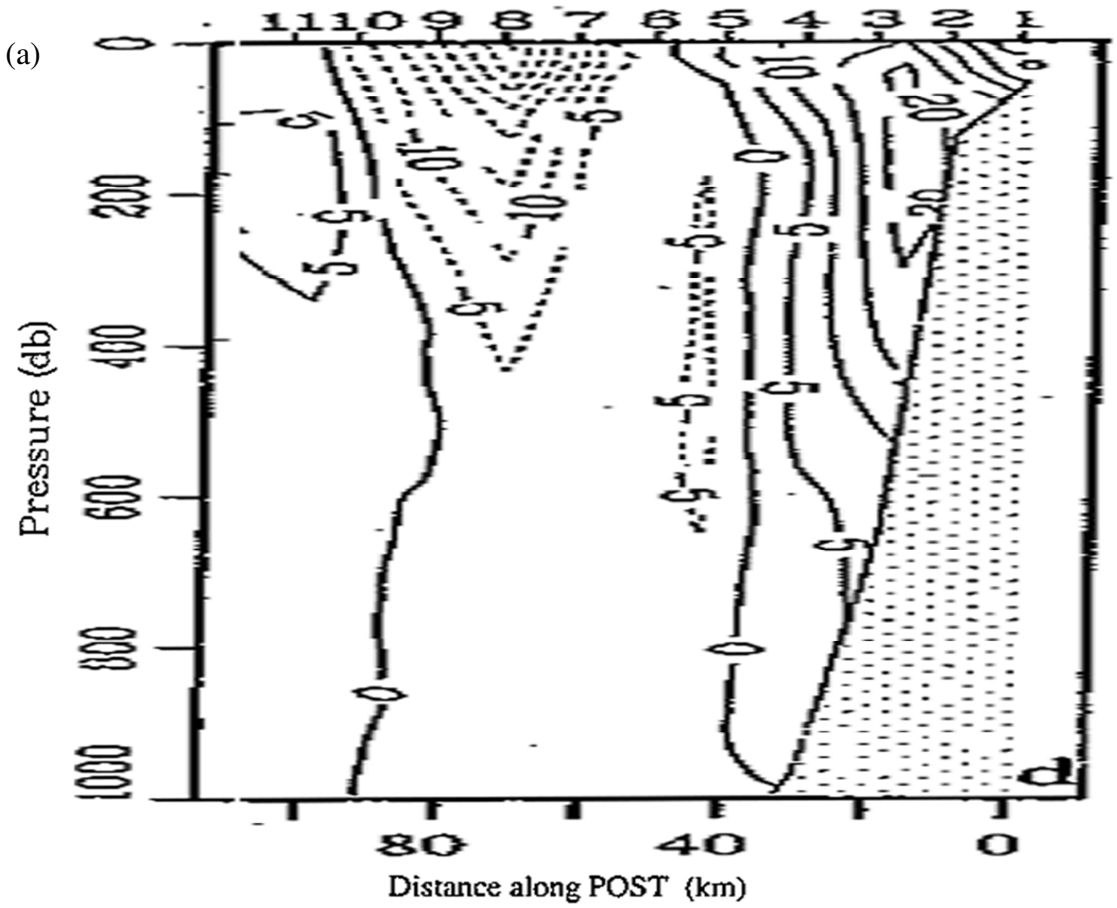


Figure 45. (a) Geostrophic current along the POST during upwelling events in May, 1989. Dotted lines indicate southward velocity and solid lines represent northward velocity. (b) Current along the same transect from NCOM data assimilation run during upwelling events on August 17, 2003. Negative numbers indicate southward velocity and positive numbers represent northward velocity.

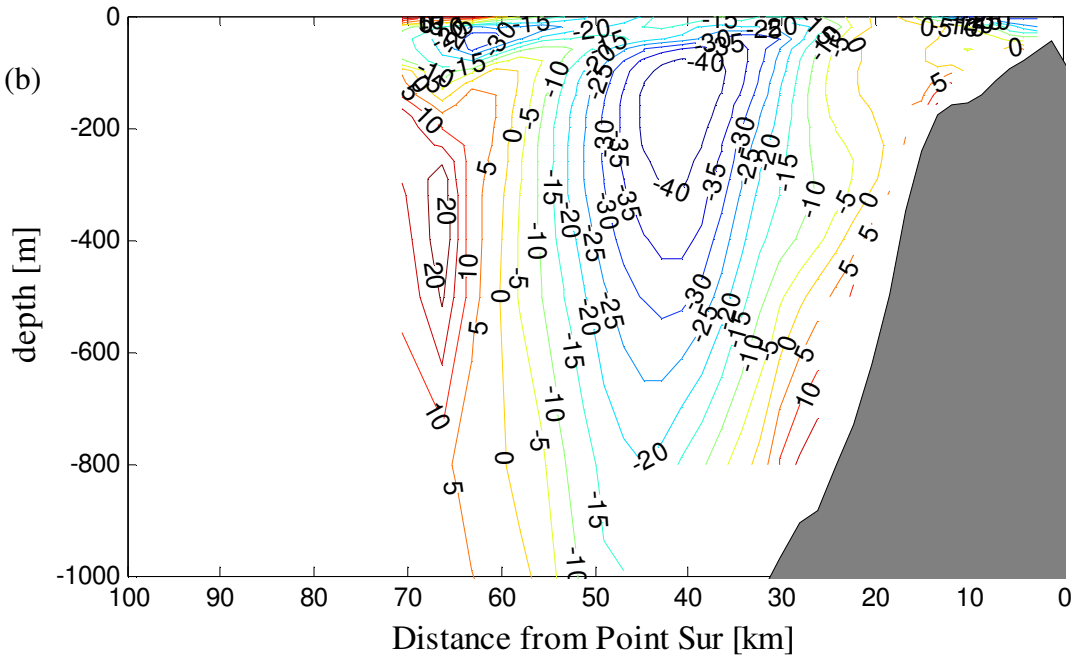


Figure 45. (continued)

The vertical variation of the alongshore current from Tisch *et al*. during relaxation events in 1988 (August) is compared with NCOM results in Figure 46. Both figures show large vertical areas of northward current. The CUC in Figure 46a has a tendency to surface above the shelf. Core speed of CUC at this time reached 0.35 m/s. The northward velocity reduces to less than 0.05 m/s below 600 dbar. The core of CUC in Figure 46b remains on the shelf with a core speed of 0.30 m/s. Most of the section has a northward speed of 0.00 – 0.10 m/s except for the CUC core on the shelf and west boundary. There exist a southward CC current from the surface down to 200 m at 60 – 70 km away from Point Sur in both Figure 46a and 46b.

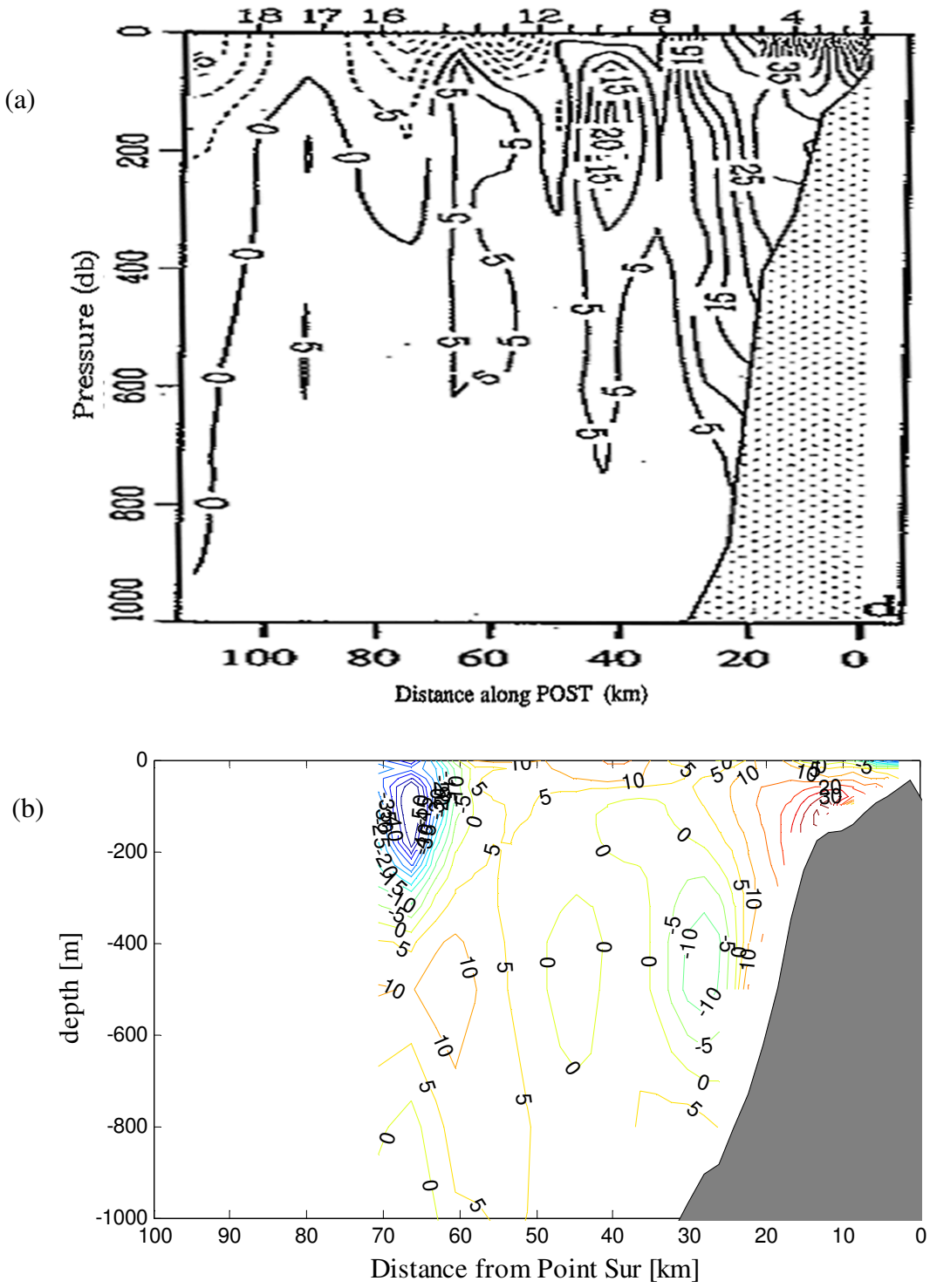


Figure 46. (a) Geostrophic current along the POST during relaxation events in August, 1988. Dotted lines indicate southward velocity and solid lines represent northward velocity. (b) Current along the same transect from NCOM data assimilation run during relaxation events on August 21, 2003. Negative numbers indicate southward velocity and positive numbers represent northward velocity.

# CHAPTER VI

## SUMMARY

A new data assimilation system combining hybrid 3D-VAR BEC scheme and NCOM was applied to the Monterey Bay area to assimilate temperature and salinity glider data collected in August 2003.

In twin data experiments, the performance of traditional 3D-VAR scheme and hybrid 3D-VAR scheme were evaluated with respect to the "true" model state. Overall, both assimilation runs at M1 location matched the "true" model state except for August 23-27, a transition period from relaxation to upwelling events. During this transition period, the traditional 3D-VAR scheme overestimated temperature and underestimated salinity while the results from hybrid scheme were in better agreement with the "true" model state. M2 location is influenced by the MBE and is dynamically more complicated than M1, which increases the difficulties for data assimilation. As a result, deviation of temperature and salinity from the "true" model state could be observed from August 18 through August 31 for both assimilation schemes. Nonetheless, the performance of hybrid scheme is still better than traditional scheme in M2 location according to bias and RMS error estimation.

Both assimilation runs were capable of predicting subsurface structure of the "true" model state during twin data experiments. However, the temperature and salinity obtained from the traditional scheme seemed to deviate from the "true" model state near the relaxation events and at the end of August. The shallowing and deepening of the thermocline and halocline in both M1 and M2 locations appeared to be more accurate in the assimilation run with the hybrid scheme than in the one with the traditional scheme.

The assimilation skill is tested by calculating the normalized distance between the assimilation results and the "true" states in state space. Both normalized temperature and salinity error tend to grow with time in both assimilation runs, which is caused by the difference of the "true" states and the first guess. The hybrid 3D-VAR scheme reduced both temperature and salinity errors comparing with the traditional 3D-VAR scheme. Although there is no velocity data assimilation in the experiments, the change of temperature and salinity field originated from the "bogus" data assimilation also had a positive impact to the velocity fields.

In real data experiment I, solutions from the model free run, the assimilation run with traditional 3D-VAR scheme and the assimilation run with FTW hybrid scheme were compared. Compared with the model free run, both assimilation runs improved model results significantly. During the transition period from relaxation to upwelling events, however, the traditional 3D-VAR scheme overestimated temperature and underestimated salinity at M1 location, which is similar to the results obtained in twin data experiments. This indicates instability of the traditional assimilation scheme during a dynamically complicated transition period. The hybrid scheme successfully assimilated glider data during this period. The performance of both assimilation schemes at M2 location was not as satisfactory as in M1 location, but the hybrid scheme still showed more improvement than the traditional scheme.

Both assimilation runs are capable of predicting subsurface temperature and salinity structures compared with model free run. Overestimation of near surface temperature can be observed in both assimilation runs, which might be caused by overestimation of SWR in COMAPS (Shulman *et al.*, 2009). Assimilation runs also overestimated subsurface

salinity especially during relaxation events, but the results are acceptable considering the narrow range of salinity variations in the region. Towards the end of August, the thermocline predicted by both assimilation schemes showed false elevation at M2 location. False elevation of halocline in the results from both assimilation runs was also observed. A combination of lack of glider data in deep water and complex dynamics at this location could be the cause of these errors.

The assimilation skill in real data experiments is tested by calculating the normalized distance between the assimilation results and observations at the mooring locations. The assimilation run with traditional 3D-VAR scheme showed loss of skill in both upwelling and relaxation events, especially for salinity results. The performance of the hybrid scheme generally exceeded the traditional scheme. The improvement of assimilation not only showed in normalized temperature and salinity error, but also in normalized velocity error, even without the involvement of velocity data assimilation.

Real data experiment II was concentrated on incorporating the FTW ensemble into the hybrid scheme. The results from the assimilation run with the full ensemble and the assimilation run with the FTW ensemble have shown that implementation of the FTW ensemble in the hybrid 3D-VAR scheme is beneficial, as it improves the forecast skill of the assimilation system and is cheaper computationally. Improvement of the forecast skill with a smaller ensemble may seem to be an unexpected result because the full ensemble contains the members of the FTW ensemble. However, the Bayesian information criterion used for selection of the flow-dependent part of the BEC selects the most persistent eigenvectors of the sample covariance matrix, which do not describe transient events, and, therefore, do not support the forecast skill of the assimilation system on short

time scales. Employing a smaller ensemble may improve the situation.

To test whether the hybrid 3D-VAR data assimilation system is able to reproduce major dynamical features of the Monterey Bay region, the results from NCOM model free run and NCOM data assimilation run with hybrid scheme were presented. Since there is not enough data reflecting the dynamics of the region during the time of interest (August 2003), the results of two model runs were compared with historical data during similar upwelling or relaxation periods. Comparisons have shown that NCOM combining with the hybrid 3D-VAR system was capable of reproducing major dynamical features, including onshore-offshore translation of the MBE during upwelling and relaxation events, coastal upwelling at Point Aňo Nuevo and Point Sur, the track of respective upwelling filaments, the appearance of the CUC during upwelling and relaxation events, and the interaction between the CUC and CC.

Future work involves further testing and modifying the hybrid scheme in regional assimilation experiments involving glider data. For example, loss of the forecast skill during transition from upwelling to relaxation, or vice versa, needs to be addressed. Velocity data assimilation can be important in improving NCOM model results and might be incorporated in future studies.

# APPENDIX

## Modeling Static BEC

The major idea is to model the resulting action of the BEC operator on a vector x by integrating the corresponding diffusion equation:

$$\frac{\partial \mathbf{x}}{\partial t} = \mathbf{D}\mathbf{x} = \frac{1}{2}\nabla \nu \nabla \mathbf{x} \tag{A.1}$$

for a certain "time period" τ. In equation (A.1) $\nu$ is the diffusion tensor represented by 3×3 positive-definite matrices, with elements depending on the coordinates **x** in physical space. The eigenvalues $\lambda_i^2 (i = 1,2,3)$ of $\nu$ are all positive.

The Gaussian BEC operator B is the propagator of the diffusion equation:

$$\mathbf{B}_0 = \exp(\tau \mathbf{D}) = \exp(\frac{1}{2}\tau \nabla \nu \nabla) \tag{A.2}.$$

Expression (A.2) shows that in the coordinate system spanned by $\boldsymbol{e}_{\mathrm{k}}$ eigenfunctions of $\mathbf{B}_0$ coincide with those of the Laplacian. The eigenvalues of $\mathbf{B}_0$ (detail of the deduction is showed at the end of Appendix)

$$\Lambda_k = \exp\left[\frac{1}{2}\left(\lambda_1^2 k_1^2 + \lambda_2^2 k_2^2 + \lambda_3^2 k_3^2\right)\right] \tag{A.3}$$

exhibit a larger attenuation at large wave number $\boldsymbol{k} = \{k_1, k_2, k_3\}$ , forming the Gaussian-shaped spectrum.

The inverse Fourier transform of (A.3) gives the correlation function

$$C(x) = \exp\left[-\frac{1}{2}\left(\frac{x_1^2}{\lambda_1^2} + \frac{x_2^2}{\lambda_2^2} + \frac{x_3^2}{\lambda_3^2}\right)\right] \tag{A.4}$$

indicating that the eigenvalues of $\nu$ are proportional to the squares of the respective decorrelation scale $\rho$ (here $\rho$ is the scale of $x_i$ ):

$$\lambda_i^2 \sim \rho^2$$

In homogeneous case, the decorrelation scales are defined locally in a similar manner whereas the "integration time" τ plays the role of a global scaling parameter for the distribution of $\rho^2(x)$.

In application, the Gaussian BEC operator (A.2) is usually represented by integrating with an explicit time-stepping scheme, $\mathbf{x}^{t+\delta t} = \mathbf{x}^t + \delta t \mathbf{D}\mathbf{x}^t$, such that the result of multiplication by $\mathbf{B}_0$ is:

$$\mathbf{x}^\tau = \mathbf{B}\mathbf{x} = \left[\mathbf{I} + \frac{\tau\mathbf{D}}{n}\right]^n \mathbf{x} = \mathbf{exp}(\tau\mathbf{D})\mathbf{x} \approx \exp(\rho^2\mathbf{D})\mathbf{x} \qquad \text{(A.5)}$$

where $\mathbf{I}$ is the identity operator and $n = \tau/\delta t$ is the total number of "time steps." Expression (A.5) shows that the Gaussian BEC model is, in fact, numerically a high-order polynomial in the diffusion operator **D**.

Consider the following form of the inverse BEC

$$\mathbf{B_0^{-1}} = (\mathbf{I} - \frac{\tau\mathbf{D}}{m})^m \qquad \text{(A.6)}$$

whose inverse approximates the Gaussian BEC:

$$\mathbf{B_0} = (\mathbf{I} - \frac{\tau\mathbf{D}}{m})^{-m} \approx \exp(\tau\mathbf{D}) \qquad \text{(A.7)}$$

The BEC operator in (A.7) can be implemented numerically in two ways:

$$\mathbf{B_0} = \left[(\mathbf{I} - \frac{\tau\mathbf{D}}{m})^{-1}\right]^m = \left[(\mathbf{I} - \frac{\tau\mathbf{D}}{m})^m\right]^{-1} \qquad \text{(A.8)}$$

The first method requires m inversion of $\mathbf{I} - \frac{\tau\mathbf{D}}{m}$, and this approach can be interpreted as integration of diffusion equation by an implicit scheme with the "time step" $\tau/m$. The

second method involves only one inversion of the matrix whose condition number is $c^m$, where $c = cond(\mathbf{I} - \frac{\tau \mathbf{D}}{m})$.

---

What are the Eigenvalues of $\mathbf{B}_0$?

In the equation $\mathbf{B}_0 = \exp(\tau \mathbf{D}) = \exp(\frac{1}{2}\tau \nabla \nu \nabla)$, $\nabla \nu \nabla$ is a matrix with dimension M (state vector dimension). In homogeneous case, define $\nu = \begin{vmatrix} \lambda_1^2 & 0 & 0 \\ 0 & \lambda_1^2 & 0 \\ 0 & 0 & \lambda_1^2 \end{vmatrix}$, thus:

$$\nabla \nu \nabla = \nu \nabla \cdot \nabla = \nu \Delta$$

The eigen vector of $\nu\Delta$ is $\exp\left[ i(\vec{k} \cdot \vec{x}) \right] = \exp\left[ i(k_1 x_1 + k_2 x_2 + k_3 x_3) \right]$. To prove this, consider the real part $\sin(k_1 x_1 + k_2 x_2 + k_3 x_3)$

$$\begin{aligned} \nu\Delta \sin(\vec{k} \cdot \vec{x}) &= (\lambda_1^2 \frac{\partial^2}{\partial x_1^2} + \lambda_2^2 \frac{\partial^2}{\partial x_2^2} + \lambda_3^2 \frac{\partial^2}{\partial x_3^2}) \sin(k_1 x_1 + k_2 x_2 + k_3 x_3) \\ &= -(\lambda_1^2 k_1^2 + \lambda_2^2 k_2^2 + \lambda_3^2 k_3^2) \sin(k_1 x_1 + k_2 x_2 + k_3 x_3) \end{aligned}$$

Similarly for the imaginary part:

$$\begin{aligned} &\nu\Delta(i \cos(\vec{k} \cdot \vec{x})) = \\ &-(\lambda_1^2 k_1^2 + \lambda_2^2 k_2^2 + \lambda_3^2 k_3^2)\left[ i \cos(k_1 x_1 + k_2 x_2 + k_3 x_3) \right] \end{aligned}$$

For the whole part:

$$\nu\Delta \exp\left[ i(k_1 x_1 + k_2 x_2 + k_3 x_3) \right] = -(\lambda_1^2 k_1^2 + \lambda_2^2 k_2^2 + \lambda_3^2 k_3^2) \exp\left[ i(k_1 x_1 + k_2 x_2 + k_3 x_3) \right]$$

Thus, the eigen value of $\nu\Delta$ (Laplacian) is $-(\lambda_1^2 k_1^2 + \lambda_2^2 k_2^2 + \lambda_3^2 k_3^2)$.

On the other hand:

$$\mathbf{B_0} \approx \exp(\frac{1}{2}\nabla\nu\nabla)$$
$$\approx \exp(\frac{1}{2}\nu\Delta)$$
$$\approx E + \frac{\nu}{2\cdot 1!}\Delta + \frac{\nu^2}{2^2\cdot 2!}\Delta^2 + ...$$

The eigen value of $\nu^2\Delta^2$ is $\left[-(\lambda_1^2k_1^2 + \lambda_2^2k_2^2 + \lambda_3^2k_3^2)\right]^2$.

Thus, the eigen value of $\mathbf{B_0} \approx E + \frac{\nu}{2\cdot 1!}\Delta + \frac{\nu^2}{2^2\cdot 2!}\Delta^2 + ...$ is

$$\Lambda_k = 1 + \frac{1}{1!}\left[-\frac{1}{2}(\lambda_1^2k_1^2 + \lambda_2^2k_2^2 + \lambda_3^2k_3^2)\right] + \frac{1}{2!}\left[-\frac{1}{2}(\lambda_1^2k_1^2 + \lambda_2^2k_2^2 + \lambda_3^2k_3^2)\right]^2 + ...$$
$$= \exp\left[-\frac{1}{2}(\lambda_1^2k_1^2 + \lambda_2^2k_2^2 + \lambda_3^2k_3^2)\right]$$

---

# REFERENCES

Batteen, M. L. 1997. Wind-forced modeling studies of currents, meanders, and eddies in the California Current system. J. Geophys. Res., *102*, 985-1010.

Batteen, M. L. and P. W. Vance. 1998. Modeling studies of the effects of wind forcing and thermohaline gradients on the California Current System. Deep-Sea Res. Pt. II, *45*, 1507-1556.

Batteen, M. L., N. J. Cipriano and J. T. Monroe. 2003. A large-scale seasonal modeling study of the California Current System. J. Oceanogr., *59*, 545-562.

Batteen, M. L., C. A. Collins, C. R. Gunderson and C. S. Nelson. 1995. The Effect of Salinity on Density in the California Current System. J. Geophys. Res., *100*, 8733-8749.

Bennett, A. F. 1992. Inverse methods in physical oceanography. Cambridge University Press, Cambridge, 346 pp.

Blencoe, D. G. 2001. Impact of high resolution wind fields on coastal ocean models, Naval Postgraduate School Monterey, CA, 85 pp.

Blumberg, A. F. and G. L. Mellor. 1987. A description of a three-dimensional coastal ocean circulation model, *in* Coastal and Estuarine Sciences 4: Three Dimensional Coastal Models, N. S. Heaps, ed., AGU, 1–16.

Brasseur, P. and J. Verron. 2006. The SEEK filter method for data assimilation in oceanography: a synthesis. Ocean Dynam., *56*, 650-661.

Breaker, L. C. and C. N. K. Mooers. 1986. Oceanic variability off the central California coast. Prog. Oceanogr., *17*, 61-135.

Breaker, L. C. and W. W. Broenkow. 1994. The Circulation of Monterey Bay and

Related Processes. Oceanogr. Mar. Biol., *32*, 1-64.

Buehner, M. 2005. Ensemble derived stationary and flow dependent background error covariances: evaluation in a quasi operational NWP setting. Q. J. Roy. Meteorol. Soc., *131*, 1013-1043.

Chelton, D. 1984. Seasonal variability of alongshore geostrophic velocity off central California. J. Geophys. Res., *89*, 3473-3486.

Chou, Y. 1970. Statistical analysis. Holt Rinehart and Winston, New York, 165 pp.

Cohn, S. E., A. da Silva, J. Guo, M. Sienkiewicz and D. Lamich. 1998. Assessing the Effects of Data Selection with the DAO Physical-Space Statistical Analysis System. Mon. Weather Rev., *126*, 2913-2926.

Courtier, P., E. Andersson, W. Heckley, D. Vasiljevic, M. Hamrud, A. Hollingsworth, F. Rabier, M. Fisher and J. Pailleux. 1998. The ECMWF implementation of three-dimensional variational assimilation (3D-Var). I: Formulation. Q. J. Roy. Meteorol. Soc., *124*, 1783-1807.

Cummings, J. A. 2005. Operational multivariate ocean data assimilation. Q. J. Roy. Meteorol. Soc., *131*, 3583-3604.

Davis, R. 1985. Drifter observations of coastal surface currents during CODE: The method and descriptive view. J. Geophys. Res., *90*, 4741-4755.

De Mey, P. and M. Benkiran. 2002. A multivariate reduced-order optimal interpolation method and its application to the Mediterranean basin-scale circulation, *in* Ocean Forecasting, Conceptual Basis and Applications, N. Pinardi and J. Woods, ed., Springer-Verlag, 281-306.

Derber, J. and A. Rosati. 1989. A global oceanic data assimilation system. J. Phys.

Oceanogr., *19*, 1333-1347.

Dobricic, S. and N. Pinardi. 2008. An oceanographic three-dimensional variational data assimilation scheme. Ocean Model., *22*, 89-105.

Etherton, B. J. and C. H. Bishop. 2004. Resilience of hybrid ensemble/3DVAR analysis schemes to model error and ensemble covariance error. Mon. Weather Rev., *132*, 1065-1080.

Evensen, G. 1994. Sequential data assimilation with a nonlinear quasi-geostrophic model using Monte Carlo methods to forecast error statistics. J. Geophys. Res., *99*, 10143-10162.

Evensen, G. 2003. The ensemble Kalman filter: Theoretical formulation and practical implementation. Ocean Dynam., *53*, 343-367.

Gandin, L. 1965. Objective analysis of meteorological fields. Israel program for scientific translations, Springfield, Illinois, 242 pp.

Graham, W. 1993. Spatio-temporal scale assessment of an “upwelling shadow” in northern Monterey Bay, California. Estuaries and Coasts, *16*, 83-91.

Graham, W. M. and J. L. Largier. 1997. Upwelling shadows as nearshore retention sites: The example of northern Monterey Bay. Cont. Shelf Res., *17*, 509-532.

Haidvogel, D. B., A. Beckmann and K. S. Hedström. 1991. Dynamical simulations of filament formation and evolution in the coastal transition zone. J. Geophys. Res., *96*, 15017-15040.

Haley Jr, P. J., P. F. J. Lermusiaux, A. R. Robinson, W. G. Leslie, O. Logoutov, G. Cossarini, X. S. Liang and P. Moreno. 2009. Forecasting and reanalysis in the monterey bay/california current region for the autonomous ocean sampling

network-II experiment. Deep-Sea Res. Pt. II, *56*, 127-148.

Hamill, T. M. 2006. Ensemble-based atmospheric data assimilation, *in* Predictability of Weather and Climate, T. Palmer and R. Hagedorn, ed., Cambridge University Press, 124–156.

Hamill, T. M. and C. Snyder. 2000. A hybrid ensemble Kalman filter-3D variational analysis scheme. Mon. Weather Rev., *128*, 2905-2919.

Hickey, B. M. 1998. Coastal oceanography of western North America from the tip of Baja California to Vancouver Island, *in* The Sea, K. H. Brink and A. R. Robinson, ed., Wiley Inc., 345-393.

Hodur, R. 1997. The Naval Research Laboratory's coupled ocean/atmosphere mesoscale prediction system (COAMPS). Mon. Weather Rev., *125*, 1414-1430.

Huyer, A. and R. L. Smith. 1974. A subsurface ribbon of cool water over the continental shelf off Oregon. J. Phys. Oceanogr., *4*, 381-391.

Kalman, R. 1960. A new approach to linear filtering and prediction problems. J. Basic Enginee., *82*, 35-45.

Li, Z., Y. Chao, J. C. McWilliams and K. Ide. 2008. A three-dimensional variational data assimilation scheme for the regional ocean modeling system. J. Atmos. Oceanic. Tech., *25*, 2074-2090.

Lynn, R. J. and J. J. Simpson. 1987. The California Current System: The seasonal variability of its physical characteristics. J. Geophys. Res., *92*, 12947–12966.

Martin, P. J. 2000. Description of the Navy Coastal Ocean Model Version 1.0. Naval Research Laboratory, Stennis Space Center, 45 pp.

Mooers, C. and A. Robinson. 1984. Turbulent jets and eddies in the California Current

and inferred cross-shore transports. Science, *223*, 51.

Nelson, C. S. 1976. Wind Stress and Wind Stress Curl over the California Current, Naval Postgraduate School Monterey, CA, 89 pp.

Paduan, J. and M. Cook. 1997. Mapping surface currents in Monterey Bay with CODAR-type HF radar. Oceanography, *10*, 49–52.

Paduan, J. and H. Graber. 1997. Introduction to high-frequency radar: Reality and myth. Oceanography, *10*, 36–39.

Paduan, J. D. and L. K. Rosenfeld. 1996. Remotely sensed surface currents in monterey bay from shore-based HF radar (Coastal Ocean Dynamics Application Radar). J. Geophys. Res., *101*, 20669-20686.

Paduan, J. D. and I. Shulman. 2004. HF radar data assimilation in the Monterey Bay area. J. Geophys. Res., *109*, doi:10.1029/2003JC001949.

Pavlova, Y. V. 1966. Seasonal variations of the California Current. Oceanology, *6*, 806-814.

Pedlosky, J. 1974. Longshore currents, upwelling and bottom topography. J. Phys. Oceanogr., *4*, 214-226.

Pierce, S. D., R. L. Smith, P. M. Kosro, J. A. Barth and C. D. Wilson. 2000. Continuity of the poleward undercurrent along the eastern boundary of the mid-latitude north Pacific. Deep-Sea Res. Pt. II, *47*, 811-829.

Rainville, L. and R. Pinkel. 2006. Propagation of low-mode internal waves through the ocean. J. Phys. Oceanogr., *36*, 1220-1236.

Ramp, S., L. Rosenfeld, T. Tisch and M. Hicks. 1997. Moored observations of the current and temperature structure over the continental slope off central California 1. A basic

description of the variability. J. Geophys. Res., *102*, 22877-22902.

Ramp, S. R., J. D. Paduan, I. Shulman, J. Kindle, F. L. Bahr and F. Chavez. 2005. Observations of upwelling and relaxation events in the northern Monterey Bay during August 2000. J. Geophys. Res., *110*, doi:10.1029/2004JC002538.

Ramp, S. R., R. E. Davis, N. E. Leonard, I. Shulman, Y. Chao, A. R. Robinson, J. Marsden, P. F. J. Lermusiaux, D. M. Fratantoni, J. D. Paduan, F. P. Chavez, F. L. Bahr, S. Liang, W. Leslie and Z. Li. 2008. Preparing to predict: The Second Autonomous Ocean Sampling Network (AOSN-II) experiment in the Monterey Bay. Deep-Sea Res. Pt. II, *56*, 68-86.

Reid, J. L., R. A. Schwartzlose and D. M. Brown. 1963. Direct measurements of a small surface eddy off northern Baja California. J. Mar. Res., *21*, 205-218.

Rhodes, R. C., H. E. Hurlburt, A. J. Wallcraft, C. N. Barron, P. J. Martin, E. J. Metzger, J. F. Shriver, D. S. Ko, O. M. Smedstad, S. L. Cross and A. B. Kara. 2002. Navy real-time global modeling systems. Oceanography, *15*, 29-43.

Robinson, A. R., P. J. Haley Jr, P. F. J. Lermusiaux and W. G. Leslie. 2002. Predictive skill, predictive capability and predictability in ocean forecasting, *in* Proceedings of the The OCEANS 2002 MTS/IEEE Conference, Holland Publications, 787-794.

Rosenfeld, L. K., F. B. Schwing, N. Garfield and D. E. Tracy. 1994. Bifurcated flow from an upwelling center - a cold-water source for Monterey Bay. Cont. Shelf Res., *14*, 931-964.

Schwarz, G. 1978. Estimating the dimension of a model. The Annals of Statistics, *6*, 461-464.

Sherman, J., R. E. Davis, W. B. Owens and J. Valdes. 2001. The autonomous underwater

glider Spray. J. Ocean. Enginee., *26*, 437-446.

Shulman, I., C. R. Wu, J. K. Lewis, J. D. Paduan, L. K. Rosenfeld, J. C. Kindle, S. R. Ramp and C. A. Collins. 2002. High resolution modeling and data assimilation in the Monterey Bay area. Cont. Shelf Res., *22*, 1129-1151.

Shulman, I., J. Kindle, P. Martin, S. DeRada, J. Doyle, B. Penta, S. Anderson, F. Chavez, J. Paduan and S. Ramp. 2007. Modeling of upwelling/relaxation events with the Navy Coastal Ocean Model. J. Geophys. Res., *112*, doi:10.1029/2006JC003946.

Shulman, I., C. Rowley, S. Anderson, S. DeRada, J. Kindle, P. Martin, J. Doyle, J. Cummings, S. Ramp, F. Chavez, D. Fratantoni and R. Davis. 2009. Impact of glider data assimilation on the Monterey Bay model. Deep-Sea Res. Pt. II, *56*, 188-198.

Strub, P., P. Kosro, A. Huyer and C. Collaborators. 1991. The nature of the cold filaments in the California Current System. J. Geophys. Res., *96*, 14743.

Strub, P. T. and C. James. 1995. The Large-Scale Summer Circulation of the California Current. Geophys. Res. Lett., *22*, 207-210.

Sverdrup, H. U. and R. H. Fleming. 1941. The waters off the coast of southern California, March to July 1937. Bulletin of the Scripps Institution of Oceanography, *4*, 261-387.

Sverdrup, H. U., M. W. Johnson and R. H. Fleming 1942. The oceans: their physics, chemistry, and general biology. Prentice-Hall, New York, 1087 pp.

Tippett, M. K., J. L. Anderson, C. H. Bishop, T. M. Hamill and J. S. Whitaker. 2003. Ensemble Square Root Filters. Mon. Weather Rev., *131*, 1487-1490.

Tisch, T. D., S. R. Ramp and C. A. Collins. 1992. Observations of the geostrophic current and water mass characteristics off Point Sur, California, from May 1988 through November 1989. J. Geophys. Res., *97*, 12535-12555.

Toth, Z. and E. Kalnay. 1993. Ensemble Forecasting at NMC: The Generation of Perturbations. B. Am. Meteorol. Soc., *74*, 2317-2330.

Tracy, D. E. 1990. Source of cold water in Monterey Bay observed by AVHRR satellite imagery. Master Thesis thesis, Naval Postgraduate School, Monterey, California, 126 pp.

Tseng, Y. H., D. E. Dietrich and J. H. Ferziger. 2005. Regional circulation of the Monterey Bay region: Hydrostatic versus nonhydrostatic modeling. J. Geophys. Res., *110*, doi:10.1029/2003JC002153.

Wang, X., T. M. Hamill, J. S. Whitaker and C. H. Bishop. 2007. A comparison of hybrid ensemble transform Kalman filter-optimum interpolation and ensemble square root filter analysis schemes. Mon. Weather Rev., *135*, 1055-1076.

Wang, X., D. M. Barker, C. Snyder and T. M. Hamill. 2008. A hybrid ETKF-3DVAR data assimilation scheme for the WRF model. Part I: Observing system simulation experiment. Mon. Weather Rev., *136*, 5116-5131.

Wang, X. C., Y. Chao, C. M. Dong, J. Farrara, Z. J. Li, J. C. McWilliams, J. D. Paduan and L. K. Rosenfeld. 2009. Modeling tides in Monterey Bay, California. Deep-Sea Res. Pt. II, *56*, 219-231.

Weaver, A. T. and P. Courtier. 2001. Correlation modelling on the sphere using a generalized diffusion equation. Q. J. Roy. Meteorol. Soc., *127*, 1815-1846.

Weaver, A. T. and S. Ricci. 2004. Constructing a background-error correlation model using generalized diffusion operators, *in* Proceedings of the ECMWF Seminar Series, ECMWF, UK, 327-340.

Webb, D. C., P. J. Simonetti and C. P. Jones. 2002. SLOCUM: An underwater glider

propelled by environmental energy. J. Ocean. Enginee., *26*, 447-452.

Wickham, J. B. 1975. Observations of the California countercurrent. J. Mar. Res., *33*, 325-340.

Wooster, W. S. and J. H. Jones. 1970. California undercurrent off northern Baja California. J. Mar. Res., *28*, 235-250.

Yaremchuk, M., D. Nechaev and C. Pan. 2011. A hybrid background error covariance model for assimilating glider data into a coastal ocean model. Mon. Weather Rev., *139*, 1879-1890.

Yaremchuk, M., M. Carrier, H. Ngodock, S. Smith and I. Shulman. 2010. On the computational efficiency of the background error covariance models in the 3dVar assimilation. Ocean Model., accepted.